Delft University of Technology

Masters Thesis

Biotubes

Investigating the structure and mechanical behavior of biogenically cemented granular reefs

Thesis by Rutger Treur

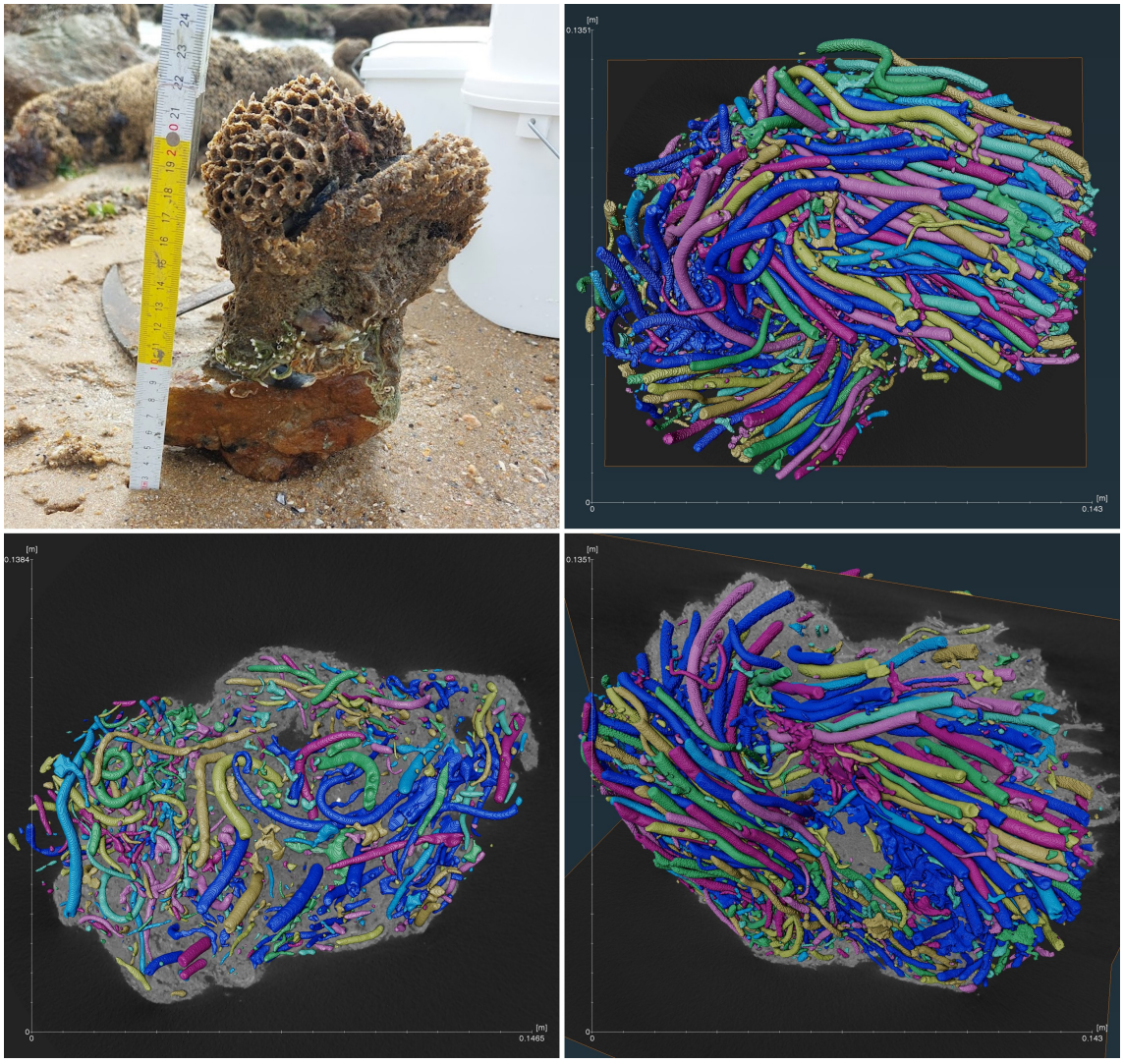

October 23, 2024

TU Delft

Thesis written to obtain the degree of Master of Science
at the Delft University of Technology,
to be defended publicly on Wednesday October 30, 2024 at 15:00.

Graduation committee:
Dr. Ir. D.J.M. Ngan-Tillard (chair/supervisor)
Dr. Ir. L. A. van Paassen
Ir. R. A. van der Eijk
Prof. dr. H. M. Jonkers

Abstract

S. Alveolata is a tube-dwelling polychaete which can be found all the way from the coast of Norway all the way down to Dakhla in the Western Sahara. It is able to build large reefs structures from sand filtered from the water column. It is known to have importance for biodiversity from animals feeding on the animal to its reefs providing a safe haven for fish. At the same time, a move is happening to using habitat protection and recreation for coastal protection. Several soft habitats such as mangroves, saltmarshes and seagrasses have been studied for their wave damping potential and S. Alveolata holds promise in this aspect. Given these functions, the S. Alveolata biogenic reefs need to be protected from outside influences, but little is known about their (mechanical) behaviour. As such, this study investigates the reef structure, erodibility, compressive and shear strengths of these reef materials and compares these to the commonly encountered loads from walking humans and wave loading. The static load from a person can reach up to 150 kPa while loading from 1.8 m waves can exert 36 kPa.

In agreement with Fournier-Sowinski (2013) and Vovelle (1965) but in contrast to Sanfilippo et al. (2019), the structure of the reefs to consist of three-layered tubes, with an organic sheath which partly contains a layer of flat grains placed next to each other on the inside and a scale-like layer of generally flat grains. These grains are glued together with proteinaceous glue spots showing a particular, bubbly structure. New is the description of bubbles radiating from the center of the glue spots. The grain size distribution shows a bi- or trimodal distribution, which has not been described before. S. Alveolata favours flat grains (in contrast to (Gruet & Bodeur, 1994; Lisco et al., 2020)) of about 1.0 mm size to build their reefs, which is a larger grain size than previously found (Gruet & Bodeur, 1994; Lisco et al., 2020; Naylor & Viles, 2000). As previously observed (Gruet, 1972), the reefs are made up of many tubes curving upward from a solid substrate. However, the first 3D mCT-scans of a whole reef block show enough voids so that small tubes wind their way through the reefs, probably made by juvenile worms. The grain size and mCT data suggest that tubes are reconstructed during the year.

The mechanical properties of these reefs show a very high compressibility with total strains between 10-20% under loads of 604 kPa. The reefs show a yield stress varying from 80-185 kPa. This is about the same stress as a person exerts while standing, the dynamic loads of walking are much higher but the limited time these loads are applied means little damage is done. Even though these yield stresses are far exceeded during testing, the samples hold some amount of cohesion due to interlocking and some unbroken bonds. Loose tubes weather from all sides at the same rate during slake durability tests. Shear box testing was conducted in a stepped manner with four loading steps from 48-380 kPa normal pressure, such that the first two steps are below yield stress at 48 and 96 kPa normal load. These show that the reefs have a cohesion of at least 23 kPa and a friction angle of 21.3°, explaining their resistance to waves. During testing, the reef samples compress strongly with their void ratios decreasing from 1.01 to 0.85. As a result of shearing, the internal tube structure of the sample was strongly deformed and shear bands or planes were formed during shearing. Some voids are also opened up in this process. After shearing samples show an apparent cohesion due deformed tube parts in which some bonds remain intact interlocking with each other. Compared to other cemented sands the S. Alveolata reefs exhibit many of the same features as these sands, such as the applicability of the Mohr-Coulomb criteria and high compressibility. However, unlike other cemented sands their open, tubular structure showed lower friction angles due to the alignment of sand particles in the linings. Also, the S. Alveolata lack the filling of void spaces often found on cemented sands leading to compressive behaviour.

Compared to the pressures to which the reefs are subjected in nature, the reef materials probably hold up well. The results provide a basis for more detailed investigation and testing and highlight key behavioural aspects of the material. It shows the response of the material to mechanical stresses and provides a starting point for using these reefs or solutions inspired upon them in different ways.

Acknowledgements

Writing this thesis has been a journey. Starting in early 2023 with the initial proposals and ideas coming from my supervisor, Dr. Ir. Ngan-Tillard and finishing in October 2024, over one and a half years later. In this time, I have gained valuable experience gathering funds, organizing and performing fieldwork, designing and performing tests and much more. These past months have earned me valuable academic experience and this would not have been possible without the many people helping out. First and foremost, I would like to thank my supervisor and chair of the graduation committee Dr. Ir. D.J.M. Ngan-Tillard for all her time and feedback, making this thesis into what it is. Secondly, my thanks go to Dr. Ir. L. A. van Paassen, Ir. R. A. van der Eijk for their time and ideas in developing this thesis and for their participation in the graduation committee. I would also like to thank Prof. dr. H.M. Jonkers for his participation in the graduation committee. My special thanks also go to the Molengraaff fund for providing the financial support necessary to carry out this research.

Apart from this, many people have aided in making the experiments and field work possible. As such, I would like to thank Dr. C. Chassagne and W. Ali for their help with the grain size experiments. The same goes for all the people from the different TU Delft labs for their help with the experiments: A. Thijssen and P.M. Meijvogel-de Koning for their help in the imaging of the S. Alveolata samples and C. Cavero Panez and K.N. Elliot, MSc for their help with the mechanical testing. Finally, I would like to thank Mr. Gourdon from the vessel 'Cormaris' for his help with sampling the H. Nirae during the field work.

Writing this thesis has been a massive challenge in many ways and as such I would like to thank those who have surrounded me with love and support all this time. To my friends and family, thank you for all your support during this long process, even when I was not sure I would ever finish. However, one person stands out. Marjolein, thank you for all you have done to support me over the last few years. This thesis would not have happened if it was not for the care you took of me during all this time. When starting this thesis, I did not think I would marry you before finishing. I cannot thank you enough for everything you have done.

Above everything and everyone, my thanks go out to the the triune God, the Most High, who has provided life, love and wisdom. To Him I dedicate this thesis.

Soli Deo Gloria

Rutger Treur
Delft, October 2024

Contents

List of Figures

List of Tables

Chapter 1

Introduction & State of the Art

As sea levels rise, coastal erosion increases. At the same time, a growing realization of the limitations of conventional structures is leading to an increased exploration of ecosystem engineering for coastal protection. In this light, some ecosystems may hold special promise, although they are little researched as engineering measures against erosion.

The tube-dwelling polychaete S. Alveolata is a worm that can build extensive reefs from sand particles, filtered from the water column. These reefs consists of tubes built against each other in specific structures, forming continuous but heterogeneous reefs that can cover large areas. At the same time these reefs can boost biodiversity and provide several other benefits.

Figure 1.0.1: Photo of S. Alveolata reefs covering rocks on the beachfront of Pornichet. In the foreground, pillow-shaped reefs are visible while encrusting reefs can be seen on rocks in the background. Photo taken at location 6.1C, for more information on the locations see appendix A.

1.1 Societal Relevance

In recent decades, many flood disasters have taken place on coasts all around the world. The most well known might be the flooding caused by hurricane Katrina in 2005 in New Orleans, but large scale flooding has also followed cyclone Nargis in southern Myanmar (2008), hurricane Sandy in New York (2012) and many more. Previously, conventional structures such as sea walls were used for these tasks. However, over recent times changes in climate conditions, sea-level, land subsidence and sediment supply have had significant effects on the sustainability of these kinds of

solutions. As such, it has been argued that ecosystem creation and restoration can provide a much more sustainable, cost-effective and ecologically sound alternative to these conventional structures (Temmerman et al., 2013).

At the same time, the emergence of nature-inspired materials focuses on solutions based on the natural environment. Examples of these solutions are by now found in all aspects of daily life, and take many forms: velcro tape inspired by cocklebur seed, robotic arms inspired by elephant trunks and kevlar inspired by fish scales. These examples and many more show the applicability of the nature-inspired approach in many levels of society and on all different scales (Katiyar et al., 2021). This nature-inspired approach translates very well into the aforementioned ecosystem engineering for coastal protection. And indeed many ecosystems such as mangroves, salt marshes, coral reefs, oyster reefs and sea grasses have been studied for their engineering potential (Perricone et al., 2023).

However, the study of biological systems goes back much further than this interest in nature-based engineering solutions. Although new species are still being described regularly, already in the eighteenth century large headways in this field were made. The famous botanist, geologist, doctor and zoologist Carl Linnaeus for example published several books in which he described and named multiple species of animals and plants. In one of those books we find a description of polychaete named Sabellaria Alveolata (Linnaeus, 1767). This name is comprised of two different components, the latin terms 'sabulum' meaning sand and 'alveolata', referring to the honeycomb structure that their reefs resemble. The common name used today for this species also refers to this: 'Honeycomb worm'.Van Duren et al. (2017) mentions this worm as a promising reef builder that might be an enrichment for the North Sea environment. It has also long been suggested that this species might hold promise in coastal protection, although it remains little studied in that perspective (Alves et al., 2017; Bruschetti, 2019; Lisco et al., 2017; Perricone et al., 2023).

1.2 Sabellaria Alveolata and its contructions

1.2.1 Species description and importance.

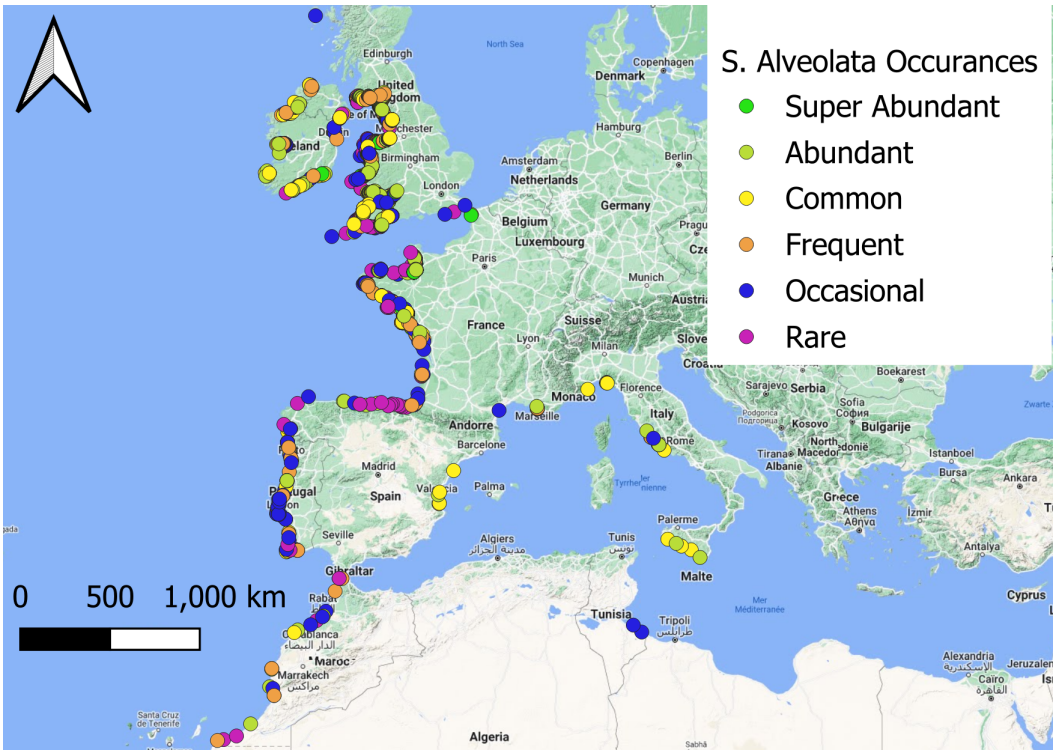

Figure 1.2.1: Map illustrating widespread occurance of S. Alveolata along the European and Africn coasts and their abundance. Data from Curd et al. (2020).

All members of the Sabellaria genus are able to build bioconstructions of different thickness, size and patchiness in intertidal and subtidal environments. Although depths are rarely quoted, Multer and Milliman (1967) mentions finding Phragmatopoma Lapidosa at depths up to 10 m. A photo

of a Sabellaria reefs can be found in figure 1.0.1. These bioconstructions are found worldwide, with them being described along the American pacific coast such as in Mexico and Chile as well as in India, Malaysia, New Zealand and in many places along the European coasts such as France, Sicily, the UK and mainland Italy (Dubois et al., 2002; Lisco et al., 2020). Along the European coasts S. Alveolata is the most widespread Sabellarid and the most important building organism in temperate coastal environments (Naylor & Viles, 2000). This is also illustrated by figure 1.2.1 which shows the different locations where S. Alveolata is found along with their abundance in those locations. They have been found far outside outside Europe and have been described from Norway (fig. 1.2.1) all the way down to Dakhla in the western Sahara (Lourenço et al., 2020) and possibly even northern Mauritania (Curd, 2020). Notably, one study found Sabellaria Spinulosa reefs on the Brown Bank area in the North Sea (van der Reijden et al., 2019).

These biogenic reefs as created by S. Alveolata have been studied over the last century or so. Recently, this has been because of its positive role in biodiversity. Like tropical coral reefs, these biogenic sand reefs open up numerous spatial and trophic niches for other species to colonize. Although the polychaetes dominate the fauna, other species also play important roles in reef functioning and the species richness of the reefs is much higher than that of the surrounding sediments. This extraordinary richness in species is explained by the variation in surface topography and the spatial heterogeneity associated with the reefs (Dubois et al., 2002). Besides this, the reefs buffer physical and chemical stresses, protect from predators and competitors and alter resource availability (Curd et al., 2019). This role in increasing biodiversity was found to be common over varying conditions in which the reefs develop (Muller et al., 2021). Because of this biological importance and its subsequent protected nature the reefs are regularly studied for their health (Curd et al., 2019).

Figure 1.2.2: Photo of an S. Alveolata worm showing its feeding organ in detail. Photo by Roux (2008).

It should be noted that the Sabellaria Alveolata itself is a filter-feeding sedentary polychaete. Individual worms are 2-5 cm long and build tubes of about 15 cm in length from sand-sized mineral grains. Individuals live for about four to five years with their main growth period during the first year. It has been found that the size of the tube correlates with the size of the organism and as such with the age of the worms themselves. As they grow older and larger, individuals build tubes with larger internal diameters. Also, the particle sizes used by the worms to build their tubes also increases with the ages because of a suggested link between particle size and the size of the building organ of the worms (Gruet, 1984; Naylor & Viles, 2000; Sanfilippo et al., 2019). The close-up photo in figure 1.2.2 gives an impression of how these worms look.

Although the reefs produced are widespread, they are not always continuous and vary in appearance during their lifecycle (Gruet, 1986). This is because the conditions under which they form are specific. They are adapted to and require relatively turbulent and sediment-laden water with a steady sediment supply from which they build their tubes (Naylor & Viles, 2000). Their development is also limited because they need rocky or sandy substrates on which to grow, although growth on other hard substrates such as concrete has also been observed (Gruet, 1986; Sanfilippo et al., 2019).

Because of their importance for biodiversity and the protected nature of their habitats research is being done in tracking and monitoring the reefs remotely. For this, special focus is currently on the use of remote sensing techniques. For example, Collin et al. (2018) explored combining very high-resolution optical imagery, photoquadrant groundtruth and neural networks to map S. Alveolata relative abundance. Additionally, Noernberg et al. (2010) exploited aerial photographs and LiDAR digital elevation models to quantify the volumes of Sabellaria present in the Bay of Mont-Saint-Michel.

1.2.2 S. Alveolata bioconstructions

When S. Alveolata does build its reefs, three different forms can be observed. Often they develop large pillow or hummock-like structures that can grow up to 1.8 m high. These are large colonies

of worms working together to create these large reefs. Although they often start as single large formations they can grow together to cover extensive reef areas (Gruet, 1986; Sanfilippo et al., 2019). However, a second reef type, which is an encrusting reef can also be formed. These reefs are generally about 30 cm high and spread over large ares. A good example of such a reef is found in figure 1.2.3. Thirdly, the worms can also occur alone, forming single tubes (Le Cam et al., 2011; Naylor & Viles, 2000). An encrusting reef can be seen in the background of figure 1.0.1 while small pillow structures can be seen in the foreground. Also, the reefs are known to prograde and retrograde as their habitats are subject to natural (e.g. cold winters and storms) and anthropogenic (e.g. trampling, harvesting, coastal disturbances) disturbances (Dubois et al., 2002; Firth et al., 2015; Plicanti et al., 2016). Where the prograding reefs are uniform and have the color of the surrounding sediments, the retrograding reefs are dark brown to grey in appearance with a highly fragmented surface. This offers certain advantages to marine life which have more room to hide while increasing the surface area dampens more wave energy. However, it has been noted that retrograding reefs are more susceptible to erosion by storm waves (Wilson, 1971). The reefs are able to go from retrograding to prograding through cyclic or erratic changes, and as such may have characteristics from both phases (Curd et al., 2019).

Although there are several forms in which S. Alveolata reefs occur, when looking at a slightly smaller scale all these different forms consist of large amounts of tubes which are attached to each other. However, some particularities do exist. These agglomerations of tubes have been studied for their grain size (Gruet, 1984), their structure and glue (Sanfilippo et al., 2019), their ability to be repaired (Gruet & Bodeur, 1994) and more. These agglomerations are built by many worms, although it is hard to count their concentration. Lisco et al. (2020) compared visual counting techniques to evaluations in thin sections finding significant differences in estimated tube density. At their peak, using thin sections, they found a tube density of 157,100 $\pm$ 42,000 tubes/m^2. However, these tube densities seem to vary seasonally with the spawn cycles of the worm. Others have found the number of tubes to vary from 18,875 $\pm$ 800 in February to 36,975 $\pm$ 900 in October using image analysis (Gravina et al., 2018). In periods with more young individuals the tube sizes are smaller and as such the densities are higher in these periods.

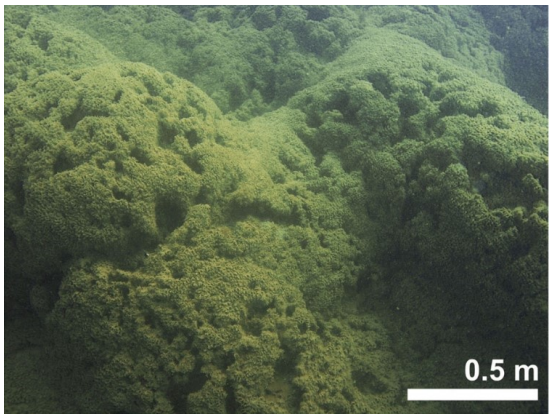

Figure 1.2.3: Underwater photograph of a S. Alveolata reef on the coast of Italy. Photo from Lisco et al. (2020)

Although these reefs have been studied in the past, some disagreements still exist surrounding their structure and granulometry. Observations by Naylor and Viles (2000) and Sanfilippo et al. (2019) indicate that the worms consolidate particles of a coarser size distribution than the mean particle size of surrounding sands. However, others have found preferential selection of the finer fraction when compared to the surrounding beach sand (Lisco et al., 2020). In this regard, many agree that particles are preferentially selected on size but correlated to the size of the worm (Gruet & Bodeur, 1994; Lisco et al., 2020; Naylor & Viles, 2000). This selection on size is further substantiated by the the fact that the grains that make up the tubes are better sorted than the intertube sands (Lisco et al., 2020; Lisco et al., 2021).

In addition to size, trials have shown that worms would select grains by shape, preferentially selecting ovoid grains while avoiding sharp grained shell fragments and thin plated micas (Gruet & Bodeur, 1994). Contrarily, others have found though that bioclasts such as mollusc shells are preferentially selected (Fournier-Sowinski, 2013; Naylor & Viles, 2000; Sanfilippo et al., 2019). Even to such a degree that the reefs have carbonate levels varying between 46.8-89.9% on reefs near Mont-Saint-Michel and 60-79.9% in the reefs around Champeaux (Fournier-Sowinski, 2013). The chemical nature of the clasts has also been shown to not be decisive (Gruet & Bodeur, 1994; Lisco et al., 2020). However, in spite of any preference that might be present, they can also deal with other materials such as glass beads (Buffet et al., 2017). However, S. Alveolata shows some latency when dealing with unusual materials (Vovelle, 1965).

Construction speeds are also variable, with Gruet and Bodeur (1994) finding speeds between 7.5-25 mm in two weeks. However, others have found speeds of up to 85 mm in 17 days with even higher

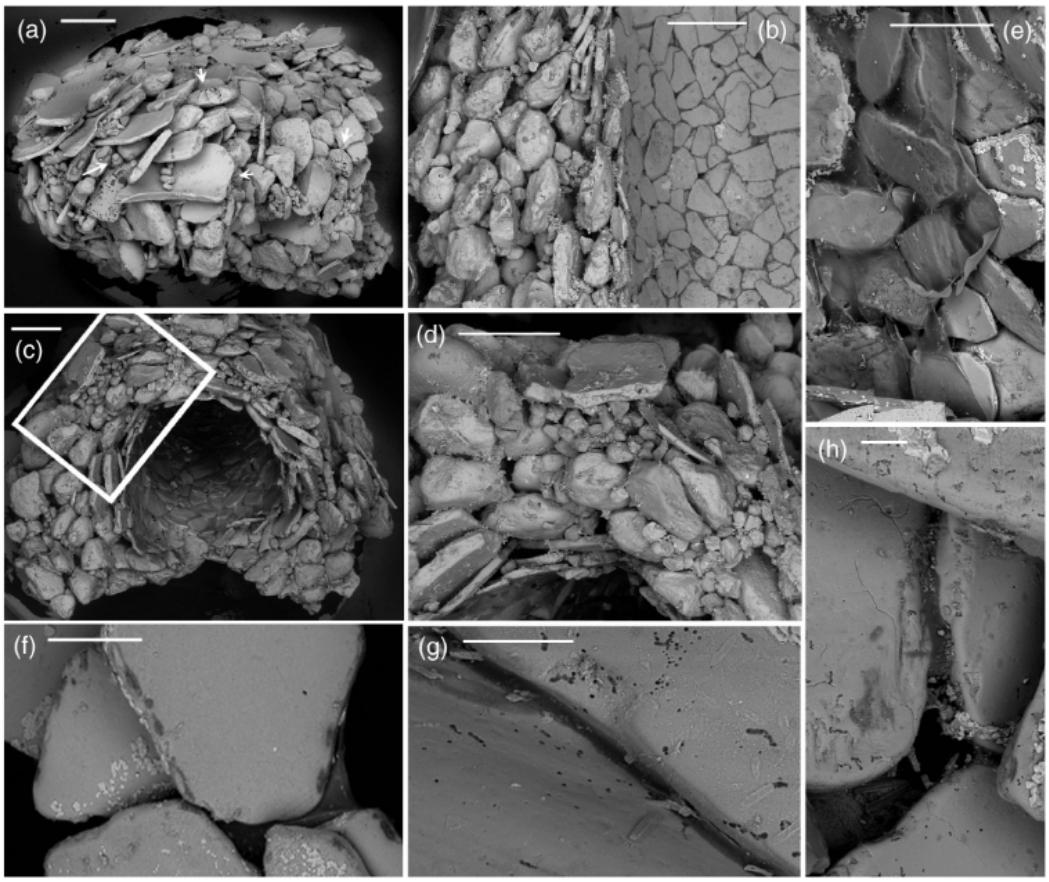

Figure 1.2.4: (a) External surface of a tube with grains of different composition, size and shape. Note prevailing flat fragments imbricate, inclined and divergent towards the aperture (right). The foraminifers Elphidium (short arrows) and Globigerina (long arrow) are present. (b) Longitudinal section of the tube figured in (a) and internal surface regularly paved by fragments of similar sizes and shape. (c) Architecture of the agglutinate tube showing layers with different clast morphologies, sizes and arrangements. (d) Detail of (c) showing an internal layer of flat particles, a mid layer with poorly selected, isodiametric elements, and an outer layer including large flat elements. (e) Organic thin sheet lining the inner surface of the tube. (f) Inner layer showing gluing modality. (g) Detail of glue at junction between two adjacent particles. (h) Grains glued along their edges. Scale bars 1 mm (a–d), 500 µm (e, f), 100 µm (g, h). Figure from Sanfilippo et al. (2019).

speeds at the start, building 10 mm per day for the first two days of construction. However, these speeds are were found in laboratory conditions and are probably slower under natural conditions (Vovelle, 1965). Under natural conditions, growth rates are highly variable: reefs can grow tens of cm's in three months (Lisco et al., 2021) depending on year and conditions. Rates of 10 cm in the first year recorded and about 6 cm in later years have been observed on one particular site by Wilson (1971). At the same time Gravina et al. (2018) found a yearly variation in thickness, with the reefs growing about 40 cm between April and October 2012, but then reclining to 10 cm over the winter. The temperature is a major factor in determining construction speed with higher temperature leading to higher construction speeds (Gruet & Bodeur, 1994). Speeds are also dependent on the length of the tentacles (figure 1.2.2) of the animal (Vovelle, 1965). For reconstruction, the existence of annular support from older tubes remains is necessary even though the larvae are able to fix themselves along the substrate to provide a starting point in that way (Vovelle, 1965).

Apart from their composition, the structure of the individual tubes is also worth noting. It has been found that their structure consists of several layers, starting with an inner organic membrane covered by three layers of sand. These consist of a thin inner layer of flat grains arranged side by side, a thick mid layer with a frame of relatively large sub-rounded grains and a thin outer layer of large, flat to curved, usually biogenic clasts which diverge towards the opening of the tube. The worms cement the grains together with a solid foam-like material which is made from proteins and is applied only in positions where the grains actually touch (Sanfilippo et al., 2019). This material

Figure 1.2.5: Photo of S. Alveolata showing the arched tooth shaped ends on S. Alveolata on the top, while bottom tubes are sufficiently protected and do not have these same tooth shaped ends. Photo taken at location 5.2, for more information on the locations see appendix A.

is formed by a process known as quinone tanning (Becker et al., 2012; Buffet et al., 2018; Vovelle, 1965), a process by which many different biomaterials are formed. These range from adhesives to extremely hard tissues (Hong et al., 2014; Kaneko et al., 2011). The structure of these cement-like materials is well illustrated by figure 1.2.4. In recent years, such adhesives have gained interest for their potential use in medical applications due to their superglue-like strength (Shao et al., 2009). Also, it has been noted in early research (Vovelle, 1965) that the tubes are built by the attachment of particles from the outside to the inside of the tube, with tubes only growing on their upper edge. The animals sort the particles they capture at their mouth before either releasing or incorporating them in their tubes.

Also, in turbulent waters S. Alveolata is known for building a tooth-shaped arch on top of their tubes which protects their tubes from turbulence. It opposes the dominant currents and slows down particles to make their capture easier. In calmer hydrodynamic environments the tubes open up like a horn (Fournier-Sowinski, 2013). This is shown well in figure 1.2.5, where the more exposed tubes on top have these toothed ends. However, the tubes on the bottom are protected by the overhang in the reef and therefore have no need for these tooth-shaped ends.

Despite the attention given to these reefs in many different types of research and the widespread notion of their importance in coastal protection (Le Cam et al., 2011; Naylor & Viles, 2000) as well as in sediment storage and beach nourishment (Lisco et al., 2020), little has been quantified about their behaviour as a geomaterial and their erosional resistance. Observations have been made though of the reefs ability to withstand severe storms and survive (Naylor & Viles, 2000). Le Cam et al. (2011) did study the mechanical properties of a single tube by loading small tube pieces in the radial direction, showing its visco-elastic behaviour which is related to the chemical composition of the cement. Also, Vorberg (2000) did some testing on samples of S. Alveolata reefs, finding uniaxial compressive strengths of 110-340 kPa. As such, many interesting questions remain regarding the mass behaviour of the material, its erosional resistance and other aspects of its mechanical behaviour such as its resistance to crushing by trampling.

Given this, the main research question of this thesis will be as follows:

> How do the S. Alveolata bioconstructions behave in response to different (environmental) loads?

In order to answer this question, the following subquestions need to be considered:

1. How are these bioconstructions structured and built?
2. What are their basic mechanical properties?
3. How do these materials respond to environmental pressures (such as wave impacts and human trampling)?

Chapter 2

Methodology

In order to answer the questions as set out at the end of the previous section, a testing methodology has been devised consisting of field work, imaging methods and mechanical testing of the reef sections.

2.1 Field work

Firstly, a fieldwork was performed in May 2023 during a period of high tidal coefficients in the area around Pornichet, including the bays of Vilaine, Pouliguen and Bourgneuf. During this fieldwork samples were taken of several bioconstructions around the area. This was mainly focused on sampling S. Alveolata biogenic reefs, but some other samples were taken as well. The visited locations during the field work are displayed in figure 2.1.1. Samples of the S. Alveolata reefs were taken using a jointing knife and a hammer where necessary. The few H. Nirae samples collected were taken using a Van Veen sampler to collect sediment samples from the sea floor. All samples were stored in bags which were in turn stored in containers with airtight lids in order to keep the samples close to in-situ moisture content. After the field work, samples were returned to the TU Delft where they were stored in a cooler room until they were used for experimentation. Further details such as the GPS coordinates of the field work locations and tidal coefficients for these days can be found in appendix A.

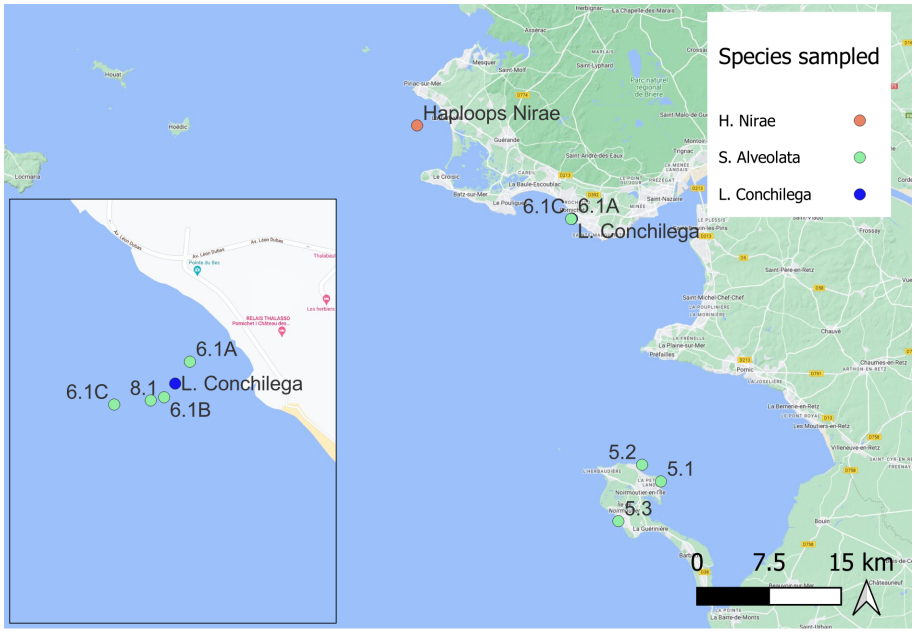

Figure 2.1.1: Map illustrating the fieldwork locations and the sampled bioconstructions at those locations. Labels refer to location numbers and dates. The GPS coordinates for each point can be found in table A.1.1.

2.2 Structural investigations

In order to answer the first subquestion on the structure and construction of these bioreefs, research on the structure of these geomaterials was done using imaging methods such as X-Ray micro-Computed Tomography (mCT-)scanning and microscopy. The set of imaging techniques will produce a full set of images as well as 3D renderings that can be used for studying the samples. In addition to this, some material is broken down and used for grain size analysis and Powder X-Ray Diffraction (P-XRD).

2.2.1 Imaging of S. Alveolata bioconstructions

In order to investigate the structure of the material studied here, several different methods were used. Mainly, digital microscopy and associated software, Environmental Scanning Electron Microscope (E-SEM) and mCT were used. Samples from different locations were cut down to small sizes and then analyzed. For optical microscopy, the blocks of samples were cut down to single tubes and small clusters, that were in turn dissected to smaller pieces both perpendicular and parallel to the tube axis. These were then investigated using the digital microscope. In total, 35 single tubes and 8 clusters were examined using magnifications from 10-2000 times with samples coming from different locations. More details on the amount of samples, the number of pictures taken and step-by-step procedures and precise equipment lists can be found in appendix C.1.

Secondly, for E-SEM investigations, samples were prepared in a similar way as for digital microscopy. However, they were cut down to smaller sizes as to fit on the metal studs used for loading samples in the E-SEM vacuum chamber. Here, samples were also cut to view the different parts of the tube and as such samples were cut both parallel and perpendicular to the tube axis. After E-SEM scanning, the samples were re-examined in the optical microscope. In total, 13 different tubes from different locations were cut down for examination using the E-SEM. The exact details of the equipment used and the amount of photos taken are found in appendix C.2.

Lastly, a block from location 6.1C was in its entirety detached from its rock base during the fieldwork. This block was scanned using mCT to reveal its structure. Afterwards, the area where it was attached to the substrate was detached from the block using a jointing knife and scanned again to obtain this part in a higher resolution. Also, another small sample was produced to scan at high resolution both for structural investigations as well as to try and measure the porosity of the material. Details of the scans such as exposure times and voxel sizes can be found in appendix C.3. The CT datasets were consequently analyzed using Avizo software in order to visualize the porosity. This included using sets of filters and label analysis steps that allow a visualization of the complete porosity as well as a visualization of the tubes. The step-by-step procedures for image analysis are given in appendix D.

2.2.2 Grain analysis

Several single tubes, collected from location 5.1, were cut in three pieces and disintegrated by destroying the organic material between the grains. The disintegration was done using hydrogen peroxide on a hot plate following the step-by-step method outlined in appendix B. These grains were then collected and analyzed using a laser diffractometer for their size composition. From this, the evolution of grain sizes along the length of the tube could be investigated. The loose grains were then analyzed in a laser diffractometer from which particle size distributions were produced. More details on the equipment used for analysis equipment can be found in appendix C.4. In total, every sample was composed of 50 runs of measurements. For every run, a size distribution was generated as well as a d10, d50 and a d90. d10, d50 and a d90 are the grain sizes at which 10%, 50% and 90% of grains respectively are smaller than that size, measured at the diameter. From these measurements, the mean was taken to get the statistics for the grain distributions. Only runs on which d90 > 500 μm were taken into the statistics due to the coarse nature of the material. The size distributions were plotted with the average of the different runs and their standard deviation.

Additionally, two tubes from different locations (5.1, 6.1B) were disintegrated and the resulting loose grains were crushed. At the same time, sand from the nearby beaches was also crushed and investigated using P-XRD (Powder X-Ray Diffraction) in order to compare their mineral compositions.

2.2.3 Glue spot analysis

The goal from these experiments was to quantify both the size and distribution of the glue spots found in the reefs. Tweazers were used to mechanically separate grains from a small tube section. Tube sections in this experiment were taken from location 6.1B and 5.3. These single grains were then left to air dry for a few days after which photos were taken of the grains using the keyence microscope described in section C.1 at a set magnification of 100x. These were then analyzed using the accompanying Keyence software. Using a point measurement tool, the length of the linearly shaped glue spots was measured. For the circular glue spots, a diameter measurement tool was used. These measurements were then processed using python. Since grains were not turned over during the analysis, the amount of glue spots was estimated by doubling the number of spots on the side of a grain and adding the number of spots visible on the edges (which would also be visible from the other side of the grain). More specific information on the amount of measurements done, the number of grains analyzed and more can be found in appendix C.6.

2.3 Mechanical testing

In order to investigate the mechanical properties of these reefs, several tests were performed on reef blocks. Two different slake durability tests were performed in order to investigate the durability of the material under abrasive/erosional conditions. Secondly, a set of oedometer experiments was done to investigate the resisting to crushing under lateral constraints. This is similar to the application of loads to the tops of the reefs such as walking pressures or even construction. Thirdly, multi-stage shear box tests were performed to investigate the shear resistance of the material. This shear resistance helps characterize the response of the material under different loading conditions in order to more fully capture the material behaviour.

2.3.1 Slake durability testing

The slake durability apparatus consists of drum, a motor drive and a basin which can be filled with fluid. The drum walls are mesh with a solid base and a solid lid. The trough is constructed in such a way that the test drum can be suspended in it. It is placed such that the motor drive can be connected to it. The motor is capable of rotating the drum at a constant speed of 20 rpm $\pm$ 5% for 10 minutes. A schematic of this test can be found in figure 2.3.1a accompanied by a photo of the setup in the lab in figure 2.3.1b.

Firstly, a set of 3 durability tests was performed according to the protocol as published by the ISRM (Ulusay & Hudson, 2007). In this protocol, ten reef blocks are cut into smaller blocks weighing 40-60 g, to give a total sample mass of 450-550 grams. They are then put in a clean drum and oven-dried at 105 °C for about 2 hours. The mass of the sample and drum is then recorded. After this, the lid is put on, the drum mounted in the apparatus and coupled to the motor. The bath is filled with water at room temperature to a level 20 mm below the drum axis. The drum is then rotated for 200 revolutions in 10 minutes with an accuracy of 0.5 minutes. After this the drum is removed from the apparatus, the lid taken off and the drum is oven dried for about 2 hours at 105 °C. After this the mass is recorded, the drum placed back in the machine and turned for another 10 minutes/200 revolutions and dried again. The percentages of retained weight after each cycle are recorded as slaking indices. A step-by-step procedure can be found in appendix E.1. For this test, two batches of blocks were used from location 4.1 and one batch on blocks was used from location 5.2.

As a second test, several reef blocks collected from location 8.1 were dissected into single tube sections. These sections were then sorted and categorized by length so that three similar sample batches are produced, each consisting of 54 tube sections of different lengths. The exact number of tubes per batch and the lengths of the classes is found in table 4.1.2. These were then dried, their weight recorded, put in a drum and tumbled for 5 minutes/100 revolutions. After this, the drums were emptied, the tubes sorted and dried and the tubes were weighed per batch. As such, the change in weight and tube amounts is recorded. The procedure is outlined more detailed in appendix E.1.

2.3.2 Oedometer Testing

Three different samples of diameter 50 mm were cut from larger reef by pushing the testing ring into blocks collected from location 5.3. With tubes generally having a diameter of a few millimeters,

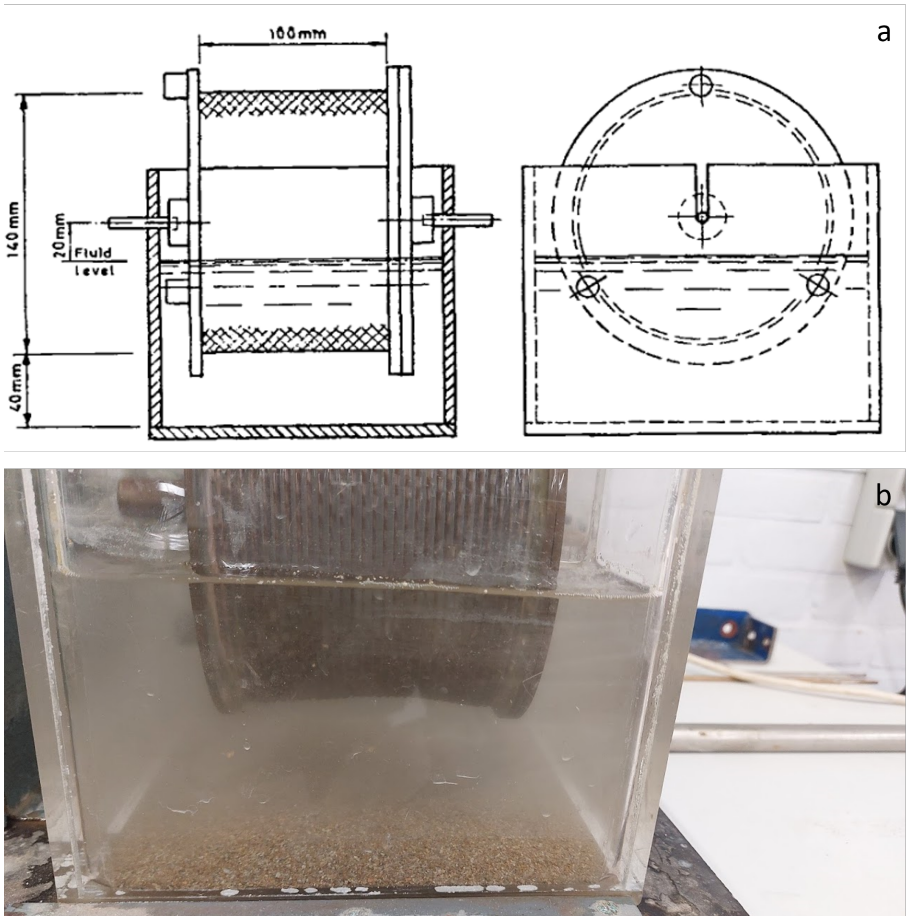

Figure 2.3.1: a) Schematic drawing of the slake durability setup as used for the experiments. Figure from Ulusay and Hudson (2007). b) Photo of the setup during experimentation in the lab at TU Delft.

this ensures that enough tubes are present for representative experiments. These were then tested fully saturated in an oedometer, the cap was placed and the samples were tested at stresses from 4 to 304 kPa in 6 50 kPa steps. Then, 3 100 kPa steps were done, so that the maximum vertical stress was 604 kPa. After this, pressure was relieved in 3 steps, with each step releasing 200 kPa from the sample. These pressures were chosen as a man in rubber boots exerts about 150 kPa static pressure (Vorberg, 2000) onto the surface. Similar numbers were found during experiments by Cavanagh et al. (1987) and Grieve and Rashdi (1984) who found standing pressures to having a maximum of about 140 kPa, although they were dependent on what area of the foot was investigated. Peak pressures were found under the heel with much lower pressures of about 55 kPa being found under the forefoot. Also, a young adult of about 80 kg will exert a maximum of about 350 kPa dynamic pressure without shoes (Hessert et al., 2005; Rodgers, 1995). This does not however include the damping effect of footwear, which is hard to quantify as it depends on many factors. It is also worth remembering that these pressures only last for a short time, with peak loading rates lasting only 25 msec (Rodgers, 1995). However, a large variety exists with pressures for walking adults also being put at 210 kPa (Grieve & Rashdi, 1984). With the pressures chosen, this range is well covered, with extra steps added after this point to ensure failure occurs. After each loading step at least 15 minutes were allowed for settlement of the sample. Also, a sand sample collected from the beach of Le Croisic was tested as reference material. A more complete overview of the sample preparation and testing procedure is present in appendix E.2. Samples were tested with the load as parallel to the tube direction as possible. This is representative of many portions of the encrusting reef type, where tubes stand up straight from the top of rocks. This is where they have the largest risk of being stepped on. The test parameters such as sample weights and sizes are given in table E.2.1.

2.3.3 Shear box testing

For shear box testing, three different round samples were cut from samples taken at location 6.1C. In this case, samples were used that from sampling tubes with a diameter slightly larger diameter than that of the shear box (63 mm). As such, as a preparation for the experiment a layer of a few mm's thickness was removed from the outside of the tubes after which they were placed inside the shear box. The reef blocks were tested at several different normal stress levels incrementally. In these tests, first a normal load of 48 kPa was applied and then the sample was sheared until constant shear stress (i.e. stress did not increase anymore with displacement). Then they were loaded to 96 kPa and sheared until constant stress. This was repeated with steps at 190 and 380 kPa. Samples were then taken out of the shear box, weighed, dried and weighed again. Samples were sheared with a speed of 1 mm/min at their natural moisture level, without wetting or drying beforehand.

These normal stresses were selected to cover a large range of stresses, while trying to keep the first two steps below the yield stresses determined by oedometer testing. Stepped shearing was done because the amount of material available in the size range required for these tests was limited. This way, more data could be gathered while using less material. As the material showed strong variability during earlier testing, three replicate tests were performed to give some indication of the variability under shear conditions.

The same was done with three different samples reconstructed from beach sand collected from the Le Croisic beach. This is an uncemented beach sand rich in angular carbonate bioclasts. These were all prepared at different void ratios. One sample was prepared at a large void ratio by carefully placing sand layer by layer into the mold using a funnel. One sample was prepared at intermediate void ratio by using the same method as the large void ratio sample, but compacting the sample afterwards by tamping and shaking the sample. One sample was prepared at small void ratio by placing the sands layer-by-layer but compacting in between layers by shaking and tamping the sample. See appendix E.3 for more details. These were then tested in the same manner as described in the section before. After this, the test data is analyzed and described. A more complete explanation on the working of the shear box as well as more in depth testing and sample preparation procedures are described in appendix E.3. Sample dimensions are also given there as well as some additional results.

2.4 Summary

This section outlined the testing protocol used for this thesis. Firstly, imaging techniques will be employed to observe the reefs. E-SEM will be used for the smallest scales, microscopy for the intermediate scale and mCT for the larger scale. Also, grain size measurements are done to collect data on the grains in the reefs, together with an analysis on the number and size of glue spots. P-XRD will be used to highlight the mineral composition of the reefs, also compared to the surrounding sands.

Secondly, mechanical testing will be done. Slake durability will be done to simulate the effect of weathering/abrasion of the reef blocks and the single tubes. 1D compression testing is done to investigate the tubes under compression along their tube axis, simulating loads such as walking or construction. Shear box testing will be employed to gain more insight into the behaviour of the material under varying stress conditions. In the 1D compression testing and the shear box testing, a beach sand will be tested along the reefs to provide a comparison material.

Chapter 3

Structural aspects & Characterization

This chapter will outline the observations made regarding the structure of the S. Alveolata bio-constructions. It will be discussed from small to large scale. As such, the small-scale organic materials will be discussed first. Secondly, the structure of the tube will be discussed. Thirdly, we will explore the way the different tubes work together to build reefs. After this, the particle sizes and the mineral composition of the reefs will be looked at. Lastly, the investigation done on single grains and glue spots measurements will be discussed. All these sections will follow a set structure: first showing any observations, then these will be interpreted and analyzed and lastly the validity and suitability of the method is debated.

3.1 Organic materials

Results

As shown in figure 3.1.1, the glue of S. Alveolata has a particular structure. It is bubbly, with bubbles often bigger near the center of the glue spots. At the same time, glue thickness decreases near the contact points of the grains as shown most clearly by figure 3.1.1a. However, some other notable features are present as well. As shown in figure 3.1.1b especially, the glue is seamlessly connected to the grain surfaces to such a degree that the boundary between the glue and the grains is often difficult to distinguish. Additionally, it should be noted that the bubbly texture of the glue is not present at the glue edges where a surface-hardening effect can be observed. At these edges a solid layer forms as displayed in figure 3.1.1d. At the edges of these spots, lots of small crystalline material as well as small biogenic debris can often be found (figure3.1.1a/d). The glue spots also generally come into two different shapes: they are often either hollow disks or elongated patches as illustrated in figures 3.1.1b/c.

However, other non-mineral structures are also present. Cables of organic materials are often visible, connecting grains. (fig. 3.1.2a) Also, an inner organic sheath is present on the inside of the tubes. This is placed along a layer of flat grains which is the inner lining of the tube (figure 3.1.2b). Between grains, structures that resemble pillars are present with their outside surfaces filled with fine-grained mineral grains (fig. 3.1.2c). One of the cables seems to originate at a glue spot as shown in figure 3.1.2d.

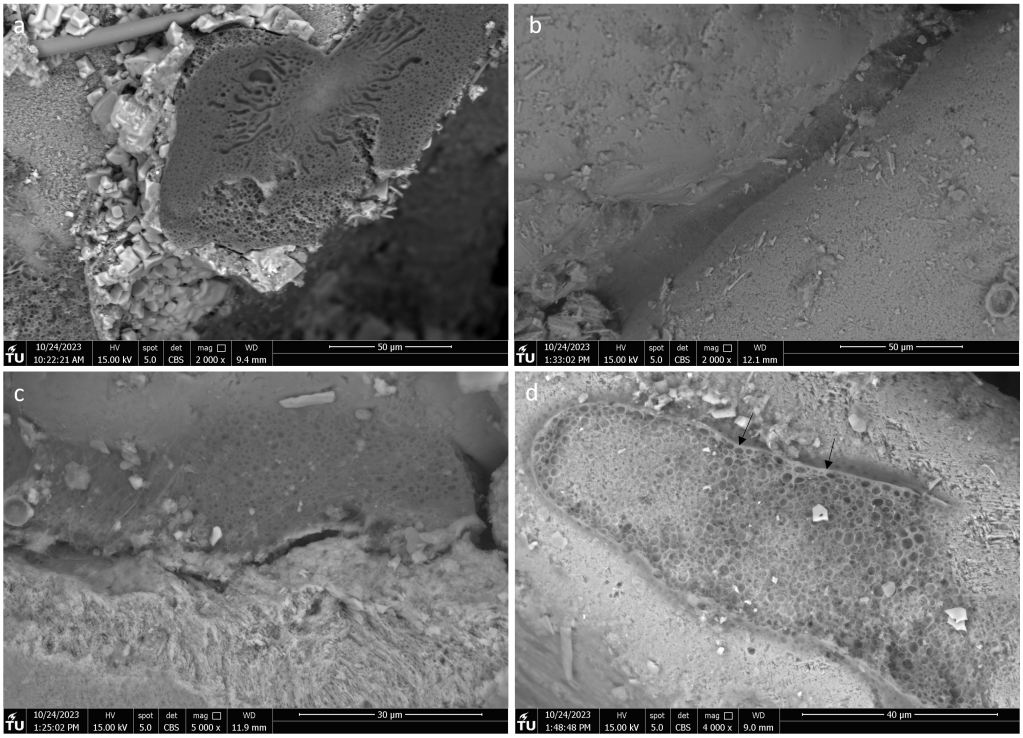

Figure 3.1.1: Details of glue spots from different samples and locations. a) The bubbly glue texture is clearly visible with bubble size increasing to the center. Glue thickness decreases towards the grain contact. Note also that glue has not just bubbles, but also much more elongated and longer voids radiating out from the center. b) Glue is seamlessly connected to the mineral grains. c) Contact between glue and grain is very smoothly shaped making the exact contact difficult to distinguish. d) The outer layer of the glue forms massive layers in which no bubbles are observed at the current magnifications.

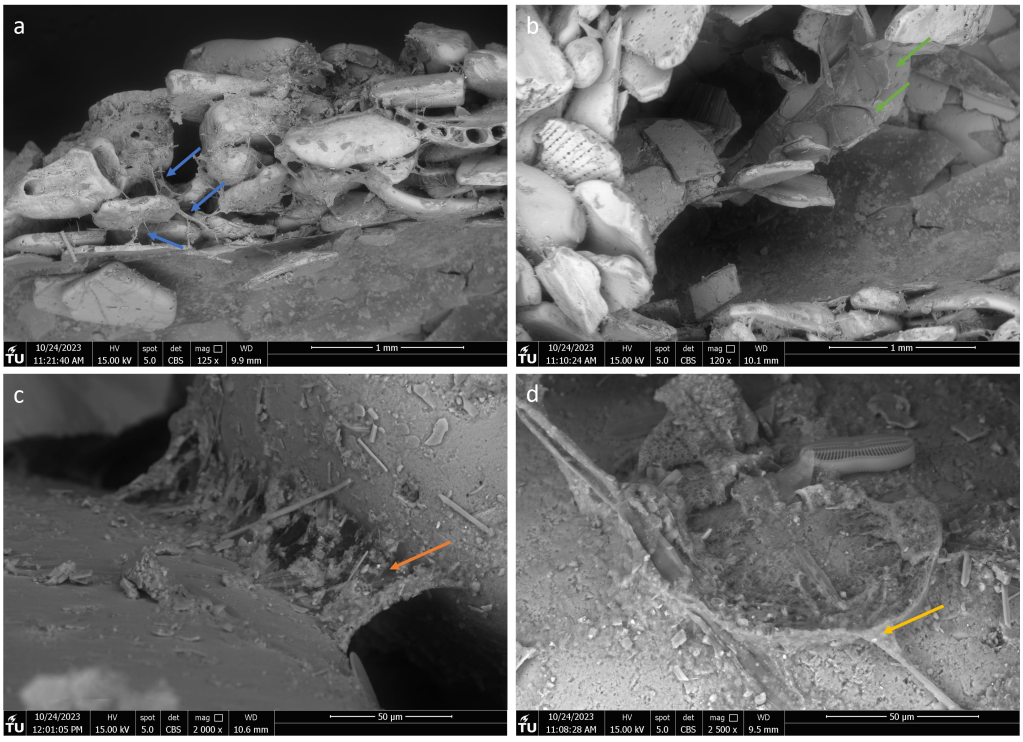

Figure 3.1.2: Other organic materials and structures visible in the S. Alveolata reefs. a) Many cables connect different grains all through the sample (blue arrows). b) An organic sheath is present inside the tube, and the inner lining of grains is embedded in it (green arrows). The sheath is partially detached in this image. c) Pillars, often covered in small crystalline debris, connect different grains on the small scale (orange arrows). d) Organic cables originate at glue spots (yellow arrows).

Samples that were imaged using SEM were also studied using light microscopy. As such, similarities can be observed. Looking at figure 3.1.3, the bubbly glue spots in the SEM appears as brown dots under the digital microscope.

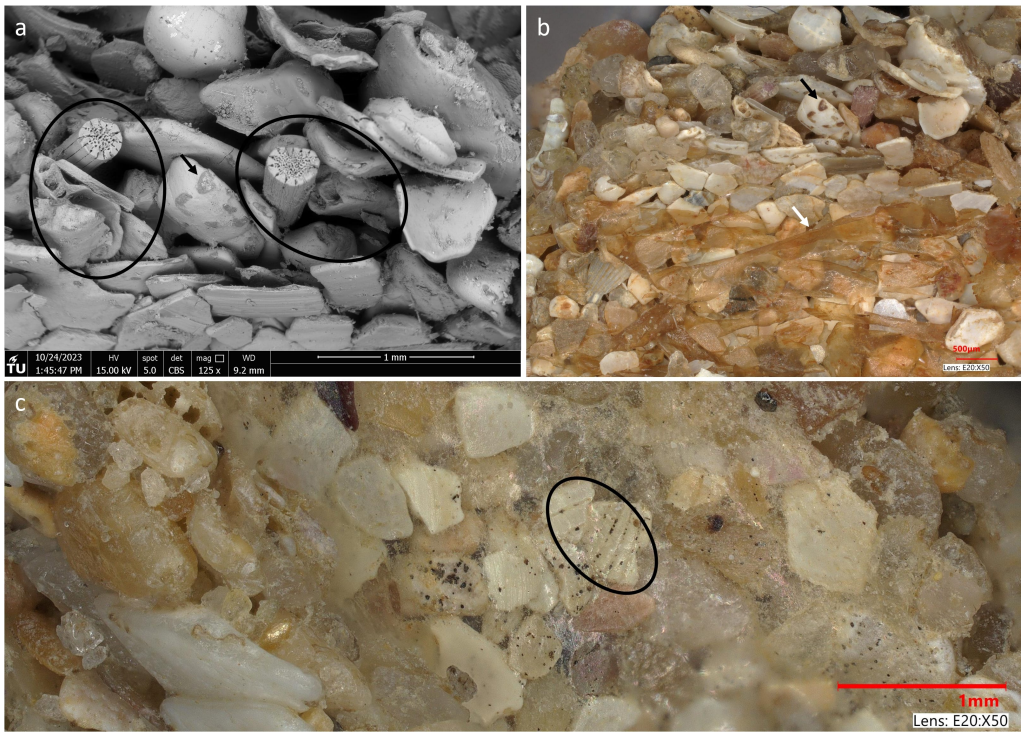

Figure 3.1.3: E-SEM (a) and digital microscopy (b) images of the same sample area, taken after SEM work. Particularly noteworthy are the glue spots clearly visible in both images, as indicated by the black arrows. Additionally the browned and curled material as indicated by the white arrow is the degraded organic sheath. When comparing these to (c), which is a much fresher sample, the effect of the vacuum in the SEM becomes clear. Both gluing spots and inner sheath show darkening and discoloration after SEM. Also note the large amount of biogenic grains present in the tubes as indicated by the black circles.

All samples examined using E-SEM were also investigated using digital microscopy afterward. As such, a comparison can be made. In relatively fresh samples (as displayed in figure 3.1.3c), glue spots and the organic sheath can be distinguished. The sheath is generally colorless, giving off a shimmer which makes it visible. Glue spots are also visible, often having a slightly brown hue. However, after SEM imaging (figure 3.1.3b) the sheath has suffered significant color change to a darker brown. It has also detached from the grains and torn, sometimes also taking grains with it as in figure 3.1.2b. The glue spots also show a similar discoloration, showing a darker brown color after SEM imaging. Similar color changes and detachments were also observed in samples that were stored in the open air for longer times.

Interpretation & Discussion

The glue spot shapes are a result of the different ways that grains can be connected. As will be shown later, most grains in the reefs are flat or elongated grains. As such, the grains can be connected on the concave surface or along their edges. The hollow disk shaped glue spots fit well grains connected along the concave surface while the elongated patches are used for connecting the different edges. This differences in glue spot shapes was also found in earlier research (Sanfilippo et al., 2019). The pattern of radiating bubbles found here was not described earlier. This may indicate that this result is not as common overall as was found in this study. When looking at the images presented by Sanfilippo et al. (2019), glue spots also show the same thickness patterns with thickening to the outside of the glue spots. At the same time, the existence of the inner organic sheath was noted by other researchers (Sanfilippo et al., 2019; Vovelle, 1965).

Also, one observation was made of an organic cable originating at a glue spot. However, upon further investigation, no more instances of this phenomenon could be observed. This did suggest a

similarity of the different organic materials observed here such as the glue, sheath and the observed pillars. Unfortunately, assessing the internal structures of these material was not possible. However, if the sheath and pillars were of similar material as the glue, some similarities would be expected.

The similar way in which both the sheath and glue spots age indicates a similarity between the materials. Although no bubble-like structure is observed in the organic sheath, this could be explained by the face-hardening effect of the glue as shown in figure 3.1.1. However, the application process of the organic sheath was previously concluded to be different to that of the glue spots with different glands being used. The worm produced the organic sheath with a rubbing motion inside the tube, the particles were glued directly in a specific place, with construction only found to take place on top of the tube (Vovelle, 1965). Also, Gruet et al. (1987) showed the two materials to have a different composition, with the inner sheath being richer in sulfur. However, given that Buffet et al. (2018) was not able to clearly distinguish two materials when researching the glands, it is likely that they are similar in nature and composition but not the same. At a much smaller scale, the sheath was found to be made up of a large number of sub-μm elementary films (Vovelle, 1965). This structure was not found in this study, probably due to limitations in the methods. At the high magnifications necessary for this, the SEM beam often damaged the samples, making investigation impossible. This is because samples in this study were not coated with any conductive materials, which would prevent buildup of electrons in the sample. This technique was employed by Vovelle (1965).

Questions also remain on how the glue spots are formed. There are several possibilities for this, the particles might be coated with glue and then pressed onto other grains with the glue accumulating at the contacts due to capillary forces. On the other hand it is also possible that the glue is applied to the grain contacts directly, with the glue then being squeezed outwards when the grains are pushed together. In both cases, the size of the spots is dependent on the amount of glue excreted by the individual animal. Previous research indicated only that the glue is applied before the grains are placed, making the first mechanism more likely (Vovelle, 1965). This also fits the observations made of glue spots seamlessly connecting to the grains and converging in the middle, making this the more likely scenario. However, the observation of radiating bubbles would generally more confirm to the second scenario, but these may also be formed as part of the drying process and as such not be a result of the application mechanism.

Suitability of Method

Generally speaking, digital microscopy did well at highlighting small features in these reefs. However, identification of the smallest features proved difficult. Although the Keyence digital microscope employed in this study was able to go to the required magnifications (2500x) to show the glue spots, it was not successful in showing any of the features in the glue spots as identified by the E-SEM. This because of the reflective properties of the materials studied, both grains and the inner organic sheath reflected too much light to make identification possible even at the lowest light setting. In the future using UV-light and a band-pass filter to investigate biocement using its the bioluminescent properties (Sanfilippo et al., 2019) may make using digital microscopy possible.

At the same time E-SEM was successful at showing the small-scale features of the reefs. However, issues were encountered at the highest magnifications which hindered imaging. Often, the non-conductive samples were charged by the electron beam leading to damage in the samples in the form of small holes or small breakages. This lead to some difficulties imaging at high magnification. If even smaller scale features were to be investigated using E-SEM, coating the samples in gold or a similar method as is often done (Sanfilippo et al., 2019; Vovelle, 1965) will prevent the charge buildup and make imaging easier.

3.2 Tube structure

Results

Apart from these small scale features, the tube itself is also structured. As mentioned in the previous paragraph, inside the tube we can find a thin organic sheath. Behind and partially embedded into the inner sheath a layer of flat grains is present, structured like floor tiling with grains neatly arranged next to each other. This layer is only a few grains thick. As such, it produces a curved but smooth inner lining, a full circumference of which consists of about 30 grains for a tube with an inner diameter of about 3 mm. This inner lining is of mainly biogenic

origins, consisting primarily of different shell fragments and other flat grains (figures 3.2.1 and 3.3.2). The smoothness of the inner lining is notable, the maximum relief on the inside of the tube is about 30 µm (figure 3.2.2).

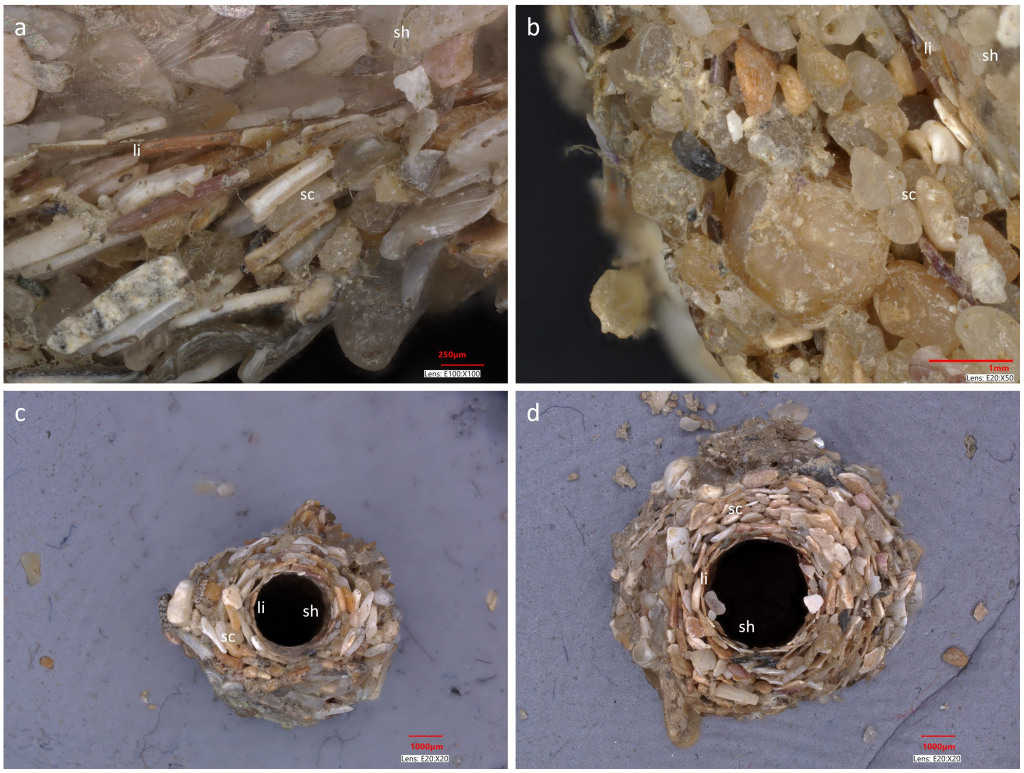

Figure 3.2.1: Digital microscopy images of the structure of a tube from several perspectives. Note that these are from different tubes and locations. The letters indicate the different areas present in the tube: li=lining, sh=sheath, sc=scale-like outer layer. Subfigures a) and b) show a cross section through the tube wall, with the organic sheath on the inside, an inner lining of flat grains along the wall and a scale-like outer wall. Note the different grain morphologies (flat vs. spherical) used in tube construction. Even when grains are more spherical as in b), they are aligned with their long axis vertically along the tube walls.

To the outside from this inner lining, an outer layer of grains can be found as displayed in figure 3.2.1. These grains can be made up of both flat (figure 3.2.1a) and spherical (figure 3.2.1b) grains. Looking at figure 3.3.2a, these flat grains can be sharp and are very often shell fragments. In either case they are placed with their long axis parallel with the tube axis. They are placed in a scale-like manner, with grains partially overlapping. This scale-like structure is also clearly visible in the top view of the tubes as a layered structure (fig. 3.2.1c/d and fig. 3.3.2c, labeled 'sc'). Notice that although in many cases the tube consists nearly solely of flat fragments (fig. 3.2.1d), or of rounded grains (fig. 3.2.1b), a mixed construction is also possible as in figure (fig. 3.2.1a). This mixed construction is more rare than a tube made up completely of rounded grains which is in turn more rare than a tube consisting of flat fragments.

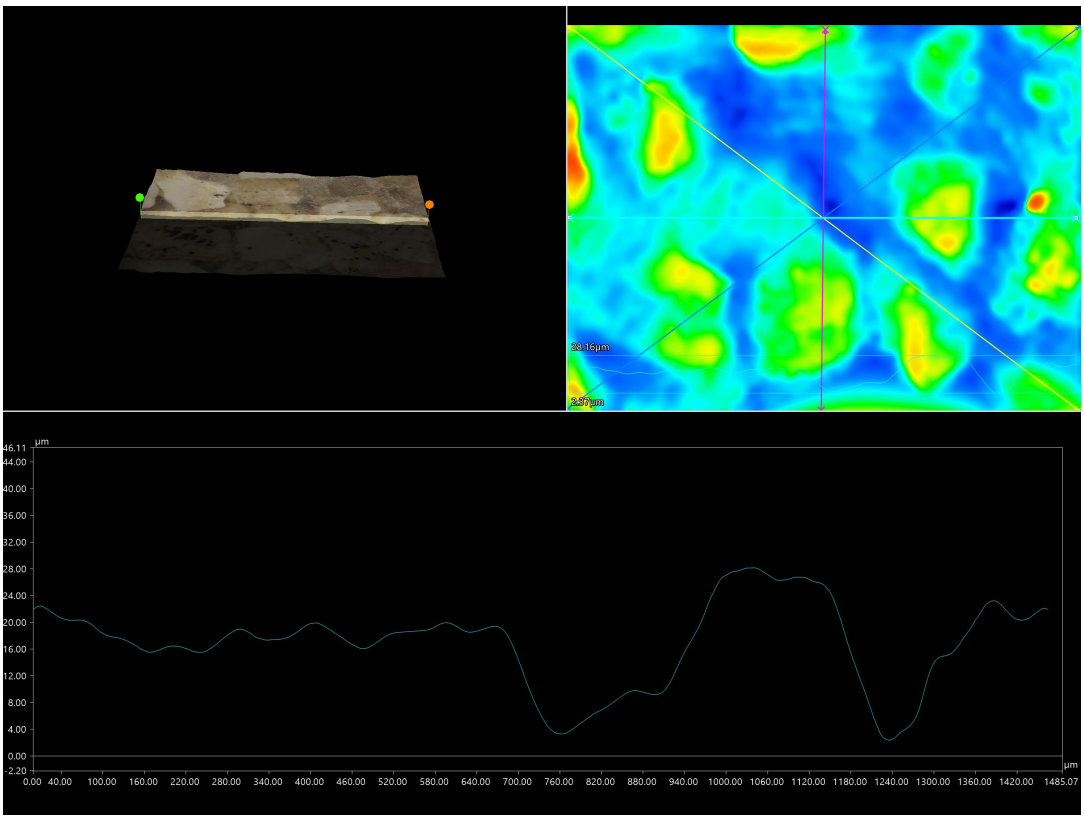

Figure 3.2.2: Arch-corrected height map images and profile of the inner surface of two tubes. The profile is drawn along the light blue line visible in the top right corner. Colours refer to the relative height, with red spots being high and blue being low. They show a relief of about 30 µm along the sections made. The underlying grains can be seen in the profile to form a relative high surface.

Interpretation & Discussion

This means that the tubes are found to have a two-layered structure in terms of grains: one flat inner layer and one scale-like outer layer. This is in accordance with the work of Fournier-Sowinski (2013) and Vovelle (1965), but not with Sanfilippo et al. (2019), who found the tubes to have a three-layered structure with a flat, discontinuous outer layer. However, Fournier-Sowinski (2013) found the tubes of S. Alveolata to be essentially composed of shell fragments, where these results show that the use of rounded grains is also a possibility. However, as stated before, the use of flat grains seems to be preferred, which is in contrast with previous research showing the preferential use of rounded grains (Gruet & Bodeur, 1994; Lisco et al., 2020). Also, in contrast with Gruet and Bodeur (1994), sharp grains are preferentially selected, just like bioclasts which were shown to be selected preferentially by Naylor and Viles (2000) and Sanfilippo et al. (2019). Most likely, the worms are supply-limited and will select the flat grains preferentially when available, but are also able to use the round grains without problems. The use of flat grains probably allows the use of comparatively fewer grains or to build in a smaller space. They may also offer advantages in terms of strength and resistance to wave energy.

However, not all tubes are created equal. In general, tubes with smaller openings also have thinner tube walls. As they have the same structure and similar inner layers, the difference is located in the thickness of the scale-like outer layer. This is illustrated by figures 3.2.1c and 3.2.1d but also by the tubes in figure 3.3.2. Also, contrary to statements made by Fournier-Sowinski (2013), but in line with observations by Vovelle (1965), tubes were found to be mostly of constant inner diameter and not cone-like when studying reef blocks which were detached at their base.

This tube structure does raise questions on the construction sequence of tubes. Previously, it has been found that tubes were built from the outside to the inside with active construction only on the top of the tubes (Vovelle, 1965). This conforms to the scale-like layering of the grains, with the tips sticking up and out. This would make it very hard to place grains on the outside of the tube. In this sequence the inner lining and the inner organic sheath are placed last, in that order.

Suitability of Method

For studying the structure of the tubes, digital microscopy has proven a valuable tool. Especially the digital Keyence microscope is useful, as the samples have a strong relief. Because of this, studying the samples under a normal light microscope has proven difficult. The advantages of being able to make depth-composition images using the digital microscope has proven valuable, as it allows a much greater focus depth as well as digital image correction.

3.3 Block Structure

Results

Reef blocks of the S. Alveolata are made up of many attached tubes. These single tubes have their own particular structure as described in the previous section. However, they are also attached to each other and to the substrate and in that way form particular structures. On the outside of the tubes, glue spots are visible. (figure 3.3.1a). However, fewer glue spot are observed on the outsides of the tube compared to the amount of glue spots between particle layers.

Adjacent tubes do not share any particle layers. This makes for an irregular structure. Figure 3.3.2c is a good example of this. It shows that adjacent tubes can have different diameters and wall thicknesses. Because of this, irregular voids of different sizes can be found throughout reef blocks as can also be seen in that photo.

Also, the attachment area showed several tubes using the substrate as part of the tube wall. This shows that the tubes are directly attached to the substrate as well. However, mCT images also show that in some places grains from different tubes do interlock contributing to their binding together (figure 3.3.1b). These images also show tubes left by S. Alveolata that are infilled with sediment as they are no longer closed off by the animal inside (figure 3.3.3b).

A small (cm-scale) section of reef was also analyzed for its porosity and void ratio. The dimensions and tubes inside this piece of reef are visible in figure 3.3.3a. This piece was shown to have an overall porosity of 29% while tubes were 20% of the total volume of this sample. In total, an amount of 1.55 cm^3 was studied, due to constraints in sample size at the resolution (10 μm) necessary. However, such a small piece is not fully representative for the reefs as a whole as it does not contain the large voids that are often seen inside the reefs.

The amount of voids and their sizes vary as can be seen in the photos in figure 3.3.4a/b. This is a consequence of the way in which the reefs are built up. This construction can be seen from the digital reconstruction of the tubes inside the reef block as displayed in figure 3.3.5. Figure 3.3.5b shows the top of the block, while figure 3.3.5c shows the bottom of the block. The difference between the two is notable. On the bottom, the tube density is smaller than at the top. At the same time, the tubes are generally smaller in diameter than at the top. Together with this, the way the reef is built is also visible and is cause for the development of these voids. On the bottom side of the reef, where it used to be attached to the substrate tubes are positioned parallel to the substrate. They grow along the surface of the rock until, after a few centimeters, they meet and start to curve upwards. This growing upright is visible in figure 3.3.5c and has been observed in nature by Gruet (1972). This is often in a spiralling fashion from the substrate (figure 3.3.5b), before becoming more vertical. Not all tubes start from the bottom level, some only appear more upwards in the reef. Some tubes have tooth-shaped ends on them, as seen in figure 3.3.4c. These are largely made up of flat grains, as seen in detail in figure 3.3.4d, which partly overlap to form long flat parts sticking out into the water currents.

Regarding the void spaces in the reefs, figure 3.3.6 makes clear that the void space is not only varied in its shape and size, but also in its infill. The scans show that some voids are infilled with sands, while other remain (partially) open. During dissection of the reefs, some were even found to contain pebbles several centimeters long. At the same time, scans show that some voids are even formed by the reef growing around marine life such as mussels as in figure 3.3.6. Also, these voids can be claimed by probably juvenile worms, building smaller tunnels in the void spaces, curling around existing tunnels.

Interpretation & Discussion

Glue spots have been observed on the outside of the tubes as well as grains attached to the outside of the tubes (as observed during sample preparation). As such, it is likely that the different

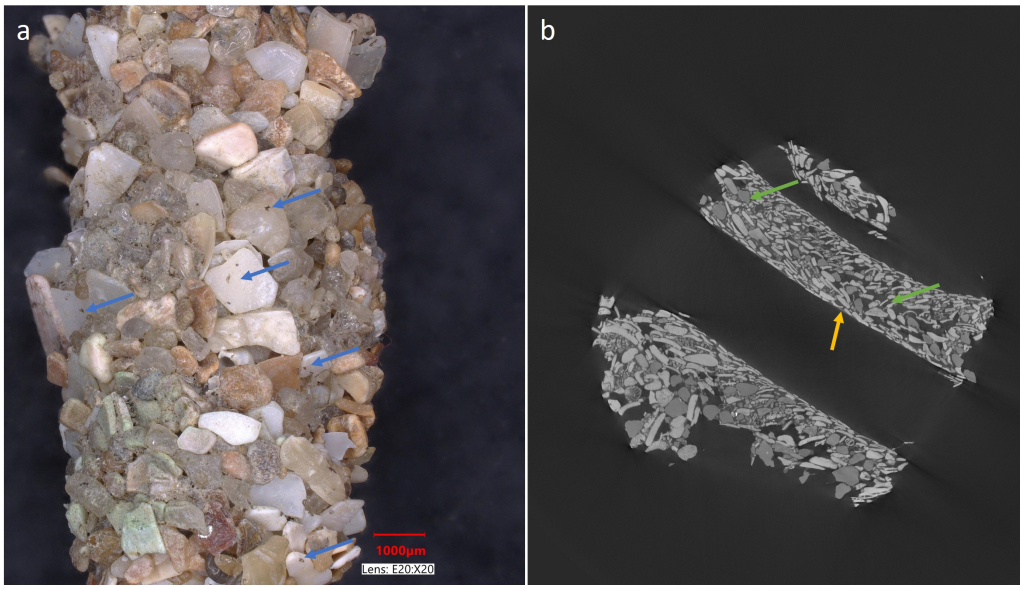

Figure 3.3.1: a) Microscopy images showing the outside of one of the tubes. Many glue spots are visible on the outside of a tube marked with blue arrows. b) mCT section though a reef block showing the inner sheath with a yellow arrow and the green arrows showing areas where the two tubes interlock.

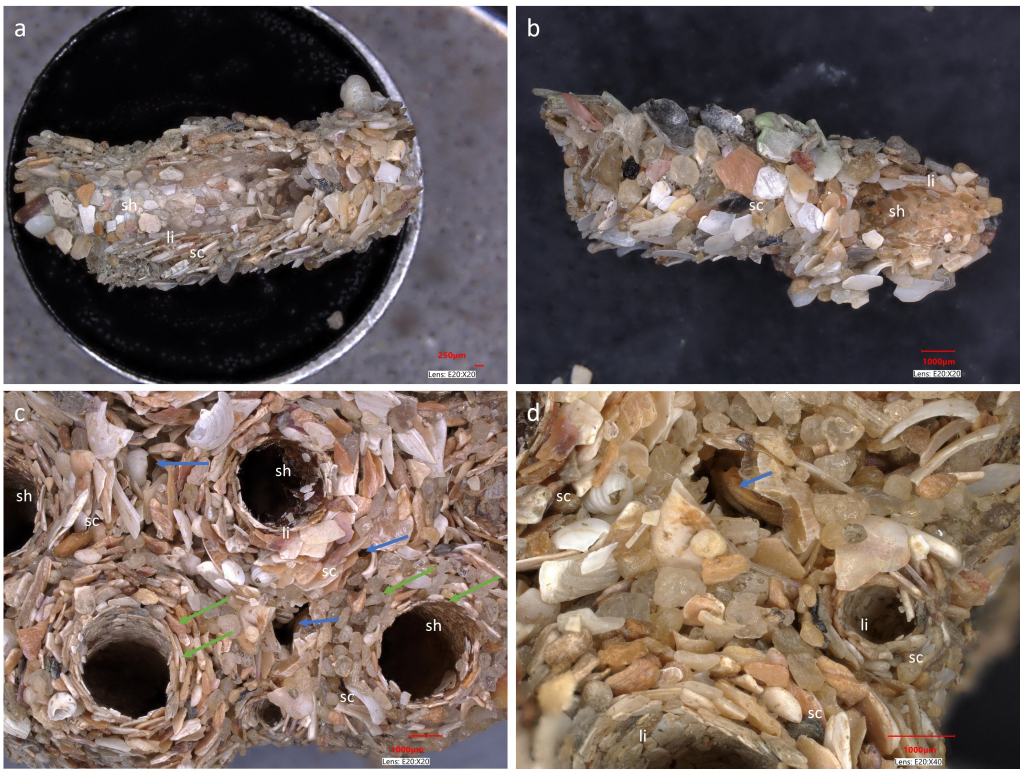

Figure 3.3.2: Digital microscopy images showing the structure of the tube aggregations. a) and b) show cross-sections of the wall of a single tube on a larger scale. c) and d) show how these tubes are interconnected. Note the larger voids present between tubes in d) (blue arrows) as well as the different grain morphologies in the different layers in the tubes (green arrows).

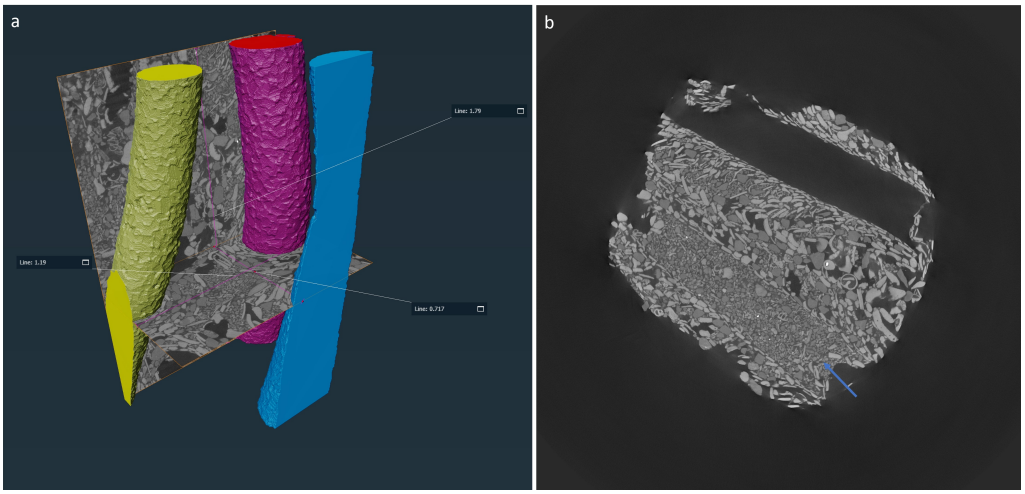

Figure 3.3.3: Detailed mCT images from some small reef section. a) shows the tubes and scale of the block analyzed for its porosity. b) shows a section through a small block, showing an infilled tube (blue arrow), which is filled with smaller grains than the tube material itself.

Figure 3.3.4: Photos of collapsed and intact reefs in the field, showing the extraordinary amounts of heterogeneity inside the reef materials, especially where they are attached to the substrate (Green arrows). Even when tubes form relatively homogeneous masses as in a), small holes and crevasses are still present at the base (blue arrows). Also note the presence of mussel shells in photos a) and c), which are sometimes incorporated into the tube blocks. Photo locations are as follows: a) 5.3, b) 5.3, c) 6.1C, d) 5.2. The orange arrow indicates the viewing direction of b) on a).

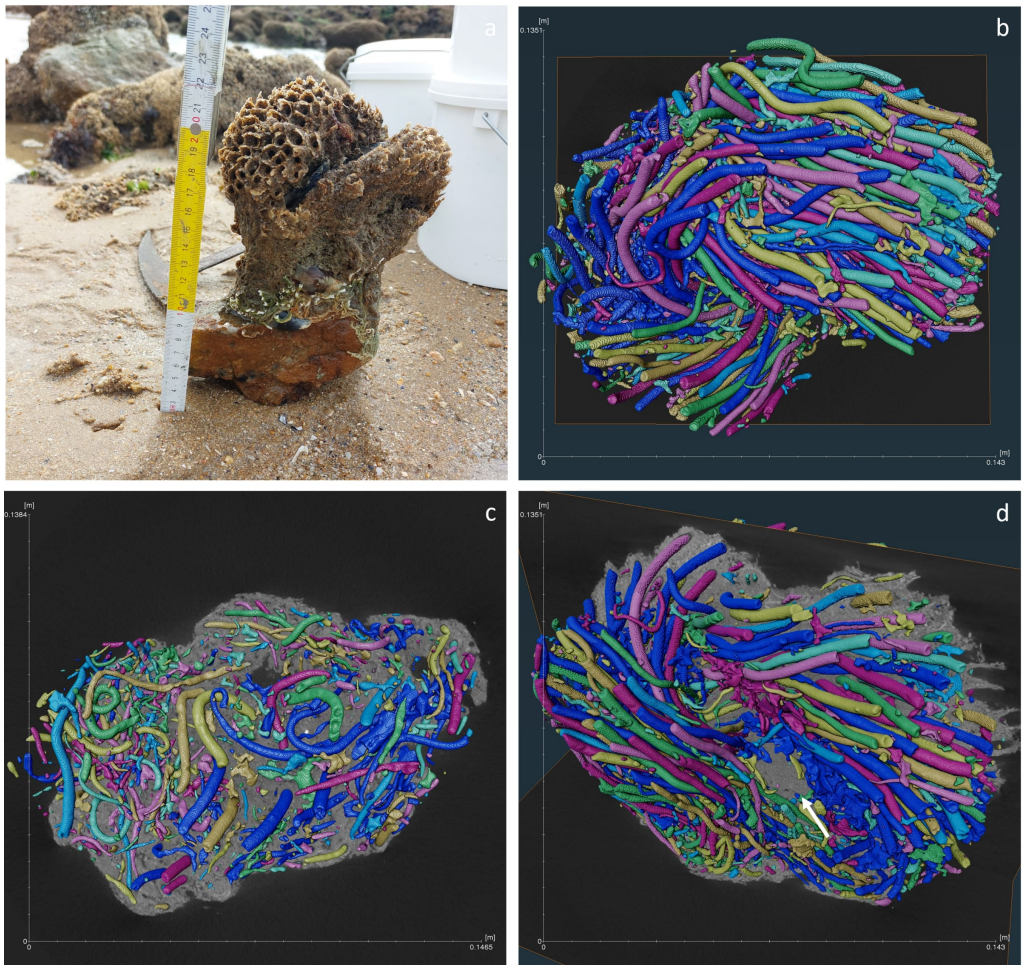

Figure 3.3.5: Digital rendering of the tubes inside a small reef block made from a mCT-scan. The cross-section in b/c/d is about 13 by 13 cm. Subfigure a) shows the block as found in the field at location 6.1C with a measuring tape for scale. b) is a top view of the tubes in the blocks while c) is a view from the bottom of the attachment area (around 10 cm mark on the tape measure). d) shows the large and partially sand-filled crevasse (white arrow) that is present in the block (around 18 cm mark on the tape measure). It also makes visible the curving and spiralling nature of the tubes in this block.

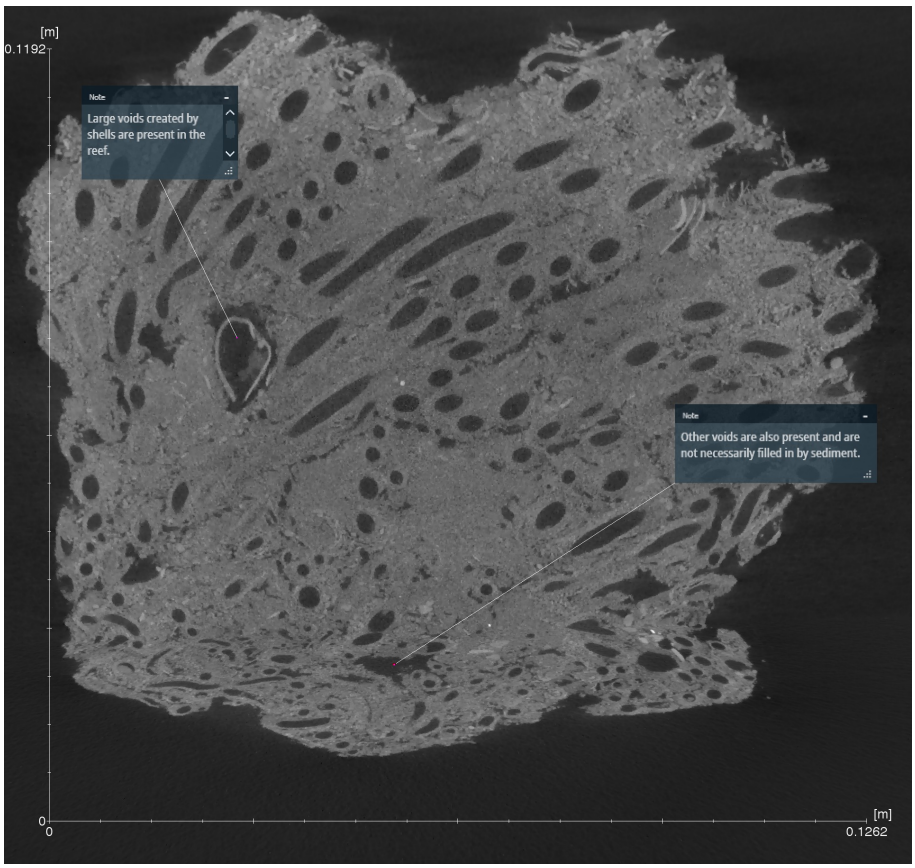

Figure 3.3.6: mCT slice through a reef block with some annotations on the void space and its structure.

tubes are attached to each other with similar glue spots as inside the tubes. However, given the interlocking of grains observed between tubes, this is not the only way the tubes stay together. As such, the behaviour of the reefs is probably governed by both these mechanisms.

Given that the reefs contain a large amount of voids, different tube directions and a difference between the amount of glue spots inside/outside the tubes, as well as occasional interlocking of tubes suggests significant anisotropy in their behaviour. Also, as the direction and scale of looking at the reefs strongly influences what effects and which heterogeneities need to be considered in its behaviour, the behaviour is also likely to be strongly scale-dependent.

Not all tubes in a reef are inhabited by S. Alveolata. Tubes can be left and recolonized after some time (Curd et al., 2019). This explains the infilled tubes seen in the reefs. These are infilled when they are left by the inhabiting polychaetes. This also leaves room for the preferential settling mechanism for the S. Alveolata larvae, which preferentially settle existing tubes so that they do not have to build new tubes (Curd et al., 2019). This also explains why most tubes are the same size, as new tubes build by juvenile worms are rare.

It has also been shown that tubes change direction while the reefs are growing. It is likely that this is to orient themselves into the prevailing currents in such a way to capture food and sand particles while protecting the tubes from infilling. For this same reason, the tubes have tooth shaped ends. These have earlier also been observed by other researchers (Fournier-Sowinski, 2013; Sanfilippo et al., 2019; Vovelle, 1965).

It is not entirely clear what determines the final shape of a reef block. Although the patterns described here are widely recognizable in the field, they can ultimately result in different large-scale structures. This difference is illustrated by figures 3.3.4a & b. They show the same horizontal start and upwards growth but are very different in their final structure with the reef in figure 3.3.4b having far more and larger voids with very irregular shapes as compared to the reef in figure 3.3.4a. It is most likely that for a large part, the shape of the blocks is determined by the local hydrodynamic conditions (Fournier-Sowinski, 2013), which in turn determine sediment and food flows which are key to the survival of the worms.

In many regards, it can be concluded along with Fournier-Sowinski (2013) that the reefs are characterized by a strong spatial heterogeneity on all scale: from tube to block and between different locations.

Suitability of Method

The methods employed to investigate the reef structure were generally found to be very suitable to the investigation done here. The only downside in the investigation is the necessity for smaller samples in order to get a suitable resolution for the analysis of porosity. As a result of this, the sample analyzed for that purpose is not fully representative of the reefs as a larger block. This is because not all the scale effects can be captured in this way. In order to minimize this problem, small samples should be prepared and shaped carefully, but the problem is to a large extent unavoidable.

3.4 Grain size

Results

Samples for this experiment were produced from a block that was cut off close to its base at location 5.3. From this block three different tubes were cut and any debris from other attached tubes was removed, resulting in three tubes approaching 10 cm in length. As such, almost the full length of the tubes was used in the experiments.

Before doing the particle size measurements, a first look is taken at the grain sizes with the naked eye. In figure 3.4.1 it is clearly visible that the fragments contain a significant coarse fraction. Similarly it is visible in many of the photographs in previous sections that many coarser grains are present inside the reefs.

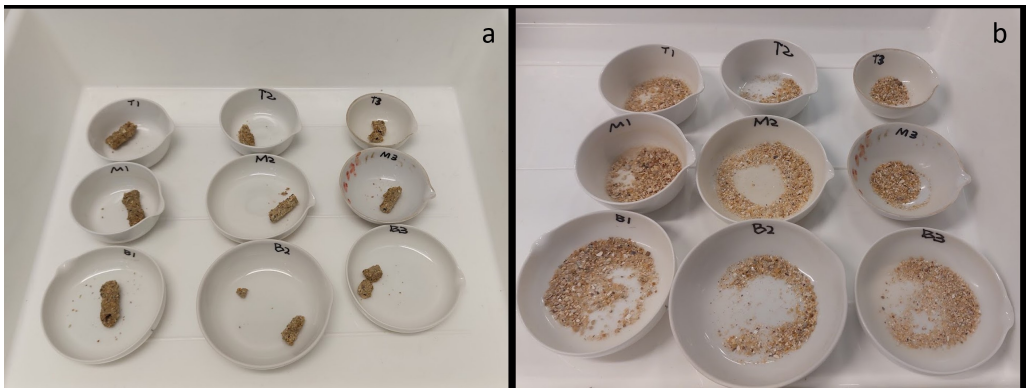

Figure 3.4.1: The tube parts analyzed for particle size distribution a) before and b) after the breakdown of organic material. For size reference, the largest ceramic dish is approximately 10 cm in diameter, and most samples are about 2 cm in length.

Looking at the raw data in figures C.4.3-C.4.5, it is clear that a part of the measurements done is not a realistic reflection of the properties of the reef materials. The coarse fraction visible with the naked eye is often not present or underrepresented inside the measurements. At the same time it has been observed during experiments that many coarse fragments can get stuck inside the tubing of the Malvern MasterSizer. As such, only measurements which give at least 10% of the material in the coarse sand range (>500 μm) are taken into account. As such, the grain statistics per tube part are included table 3.4.1. Samples that did not meet the criterion are indicated with NaN values.

After applying the filter as mentioned above the resulting size distributions can be plotted for the different tube parts. The particle size distributions in figures 3.4.2 show a clear bimodal distribution with distinct peaks at 1 mm and 10 μmm. Some measurements also show a third peak at 0.5 mm. It is notable that the grain statistics show no development in grain sizes with the length of the tube (table 3.4.1).

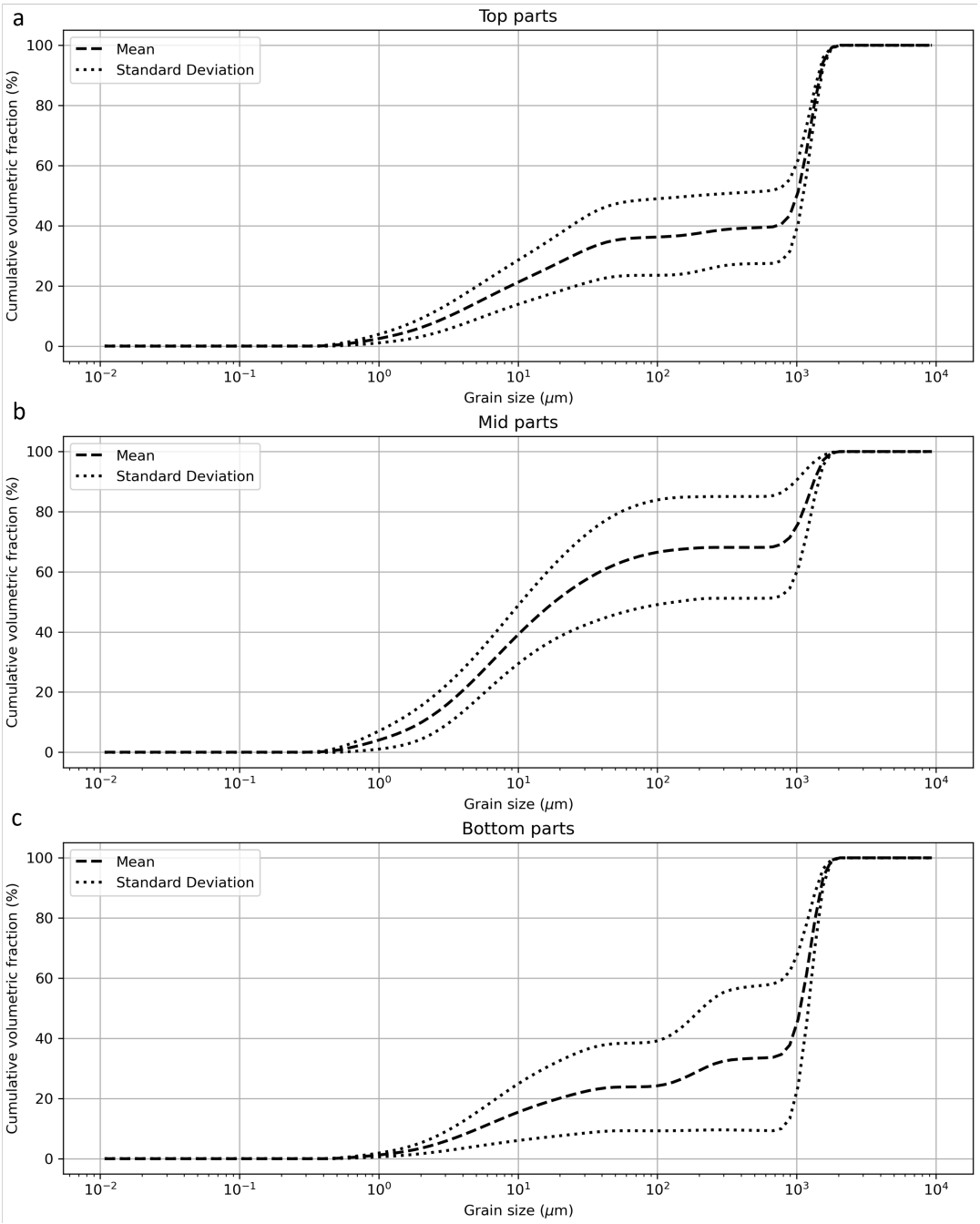

Figure 3.4.2: Cumulative particle size distributions for the top, middle and bottom parts. Displayed are the mean ± one standard deviation from all measurements.

	d10 (μm)	d50 (μm)	d90 (μm)
T1	3	905	1554
M1	1	13	922
B1	nan	nan	nan
T2	110	320	1431
M2	3	251	1414
B2	4	346	1431
T3	9	1073	1570
M3	nan	nan	nan
B3	293	1291	1644

Table 3.4.1: Grain size distribution parameters from the different sections of single tubes. T= top, M=middle, B=bottom, while the numbers denote which tube it is a part of. Percentiles are with regard to volume here.

Interpretation & Discussion

The grain sizes found through applying a filter are representative of the different grains used in tube construction as outlined in previous sections. The largest grains, which represent a large percentage (around 40-60%) of the total volume are those large flat grains, which are most preferentially used in construction of the grain layers by the adult worms. They are used in the construction of the inner and outer linings as seen in figure 3.2.1a. The second peak, at 0.5 mm roughly, is not present in all tubes sections. If present, it represents 5-20% of the total volume. These correspond to the rounded grains that can sometimes be seen in the outer linings of the tube walls as in figure 3.3.2d. Lastly, many smaller grains are also present which cannot be seen from our imaging, but have probably been washed into the reefs by the waves. They are represented by broad peaks around 10 μm, which contribute around 15-60% of the volume, depending on the sample. It is however highly likely that these percentages are actually a lot lower due to the fact that these grains could flow freely through the MasterSizer in contrast to large flat grains. Sanfilippo et al., 2019 reported particle sizes of 0.5-l.3mm for the skeletal fragments found in the reefs, which is very similar to the 1.0 mm found in this study. Also, the lithic fragments reported there were 0.2-0.6mm, which show similarities to the 0.5 mm fragments found in this study. However, most other researchers have found much smaller grain sizes to be used preferentially, specifically 125-500 μm (Multer & Milliman, 1967), 500 μm (Vovelle, 1965), 150-600 μm (Gruet, 1984), 290-420 μm (Naylor & Viles, 2000), 250-700 μm (Nicoletti et al., 2001) and 400-700 μm (Delbono et al., 2003).

Several authors have noted that the selection of grains by S. Alveolata is linked to the size of the worm, with larger worms selecting larger particles (Gruet & Bodeur, 1994; Lisco et al., 2020; Naylor & Viles, 2000). As such, an enlargement of grain sizes would be expected towards the top of the tube, especially with a horn shaped tube (meaning a constant enlargement rate) like suggested by Fournier-Sowinski (2013), and indeed this has been found by Vovelle (1965). However, Vovelle (1965) also noted that tubes open very quickly and mostly have a constant diameter, with the thinner parts of the tube having a length of 8mm on average. Given this, it is possible that the tubes were not cut close enough to the substrate. However, this tube form was also not seen during CT-scanning in which the block was cleanly separated. Also, tubes growing attached to the surface found during the field work do not show this horn shape (figure 3.4.3). As such, it is probably the case that the mechanisms of reef growth are not fully understood and it is likely that tubes and consequently reefs are reconstructed during the year. This would also explain the seasonal variation in tube density (Gravina et al., 2018; Lisco et al., 2020).

Reflecting on the grain sizes, the first tube (T1/M1/B1) results stand out with a large difference between sections in d50. For the other tubes, these are far more comparable. This probably has two different causes. One is the small amount of measurements for sample M1, even when compared to sample T1. This suggests that the measurements on sample M1 are probably hampered more than others by samples getting stuck inside the Mastersizer (as will be discussed later). Given this, the results should be taken with caution, as it is likely the proportion of coarse grains is underestimated, even when filtering the results as done here.

Even given all of these restrictions, the distribution of the particle sizes suggests active selection of particles based on size. Given the findings in section 3.2 we also see that large flat grains, often of

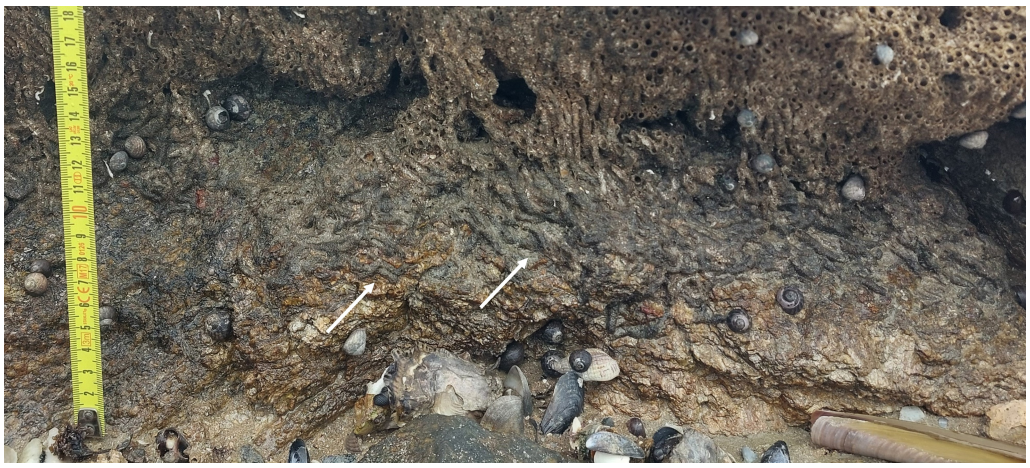

Figure 3.4.3: Photo taken close to field work location 6.1B showing tubes growing parallel to a rocky substrate. Note the constant diameter of the tube, without showing significant thinning at their ends (white arrows).

biogenic origin, are preferentially selected above rounded grains. This is in contrast to Gruet and Bodeur (1994) and Lisco et al. (2020) who found a preferential selection of ovioid particles and no selection of sharp shell fragments. These findings are more in line with the work of Naylor and Viles (2000) and Sanfilippo et al. (2019), who found similar results. However, care should always be taken as the standard for particle size distributions is generally mass-based, not volume based. As the correlation between sieving methods and laser diffraction is dependent on the particles being tested, direct comparison is not possible (Beuselinck et al., 1998).

Suitability of Method

As has been mentioned before, during experimentation it was noted that especially the flat, coarse grains were seen getting stuck inside the tubes of the equipment. This led to skewed measurements necessitating filtering of the results. Where this was found to be an issue during experimentation, care was taken to resolve this issue by moving tubes around. However, even with these adjustments, the flow speed of larger particles was lower than that of the water itself (which carried the smaller grains). As the stirring and flow speeds were already at their maximum setting, this could not be adjusted any further. Given that the maximum grain size of the apparatus is published as 2 mm, this should not have posed much of a problem. In this case, the flatness of the grains was probably the problem, as this shape generates less lifting force than rounded particles and as such is less easily carried by the water. Given this, it is unavoidable that measurements are skewed to some degree. As such, a repeat of this experiment is recommended at a later time, using a different method such as a sieving method or by manual separation. These methods need a much larger sample size though, which poses its own problems. As such, the best candidate is probably to use image analysis methods with automated measurements, for which also good correlations do exist with the mass-based distributions (Fernlund et al., 2007), allowing more direct comparisons.

At the same time, the effect of the hydrogen peroxide grain separation method is not known currently. This may have influenced the grain measurements by breaking down some materials. However, this could not be ascertained.

Another issue which needs to be considered is the influence of grain shape on the analysis using laser diffractometer. It has been shown that non-spherical particles do not produce accurate resuls given that the measurement is dependent on the orientation of the particles in the laser beam. This effect is strongest in rod-shaped particles (Naito et al., 1998). For sand particles, Polakowski et al. (2014) determined the influence on measurements with the Malvern Mastersizer to be small, but also warned that the results may be different for less spherical sands. Given the observations done under the microscope, the grain sizes found here do not seem far-fetched although the exact percentages may be off, as stated before. Given these factors, it would be wise to approach the grain size distributions given here with some caution.

All these possible problems with the measurements result in a large standard deviation (figure 3.4.2). This is especially the case at the middle peak at about 0.5 mm. This may be because this peak is not just a result of some sands actually in that size, but may also be because flat grains

not oriented fully obliquely to the laser may result in a wide range of measurements between the maximum and minimal possible measurement of the grains.

3.5 Grain mineral composition

Results

Four different sands were used in these experiments. One sand from location 6.1B was collected on the beach a few meters away from the reefs. The sand from location 5.1 was a sample of intertube sand. As can be seen from figure 3.5.1, even before analyis the samples show slight differences. The samples from Noirmoutier (location 5.1) show a lighter color and appear coarser than the samples from location 6.1B.

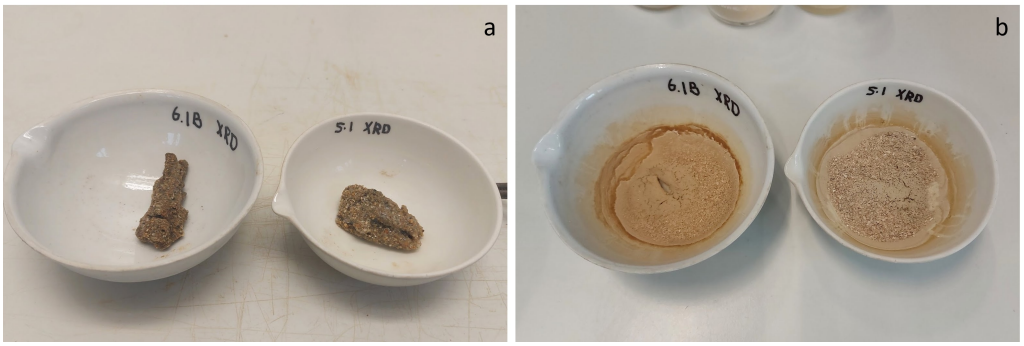

Figure 3.5.1: Photos of the samples used in P-XRD before (a) and after (b) disaggregation. The resulting sands were later crushed up to be used for powder analysis. The samples are approximately 5 cm in length. The samples from Noirmoutier (5.1) are slightly paler and coarser when compared to those from Pornichet (6.1) which are finer and more yellowish in appearance.

The grain mineral composition was analyzed through P-XRD as outlined in section 2. From the analysis we know that in the sands from location 5.1, the minerals quartz, calcite, muscovite and aragonite were present, with possible traces of microcline, albite and dolomite. In the tubes from location 5.1, the minerals quartz, calcite and muscovite were present, without traces of other minerals. At location 6.1B the minerals quartz, calcite, aragonite and dolomite were also present with possible traces of muscovite, kaolinite and feldspar. The tubes from location 6.1B contained quartz, calcite and aragonite with muscovite, dolomite and kaolinite possibly present. The spectra from the different locations used for the analysis are present in figure 3.5.2.

Interpretation & Discussion

The original color of the different samples already differs per location. This already points to differences in mineral composition. This difference would be mainly having more (typically) lighter coloured minerals such as quartz and calcite at the Noirmoutier location, probably mostly from shell fragments. Meanwhile, the more yellow color is generally a result iron oxides in the grain (Nichols, 2009). However, it could also be explained by a difference in grain sizes.

The origin and presence of calcite and aragonite is unsurprising. These are both minerals commonly used by different sea creatures to build their shells. For example, aragonite is commonly used by several mollusks in shell construction (Nichols, 2009), fragments of which are preferentially selected (Fournier-Sowinski, 2013). Given that the reefs concentrate calcite with higher percentages of calcite inside the reefs compared to the sediment (Fournier-Sowinski, 2013; Vovelle, 1965), the presence of large amounts of calcite here is no surprise. Quartz is a common sand mineral and often a product of erosion. The presence of muscovite at Noirmoutier is explained by its closeness to the Loire Estuary which provides sediments to the area and which flows through an area shaped by strong past tectonic activity, providing plenty of metamorphic rock fragments, just before emptying into the sea. Combined with the local geology consisting of old volcanic and metamorphic rocks, which could also supply materials like micas, their presence is to be expected. The area at Pornichet consists of these same materials though, so it is likely that muscovite is also present there, but maybe in lesser amounts (Maréchal & Rouillard, 2020).

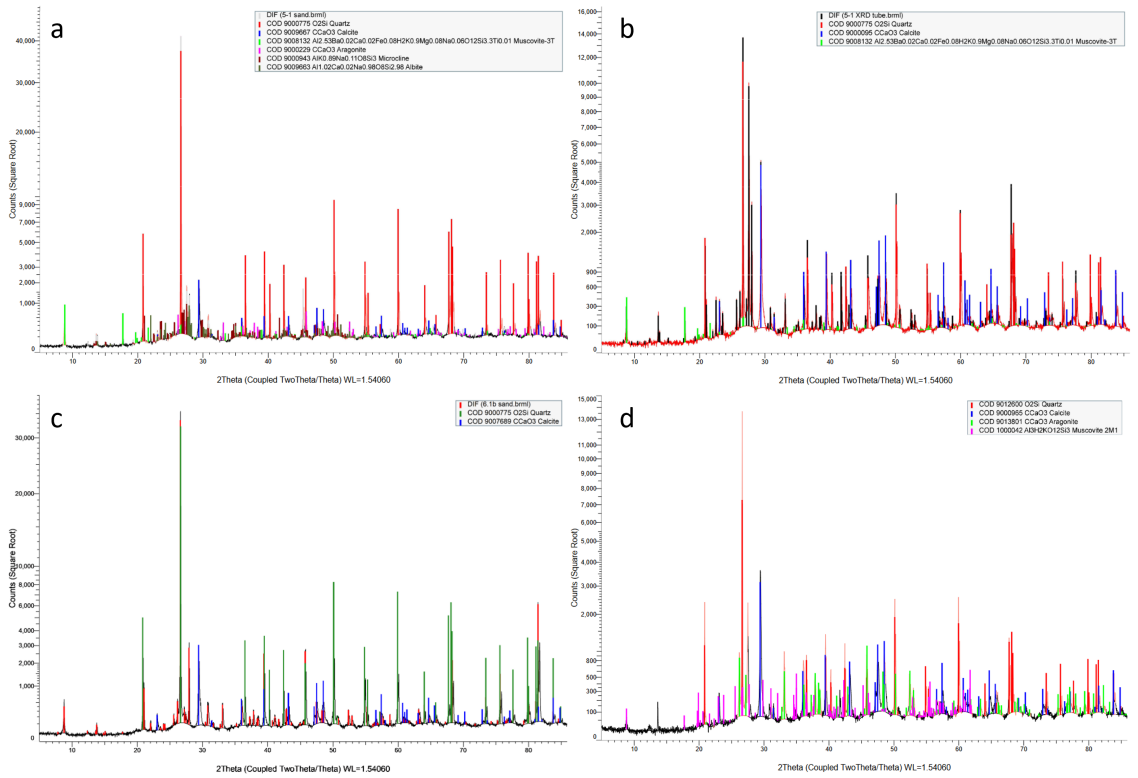

Figure 3.5.2: Powder X-Ray Diffraction spectra from the analysis of powdered beach and tube sands. a) is from sand from fieldwork location 5.1. b) is from sand from a S.A. reef at location 5.1. c) is from sands collected from location 6.1B. d) is from S.A. reef fragments collected near location 6.1B.

The presence of dolomite is probably due to the suppresion of calcite or aragonite through direct secretion from the seawater as a result of the strong hydration of Mg-ions, but this is not entirely clear (Haldar & Tišljar, 2014). As such, not all differences shown in the samples may be as strongly present in the overall area and may be linked to the complex local hydrodynamic conditions leading to concentration of some minerals over others. Given that muscovite is a platy mineral from which flat fragments are commonly found, this will be preferentially selected by the worms. As such, in an indirect manner, the S. Alveolata do seem to concentrate certain flat and platy minerals as they offer advantages in and are necessary for the construction of their tubes.

Suitability of Method

The downside of the P-XRD measurements done here is that they are purely qualitative. To improve the measurements done here, quantitative P-XRD measurements would be able to show the exact proportions of the different minerals present inside the reefs. This would far better show the effects that the S. Alveolata have on the mineral composition of their reefs compared to the surrounding sands. Another good solution is to perform petrographic analysis on thin sections cut from resin impregnated reef blocks with a light microscope. Alternatively, mCT can be used to classify grains based on grey values and shapes.

3.6 Glue spots measurements

Results

Given the characteristic grain bonding and structuring found within S. Alveolata reefs, it is important to investigate how the different grains are bonded to each other. The results from this part of the study are summarized in table 3.6.1. In total 41 grains from location 6.1A and 51 grains from location 5.3 were analyzed, with 109 and 133 glue spots measured respectively. Grains were taken from the whole tube, excluding the top part. The average glue spot size for location 6.1A is 152 μm, while this is only 86 μm at location 5.3. This size difference is also visible when looking at the different spot shapes. For rounded spots the same trend is visible: 119 μm (6.1A) vs 54 μm

Location	6.1A	5.3
Average size glue spots (μm)	152	86
Average size rounded glue spots (μm)	119	54
Average size linear glue spots (μm)	163	94
Average nr. of spots per grain (estimated)	7.6	7.1
Average nr. of spots on grain side	2.6	2.1
Average nr. of spots on grain edge	2.3	2.9

Table 3.6.1: Average spot sizes and the average number of spots on the different areas of the grains for two different sampling locations.

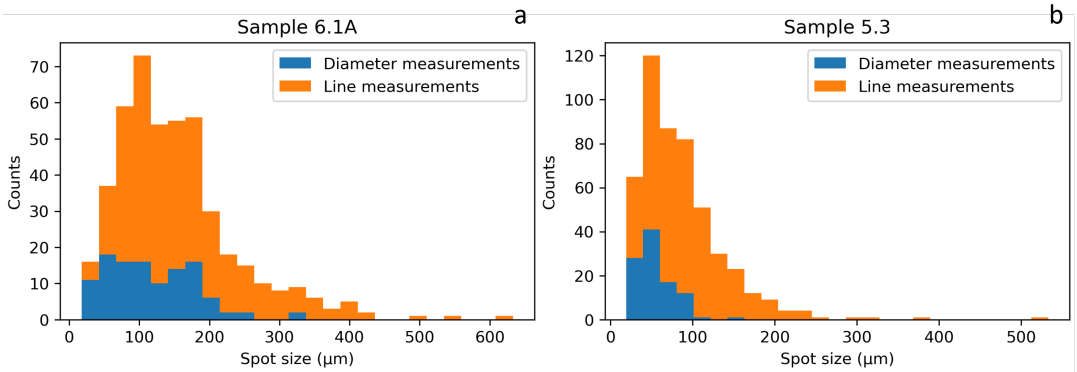

Figure 3.6.1: Histograms of the glue spot sizes of the two different samples from location 6.1A (a) and location 5.3 (b), showing similar distributions although there is are differences in spread and mean size. Note that the sizes are stacked, so in a) about 15 rounded spots and about 55 spots have a size of 100 μm.

(5.3) as well as for linear spots 163 μm (6.1A) vs 94 μm (5.3). The same goes for the amount of glue spots, which is also smaller at location 5.3. However, the distribution of the glue spot sizes is similar between locations (figure 3.6.1). They are both positively skewed, although their peaks are different: around 100 μm for location 6.1A and around 75 μm for location 5.3. The largest glue spots are also larger than 600 μm for location 6.1A while for location 5.3 this is only just over 500 μm. The largest spots which were found more than 10 times during the investigation were about 370 μm for location 6.1A and about 180 μm for location 5.3.

Together with the size, the amount of glue spots per grain was also estimated for both sample locations. The sample from location 6.1A on average had an estimated amount of glue spots per grain of 7.6, while those from location 5.3 had on average 7.1 glue spots per grain (see table 3.6.1. A difference is visible when looking at the amount of spots on the grain edge and on the grain sides, location 6.1A has more spots on the grain sides while location 5.3 had more spots on the grain edges. The distributions of these numbers are also visible in figure 3.6.2. There is a positively skewed distribution in the number of total glue spots per grain, like with the size of the glue spots. Both sample locations have their peak at 5-7 glue spots per grain, although location 6.1A has a similar peak at 1-3 glue spots.

Interpretation & Discussion

Given this, it is notable that sample location 5.3 has both smaller glue spots and less spots per grain. It was not possible to determine the cause of this, but several are possible. Grain size could be one explanation, as larger grains require more and larger glue spots for proper installation. However, although no size distributions are available for these tubes and locations, figure 3.6.3 shows that the grains from sample 5.3 are visually similar size than those from sample 6.1A, making this less likely. More likely, S. Alveolata is able to adapt to conditions in terms of building materials and speed (Buffet et al., 2017; Gruet, 1972, 1984; Lisco et al., 2021). As such, it is more likely that this increase in glue used to construct the tubes may reflect environmental pressures and conditions such as an increase in wave energy stored that needs to be dissipated or larger sediment and water flows along the reefs. This would be a topic for follow-up research.

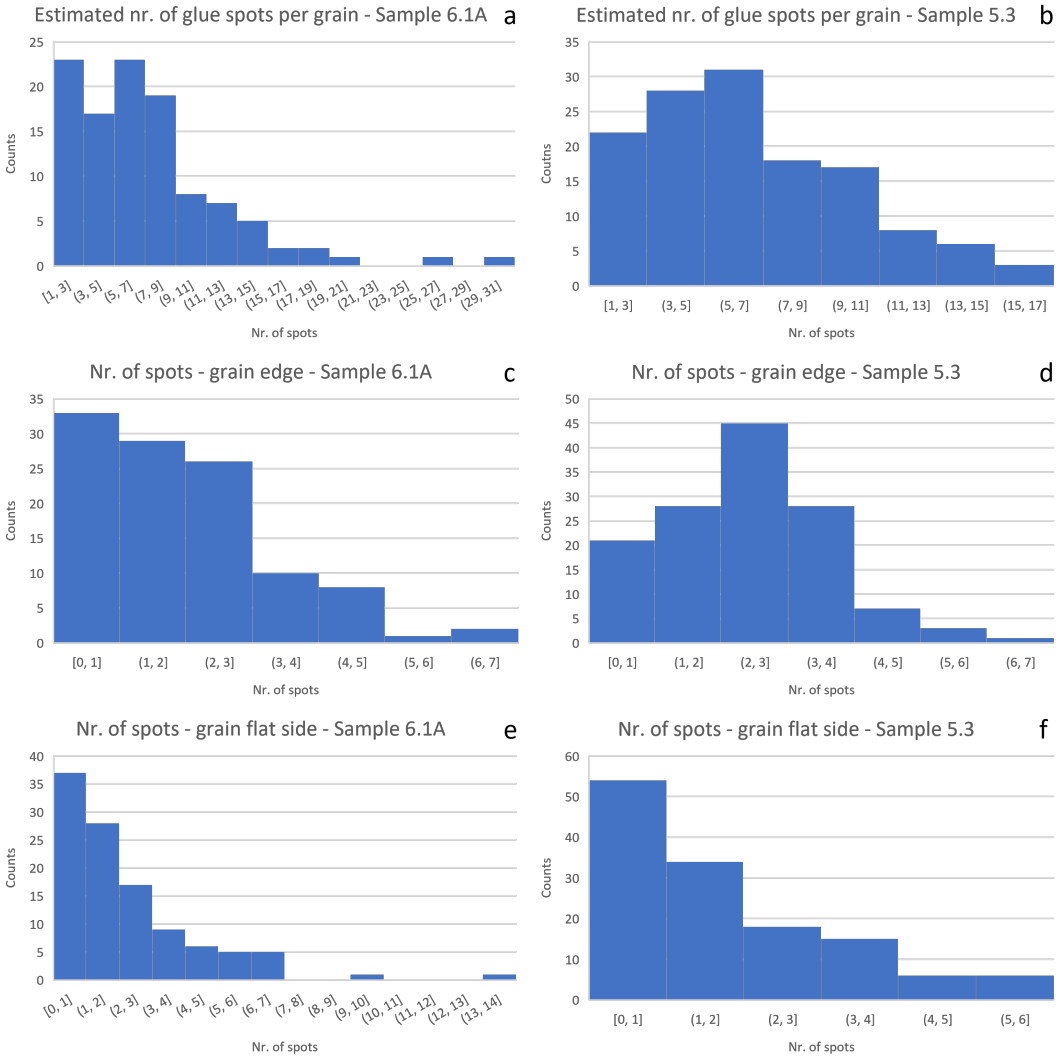

Figure 3.6.2: The amount of glue spots present on a single grain as well as their provenance (samples 6.1A is from Pornichet, sample 5.3 is from Noirmoutier). a) and b) show the estimated amount of glue spots per grain for location 6.1A and location 5.3. c) and d) show the number of glue spots found on the edge of the grains, which would be visible from the other side of the grain. e) and f) show the amount of glue spots found on the mostly flat sides of the grains. In total 41 grains from location 6.1A and 51 grains from location 5.3 were analyzed, with 109 and 133 glue spots measured respectively.

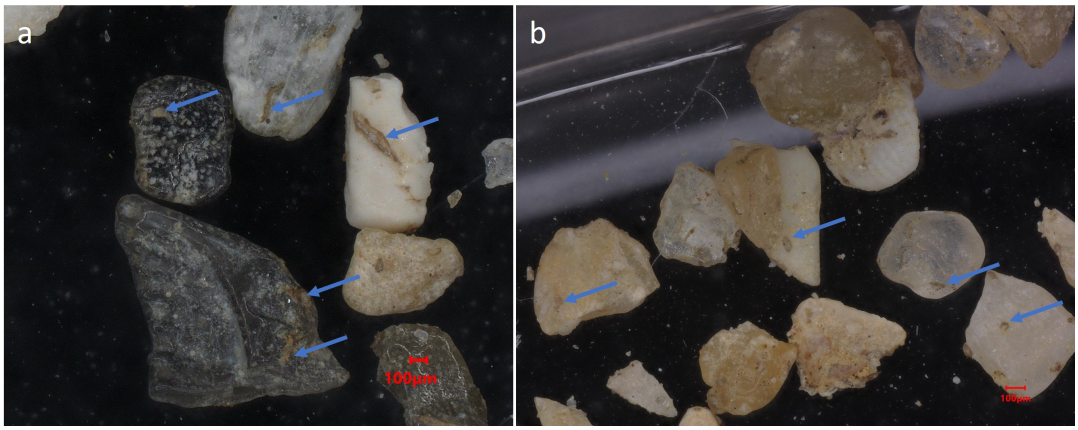

Figure 3.6.3: Photos of grains from the glue spot investigation. a) is from sample 6.1A and b) is from sample 5.3. Grains from sample 5.3 are visibly of a similar size compared to those from sample 6.1A. Blue arrows show some of the browned glue spots visible on the grains.

Suitability of Method

Although the basic method used in this sections has its benefits, it also presents some challenges and flaws. Since tubes were mechanically disaggregated before analysis, there is always the possibility of particles breaking. This is especially possible with the thin and flat particles often encountered in the S. Alveolata tubes. This would reduce the numbers of spots encountered per grain. However, no signs of particle damage were spotted during the investigation.

Also, this method assumes equal number of glue spots on the hidden and observed side of the grains. There is no reason to doubt this assumption, but also no direct observations which confirm this. However, since grains are layered next to each other, it is likely that this assumption is correct for most grains. The grains on the in- or outside of the tube are the exception to this, with observed differences in the amount of glue spots per side.

A more interesting issue is the detachment of grains and the behaviour of the glue spots. Two basic mechanisms are possible, dependent on the adhesive properties and strength of the glue. On one side, glue spots may detach completely from one of either grain. In this manner, the glue stays intact while it detaches from one of the grains. On the other side, the glue may split between grains, leaving two grains with traces of the glue spots. Looking at the different spots indicates that this second is closer to reality, with only broken glue spots observed during counting. This is relevant as the first mechanism may lead to underestimation of glue spots when using the methods done here, especially when not studying many grains.

Also worth discussing is the choice to measure glue spots using either their diameter or length, as this implicitly includes a classification of the glue spots. Although this rough classification has been observed in this thesis and has also been published by (Sanfilippo et al., 2019), it remains a simplification of reality. As such, interim cases do exist, where their shape classification could remain up for discussion although not at such a scale that it would invalidate the results here. Given this problem, a more intricate classification using mathematical methods to classify roundness, accompanied by automated measurement might improve the results here and shine more light on the attachment mechanisms of tubes and the behaviour of the glue.

3.7 Summary

In the previous chapter, the structure inside the S. Alveolata reefs has been described over several scales of observations. At the smallest scale, several organic materials are observed. Mainly, the glue spots that hold the grains together inside the tubes have been confirmed to have a bubbly structure and to have two main shapes: either an elongated strip, which is used to suture together edges of flatter grain or hollow discs which are used to connect concave surfaces. The glue spots show a face-hardening effect on their outsides and the bubbles often radiate from the center of the spots. On average, a grain is connected by 7-8 glue spots which have an average size of about 80-150 μm, depending on their location of origin.

The tube of S. Alveolata was confirmed to consist of an inner sheath made of the same organic material as the glue. An inner layer of grains is partially embedded into the organic sheath, with grains placed next to each other. The outer layer of the tubes consists of grains placed in a scale-like manner, partially overlapping. As described earlier, the tubes are preferentially made of flat grains but are also found here to sometimes be made up of rounded grains or have a mixed construction. The tubes are found to be connected by glue spots and by interlocking of grains from the adjacent tubes. These glue spots are probably formed from capillary action between two grains, attaching seamlessly to the grains. The grains themselves are confirmed to be preferentially flat grains, often of biogenic origin. The tubes are built up from the outside to the inside with the inner organic sheath applied last and grow only on their top side. The reefs are confirmed to concentrate calcite and aragonite. However, reefs from one location were also found to have muscovite, a platy mineral often forming flat grain. Their structure is also reflected in the grain sizes found inside the reef, with a grain size of about 1mm making up about half of the volume of the tube. Another large fraction is about 10 μm, grains which have washed into the reef.

Reefs were confirmed to be attached to a solid base, often rocks, which were part of the tube. They curl upwards after their concentration becomes large enough and orient themselves in the currents. The reefs were found to contain many voids, which were sometimes formed by marine life such as mussels, around which the reefs have grown. These are sometimes infilled with sand or even cm-size pebbles, signifying the large currents in which the reefs occur. Also, voids may

remain empty and juvenile worms may build new tubes in between, which do not always start at the bottom of the reef. Given the diameters of the tube, the lack of grain size development and the changes in tube density over the year, it is likely that tubes and consequently reefs are reconstructed during the year.

Chapter 4

Mechanical Behaviour

In this section the results of the mechanical testing of the S. Alveolata reef blocks is discussed. Firstly, two kinds of slake durability testing are examined. Secondly, the oedometer tests performed on the reef samples are reviewed and lastly, the results from shear box testing are considered.

4.1 Slake Durability testing

Two different kinds of slake durability testing were performed as outlined in section 2. Firstly, the results from the slake durability testing on blocks will be discussed and after that the testing on single tubes is reviewed.

4.1.1 Slake durability testing on blocks

Results

Although it has been found that rounded fragments are most resistant to slaking (Ankara et al., 2016), in this case more angular fragments were used as rounding the reef fragments turned out to be very difficult with tubes separating from the blocks in the process.

Simply submerging the lumps in water does not have much effect on the blocks. As the blocks were washed in the sample preparation phase of the testing, only very few loose particles remain which can be washed out.

The slake durability testing on the reef blocks resulted in significant losses in weight. As the slaking indices (table 4.1.1) show, weight loss after the first slaking cycle already reached up to 90% for the samples from location 4.1 and 76% for samples from location 5.2. The large amount of mass loss is also visible in the photos (figure 4.1.1), which show a correspondingly large amount of volume lost during experimentation. This mass is lost exclusively in the form of single sand grains which are abraded from the reef blocks (figure 4.1.2). The experiments also illustrate that the makeup of the reefs is not exclusively sand grains. All samples contained significant amounts of larger shell fragments which could not pass through the drum mesh (figure 4.1.1). These shell fragments are often cm-size. The remains of other worm constructions are also visible (figure 4.1.1f).

The tumbling during experimentation also produces rounded fragments (figure 4.1.1). This can already be seen after one testing cycle, with small blocks remaining of a few cm in diameter in size.

Weight\Location	4.1 (Experiment 1)	4.1 (Experiment 2)	5.2 (Experiment 3)
Start (g)	511.32	522.03	519.06
After drying (g)	388.02	399.3	400.64
Cycle 1 (g)	45.13	40.83	96.59
Cycle 2 (g)	11.84	9.58	23.41
Slaking indices			
Id1	11.63%	10.23%	24.11%
Id2	3.05%	2.40%	5.84%

Table 4.1.1: Weights and slaking indices from the slake durability testing on reef blocks.

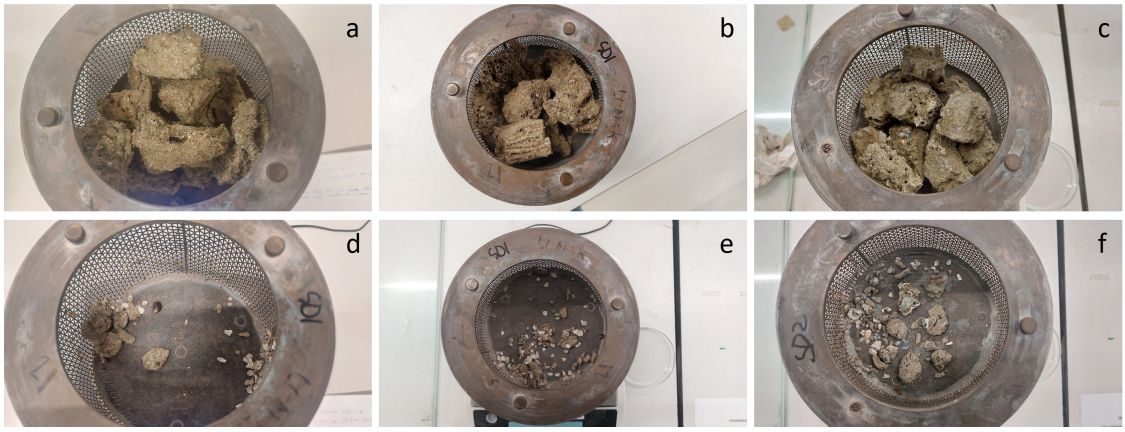

Figure 4.1.1: Before and after photos of the slake durability experiments on blocks. a) and d): sample before and after experiment 1. b) and e): sample before and after experiment 2. c) and f): sample before and after experiment 3. Note the significant losses in volume between during the experiments. For scale, the drums are about 15 cm in outer diameter.

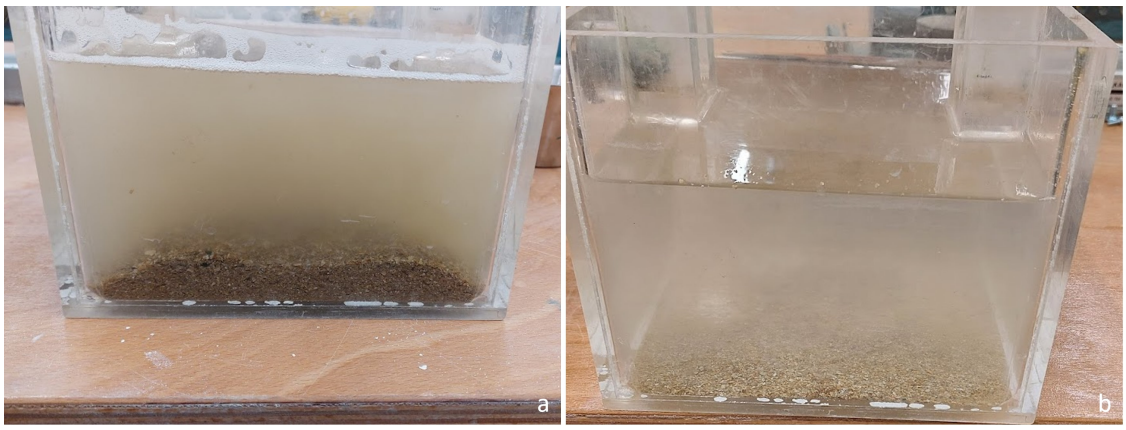

Figure 4.1.2: The debris from the slake durability experiments of sample 2. a) is after cycle 1 and b) is from cycle 2.

After one test cycle, blocks are rounded but still irregular in shape (figures E.1.2-E.1.4). After two cycles, many of these irregular blocks have been reduced to smaller fragments, often consisting of single tube parts.

Interpretation & Discussion

When looking at the result after two slaking cycles as in figure 4.1.1d/e/f, it is visible that most of the blocks which were left after one slaking cycle are no longer present and have been reduced to single tube fragments. This seems to indicate that the resistance of a single tube exceeds that of a small block of tubes. Given all of these observations, the blocks may have a critical number of tubes. Before this number, the blocks weather as a whole and their resistance is both from friction and cohesion. After this number is reduced, the blocks fall apart into single tubes which have cohesive resistance to slaking.

After neither one nor two cycles, no pattern is visible in terms of elongation of the blocks, with tube orientation inside the blocks not showing any relation to the shape of the blocks. However, only small blocks survive the slaking testing. This indicates that although there is strong spatial heterogeneity in durability of the blocks, no anisotropic behaviour is seen during testing. This is surprising, given the observation that fewer glue spots are present between tubes than inside tubes. From this observation, lumps elongated along tube direction would be expected, as the weaker planes between tubes would be failure points during erosion.

Given that the behaviour of the lumps is not as expected from observations on glue spots, it is highly likely that reef blocks also resist erosion by other mechanisms than cohesion from the glue. This confirms what was already suggested from the mCT images. Intertube friction through

particle interlocking also play a role in the behaviour of the reef. However, in all samples significant amounts of fragments from single tubes are visible. This does confirm to the observation that more glue spots are present inside the tubes than outside. As such, it is likely that a certain amount of tubes is necessary to have a significant contribution from this frictional resistance to weathering. However, it may also simply be the case that the anistropy in the cohesion is not sufficient to suppress the tendency to cut off the edges of elongated particles due to the tumbling motion during testing.

Given the previously mentioned resistance to wave action of the reefs, these results are surprising. A higher resistance to weathering would be expected of materials known for their resistance to wave-action. This might be because of several factors. Firstly, materials were taken from throughout the reefs. It is known that the reefs are the strongest near the top (Vorberg, 2000). Also, the weathering mechanism of the slake durability tests is not fully representative of wave action. This will be explored in the next section.

Compared to other materials such as cemented sands, the slaking index is very low. Ulusay and Hudson (2007) presents some values for other materials. The only material which shows similarly low slake indices is mudstone with an I_{d1} between 17-30% and an I_{d2} of about 5%. However, Hartono et al. (2019) investigated the slaking properties of a cement-stabilized siltstone. This material shows similarities to the S. Alveolata reefs investigated here, although much finer grained with only half the material of sand size. This material shows complete disintegration without cement, as would also be expected of a normal beach sand. However, with about 5% cement content this silt is stabilized and slaking indices I_{d2} become similar to those of the S. Alveolata reef blocks. However, these materials have a far larger specific gravity than the reefs encountered in this study.

Suitability of Method

As mentioned before, the resistance found from these reef material is much lower than expected. Most probably, this is also due to a difference between what was intended to be simulated with the experience and the actual conditions during the experiment. The tumbling during the experiment causes both impacts between the fragments as well as rolling abrasion over the mesh surface. This is not the same as the impact made by waves, which induce different loads such as drag and inertial forces which act non-uniformly distributed loads (Tunnicliffe, 1982). As such, a different method for testing wave loading is recommended. For example, methods like the erosion testing in a wave flume like done by Skafel and Bishop (1994) and especially Tervoort (2022) would be better suited to test the wave resistance of the material. Another option is to use the Erosion Function Apparatus (EFA) apparatus as developed by Briaud and Chen (2005). These results could be combined with regular in-situ monitoring of the reefs via remote sensing, with extra measurements after storm events allowing for modelling and prediction of influences from these events. Reassessing the slake durability method, it is a more accurate representation of the behaviour of loose reef blocks being weathered when detached from the reef. For example, during transport along the sea floor by wave action.

4.1.2 Slake durability of tubes

Results

The slake test on blocks shows that single tube (parts) are sometimes able to hold up during abrasion. As a follow up, their behaviour is further investigated using the same slake durability setup. In total three batches of tubes were tested, each with 54 tubes parts. Of these, 12 were less than 1.5 cm in length, 15 were between 1.5-2 cm, 13 were between 2-2.5 cm and 12 were more than 2.5 cm in length. A batch of tubes weighed in total between 33-38 grams with most of the weight concentrated in the class of 2.5+ cm tubes. The weights and numbers of tubes before and after testing are given in table 4.1.2.

It is clear that the total weight of tubes decreases much more than the amount of tubes. This indicates, as would be expected, that the longer tubes are far more susceptible to breakage than the shorter tubes. This is best explained by the large tubes breaking into smaller pieces which then slowly erode to single grains. Notably, most tubes were found to still have a complete and intact annulus of grains after the experiments.

		Amount			Weight (g)		
	Length Class (cm)	Before	After	Change	Before	After	Change
Run 1	1.5-	14	25	78.6%	5.72	4.51	-21.2%
	1.5-2	15	15	0.0%	8.96	5.48	-38.8%
	2-2.5	13	9	-30.8%	10.46	4.64	-55.6%
	2.5+	12	2	-83.3%	12.95	1.57	-87.9%
	Total	54	51	-5.6%	38.09	16.20	-57.5%
Run 2	1.5-	14	22	57.1%	5.68	4.70	-17.2%
	1.5-2	15	17	13.3%	8.85	5.38	-39.2%
	2-2.5	13	7	-46.2%	10.00	4.04	-59.6%
	2.5+	12	1	-91.7%	11.99	0.46	-96.2%
	Total	54	47	-13.0%	36.51	14.58	-60.1%
Run 3	1.5-	14	24	71.4%	5.19	4.37	-15.9%
	1.5-2	15	16	6.7%	7.86	5.41	-31.2%
	2-2.5	13	9	-30.8%	9.75	4.06	-58.3%
	2.5+	12	3	-75.0%	10.65	1.47	-86.2%
	Total	54	52	-3.7%	33.45	15.31	-54.2%

Table 4.1.2: Losses in weight and number of tubes during a five minute slake durability experiment presented per length class.

Interpretation & Discussion

From the results of this experiment, an estimation can also be made of the total length of tube lost during this five minute experiment. This is done by taking an average length for each class and multiplying with the number of tubes is each class (see also appendix E.1). In this way it is estimated that the total length of tube in one run during testing is 106 cm. During the experiment, 23 % of this length is lost on average making the total after the experiment 82 cm on average. Using the weights in table 4.1.2 and the estimated total length the average weight per length of the reef tubes can also be computed and is 0.34 g/cm before the experiment and about 0.19 g/cm after the experiment. This means that the length has on average decreased by a factor 0.77 while the weight per length has decreased with a factor 0.55.

Assuming a constant density in the tubes, we know that the weight per length decreases exponentially with loss of outer diameter. This is due to the volume of a cylinder being exponentially related to the outer radius. As such, we can estimate the loss in radius to be $\sqrt{0.55} = 0.74$. Given this, it is shown that the reef tubes decrease in length and radius at the same rate during this simulated weathering of the tubes. This indicates very similar resistance to weathering both along the tube as in the radial direction. However, as this is based on averages and estimates. The durability of these tubes and reef blocks could be an interesting subject for further study, as the mechanism through which tubes lose grains and the role of the different linings in this process is not clear from these results.

On average and in a relative sense, tubes weather equally from all directions. However, this ignores the important aspect of tube breakage. Since the tubes tested are longer than they are wide, they are much more likely to break in that direction. This means that when tubes are individually assessed, long tubes will probably break into smaller pieces instead of shrinking. The second aspect means that given their starting dimensions, the tubes lose much more length than radius. This means that the tubes have more strength in their radius than in their length. This is a result of their structure. Radially, tubes form cohesive layers of grains bonded together. Tubes are flat on their outside, distributing the loads between grains. This also explains why remaining tubes often show a full annulus of grains. Once this support is broken, stress can be concentrated in parts and tubes easily break under these larger loads.

Suitability of Method

The slake durability method initially was aimed at simulating the stresses experienced under wave loading. However, as discussed previously, this is inaccurate and a better representation is the weathering and abrasion experienced by particles as they are dragged along the sea floor by waves and currents. In this environment, single tubes do not survive long. Indeed, no observations of tube (parts) washing up on shores have been recorded. As such, apparatus like the EFA apparatus designed by Briaud and Chen (2005) are more suitable to investigate the behaviour of the material

in water flows.

4.2 Oedometer testing

Results

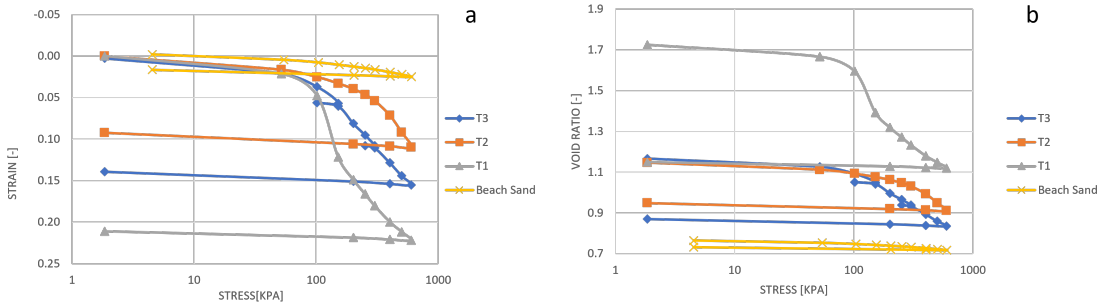

Figure 4.2.1: Stress/Strain (a) and stress/void ratio (b) plot for the oedometer tests performed on reef samples and reference beach sand.

The oedometer test is generally used to examine the compressibility of soils under load while preventing lateral strains. However, in this case the consolidation behaviour is not of interest. This is because the high permeability of the reefs does not allow for a delayed volumetric response. This is reflected by the time interval for each load step which is only 15 minutes. The following relevant parameters have been calculated for each sample and for each load step to help interpret the tests and to classify and describe the behaviour of the samples.

- Coefficient of volume compressibility (m_v): Ratio of unit volume change per unit of effective stress change.
- Compression modulus (E_s): The ratio of mechanical stress to strain in a material when that material is being compressed.
- Compression index (C_c): The change in void ratio for one log cycle of pressure change during compression.
- Swelling index (C_s): The change in void ratio for one log cycle of pressure change during relaxation.

In this set of experiments, three different S. Alveolata reef samples were cut out of reef blocks so that their tubes were roughly parallel to the direction of compression. Aside from this a beach sand sample was prepared from sand collected at the beach near the Océarium at Le Croisic. This sand is a pebbly coarse sand, with many angular fragments and shell pieces present. A picture of this beach sand as used in the shear box experiments can be found in figure 4.3.3. A sample was constructed from this beach sand by placing the ring mold on the base plate and filling it layer-by-layer while compacting the layers in between and at the end. This sample was tested in the same way as the reef samples.

The stress/strain and stress/void ratio plots for the oedometer experiments can be seen in figure 4.2.1. In terms of total strain there is a large difference between the tested beach sand and the reef blocks. The strain in the reef blocks is much larger, with strains between 10-20% for the different samples after loading to 604 kPa. Also, the void ratio change during initial loading of the reef blocks is at least double that of the beach sand, as indicated by the C_c during the first load step. This difference only gets bigger as the average C_c values for the last 3 load intervals in compression are a magnitude higher for the reef blocks compared to the beach sand (table 4.2.1).

Also notable is the large difference in void ratios between the reef blocks and the beach sand (figure 4.2.1b). The range of void ratios of the S. Alveolata samples ranges from 1.15-1.72. This is far higher than the beach sand tested which had a starting void ratio of 0.76. It also has a much wider range of possible void ratios than the sand which ranged from 0.71-0.98 (including the values from later shear box tests). For the construction methods of these samples, see section 4.3, appendix E and previous paragraphs. These high void ratios correspond to low dry densities as well, with the reef blocks having dry densities of 1.23-0.980 g/cm^3 compared to the 1.35-1.56 g/cm^3 for the beach sand (table E.2.1). It is clear that the high strains in the reef blocks are linked to the high void

	Initial			Average last 3 load steps in compression				
	Mv (1/Pa)	**Es (kPa)**	**Cc (-)**	**Mv (1/Pa)**	**Es (kPa)**	**Cc (-)**	**Rebound Cs average**	**Elastic ratio**
Test 1	4.29E-07	2.33E+03	0.040	1.73E-07	6.18E+03	0.374	0.016	0.05
Test 2	3.25E-07	3.07E+03	0.024	2.02E-07	4.98E+03	0.417	0.016	0.16
Test 3	3.73E-07	2.68E+03	0.028	1.69E-07	6.12E+03	0.322	0.017	0.10
Beach Sand	1.30E-07	7.70E+03	0.011	2.99E-08	3.35E+04	0.053	0.007	0.34

Table 4.2.1: Values of the different parameters derived from the oedometer tests in the initial loading step (pre-yielding) and the average of the 3 last loading steps (post-yielding). Also given are the average C_s in rebound and the elastic ratio.

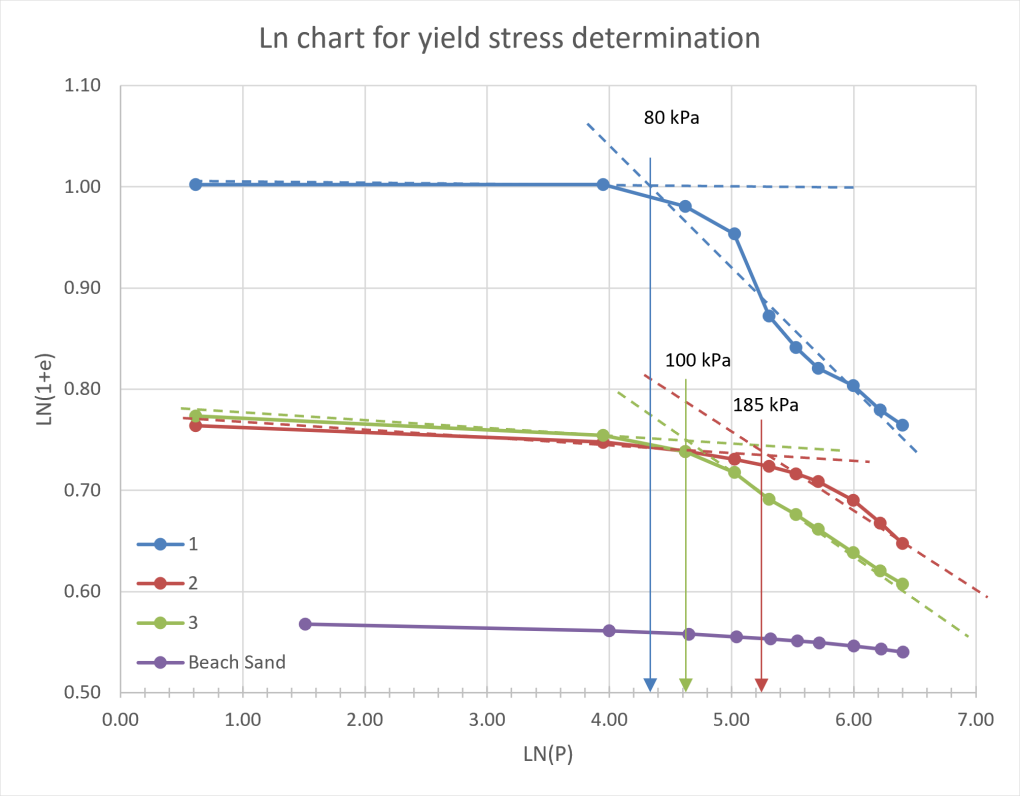

Figure 4.2.2: Butterfield yield stress plot for the different reef block samples and the reference beach sand. The beach sand does not show a yield point, the reef blocks in contrast show a clearly defined yield point in the range of 80-180 kPa.

ratio and low density. The higher the void ratio, the more voids can be closed. This is visible in particular in sample T1, which has the highest void ratio and lowest density from all the samples tested.

Plotting the result on a ln(1+e)-ln(σ) allows the determination of the yield stress according to the Butterfield method (Butterfield, 1979) (figure 4.2.2). The reef samples show clear yield points of 80, 100 and 185 kPa. This in contrast with the beach sand which is more linear over the tested range of stresses. In this case, the yield point is the stress state at which the internal structure of the reefs starts to collapse and the elastic strains make place for mostly plastic behaviour. After this yield point, the void ratio changes much faster than before it, with C_c values about 10-20 times higher than before the yield point(table 4.2.1).

During unloading, 5-16% of the total strain from compression is recovered for the reef blocks. For the beach sand, this is much larger at 34% the total strain (table 4.2.1).

There is a difference between the reef samples. Sample 1 has much higher starting void ratio at 1.72 than the other samples 2 and 3 which have void ratios of 1.15 and 1.17 respectively. As a result, it has a far larger void space that is closed by applying a load, reflected by a much higher total strain (figure 4.2.1). The samples with such a large void space have a higher concentration of tubes than samples with a lower void ratio, as the tube space is a large contributor to the void

space. Sample 1 also stands out because the void space is closed very quickly with the load increase from 100 to 150 kPa. After this interval behaviour becomes more like the other reef samples with C_c becoming more similar to the other samples, in the last three loading intervals they are in fact very similar in terms of C_c (table 4.2.1).

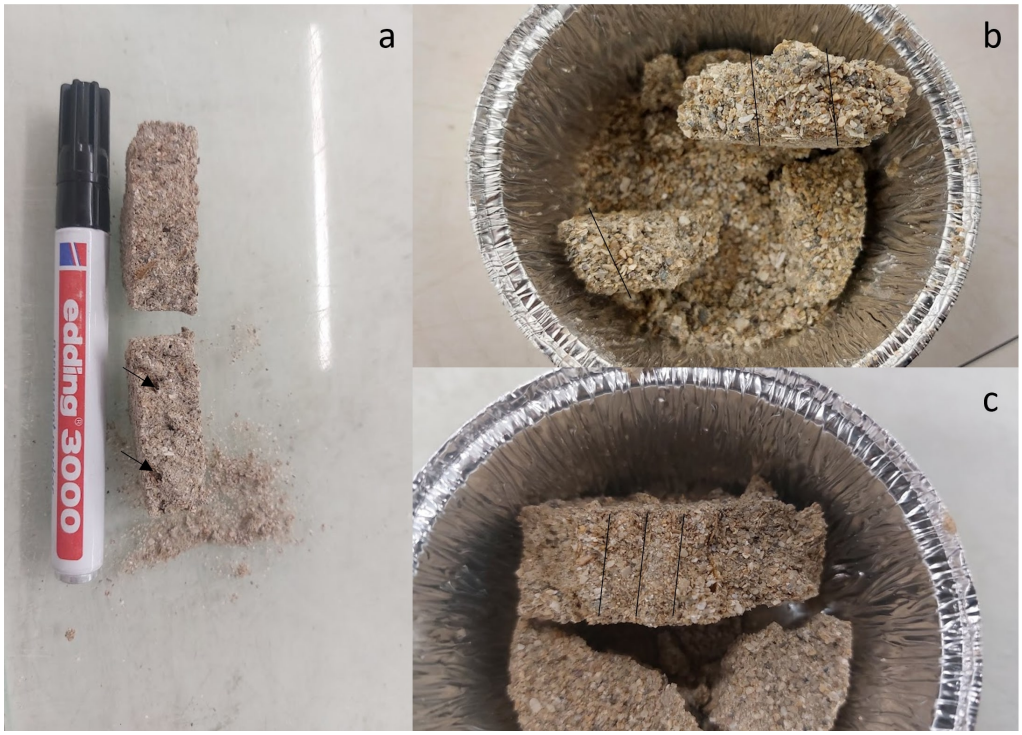

Figure 4.2.3: Photos of the oedometer samples after testing. The black arrows show tube openings, black lines show residual structure in the samples. Photo a: sample 2, b: sample 1, c: sample 3.

The reef blocks behave strongly plastic after exceeding their yield stress and their internal structure starts to collapse. After the experiment the samples were examined. The tubes inside the sample have started to close, meaning that they have decreased in diameter and circumference (figure 4.2.3). However, not all tubes have closed a similar amount, some are still mostly open while other samples show mostly closed tubes. At the same time, the remaining structure from the now (partly) closed tubes is clearly visible in the samples.

Interpretation & Discussion

Given the results from mCT-scanning, which showed that the tubes represent a large percentage of void space, it is likely that the lower density and high void ratio encountered are a result of a higher tube concentration. At the large difference between samples in terms of void ratio and density shows the large natural variability in the reefs.

It is known that at a small scale the tubes themselves behave visco-elastic, meaning that they can dissipate energy in their movement, and that the strains are reversible at strains up to 0.6 mm, although not instantaneous in time (Le Cam et al., 2011). Although the Butterfield yield stresses point to a clear boundary between elastic and plastic behaviour, this cannot be fully ascertained. No unloading was performed below the yield points as calculated. For sample 3, unloading was performed from 150 to 100 kPa and from 300 to 250 kPa. These unloading steps result in very similar rebound behaviour, with C_s values of 0.006 and 0.009. This is very similar to the rebound values of the beach sand. The final rebound of the reefs is slightly stronger, with C_s values of about 0.016 during final unloading. These final rebound values are in between the C_s of the beach sand and the C_c of the reef samples during initial loading. This means that to some extent, the mechanisms differ.

In the initial stages of loading, bonds between grains are intact leading to stiffer behaviour. After the yield point, the bonds start breaking and samples start behaving less stiff. However, when reef samples are unloaded and in rebound, their stiffness is very much in between that of the initial response of the reef samples and the final rebound stiffness of the beach sand. This probably means

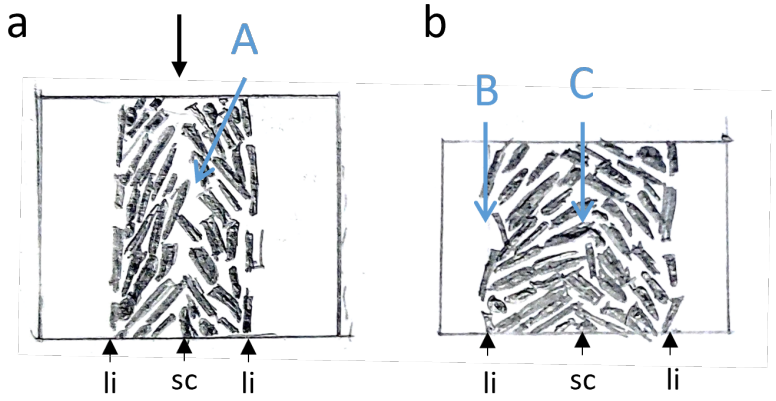

Figure 4.2.4: Sketch of the behaviour of the reef samples under oedometric conditions . a) is the situation before the load (black arrow) is applied and b) is the situation afterwards. The sketches are based on figure 3.3.3b. Note the void space between tubes can sometimes be large (A). With pressure, these areas (B) as well as the tube space is closed, displacing the inner lining (li) (C). Grains are able to slide over each other to the inside of the tube space due to the angle of the grains in the scale-like outer layer (sc). The destructuration of the sample probably only occurs after the yield point, with void space reducing without destructuration before the yield point as a result of compressing bonds.

that not all bonds in the samples are completely broken.

Given the (apparent) cohesion remaining in the samples and the rebound behaviour, it is likely that the bonds in the samples are not fully broken during compression. With the stresses encountered in the samples, no particle breakage is expected either, and indeed, none was observed with the naked eye. This does not mean no particle breakage occured but does indicate that it did not happen at large scale. This means that the total strain of about 22% is a result of rearrangement of grains and accompanying deformation of glue spots. It was observed that the inner diameter of the tubes decreased during testing. This is possible as a result of compression along the tube axis, which would compress the grain layers, causing destructuration and dilation of the grain linings and as such decreasing the inner tube diameter and closing voids between tubes. This is aided by the inwards orientation of the outer grain layer. At the same time, any space present between tubes would probably also be closed. When looking at figure 3.2.1, it is easy to see how this is possible. Even within the structure, enough room is available grains to adjust their position. This mechanism is illustrated in figure 4.2.4. Given this mechanism, it is likely that the apparent cohesion in the samples after testing is a function of interlocking and cohesion.

At large stresses, it is clear that their C_c values become similar (table 4.2.1) although the corresponding void ratios still vary significantly. This could be because there is a degree of natural variability in the distribution of void space in the samples, which is closed when pressure is applied after which the behaviour of the samples becomes more uniform. It is not possible to say if or when samples start to behave like the beach sand. If this were to ever happen, significantly more pressure would be needed than was exerted in these experiments.

Notably, sample 1 shows a very high void ratio and high compressibility. Several explanations for this are possible. Most likely, it can be attributed to damage or destructuration during samples preparation and placement, or from flaws in the testing as mentioned for the shear box testing. However, there is no direct reason to think this is the case as no other abnormal behaviour was observed. As such it may be a result of the natural variability in the reefs.

The beach sand tested here shows behaviour in line with other carbonate sands. For example, it does not show a yield point at the stresses tested here. This is in line with other carbonate sands, such as those tested by Nakata et al. (2001) and Yang et al. (2021). When comparing its behaviour to the different ratios of carbonate/silicate sands tested by Yang et al. (2021), its behaviour is in line with 60-100% carbonate sands in terms of C_c values although courser grained than those sands which have a diameter of 0.5-0.8 mm.

A comparison can also be made between the reefs and some other materials. For example, Head and Epps (2011) lists some values for m_v, and describes the maximum values found here as high

to very high, on the same level as alluvial clays and peats. Compared to Australian cemented calcareous sands, which have a C_c value of 0.18-0.24 and a C_s value of 0.065 (Chai et al., 2021), which are less than what was found here. And as such, the compressibility of the reef material is higher than most materials.

As described before, a man wearing rubber boots will exert a pressure of about 150 kPa onto the reefs while standing (Vorberg, 2000). When assessing the dynamic pressures generated in walking, Hessert et al. (2005) found that some parts of the foot can generate up to 4.5% of body weight/cm^2. For an adult weighing 80 kg, this translates to 350 kPa exerted on the reefs for a short time. However, most parts of the foot do not exert more than 3.5% of body weight/cm^2 or 275 kPa for an 80 kg adult. Grieve and Rashdi (1984) cited pressures of about 210 kPa while walking. However, these pressures are dynamic they only occur during very short times (25 msec) (Rodgers, 1995).

Given the loading method here, the static pressures can be compared to the results. Given the yield stresses of these samples are in the range of 80-180 kPa, it is doubtful whether someone standing on the reefs does permanent damage. The damage would be dependend on body weight but also on the strength of the reef in that place, as it is naturally variable. As for the damage caused by walking, this is more difficult to assess as the testing method is static loading. However, given the very short loading duration at such pressures, lasting damage is unlikely. Especially given the high mobility of the worms in their tubes and their ability to repair reefs. Damage caused by impacts from fishing gear are known to be repaired in three days (Vorberg, 2000). This has also been observed under laboratory conditions, with worms reconstructing 10 mm/day during the first two days (Vovelle, 1965) or up to 25 mm in two weeks (Gruet & Bodeur, 1994). Note that the existence of a full tube annulus is necessary for reconstruction (Vovelle, 1965).

Figure 4.2.5: Photo taken during fieldwork in location 5.3 showing S. Alveolata reefs overgrowing manmade groynes built for coastal protection.

Besides the pressures from people walking, the reefs will also experience loads from waves. These loads are highly dependent on local conditions, with many factors such as tides and coastal morphology influencing the formation of waves (D' Angremond & Pluim-van der Velden, 2001), as such this topic is not further explored here. However, an estimation can be made using the method developed by Cuomo et al. (2010) for estimating the wave load on a near-vertical wall. This is a close analogue for the S. Alveolata reefs, which are sometimes even found on such structures (figure 4.2.5). At the location of figure 4.2.5 waves of about 1.8 m high were not uncommon ("Ile de Noirmoutier - Barbatre Surf Forecast and Surf Report", n.d.). Using this information, an estimated 36

kPa can be calculated as the pressure exerted by waves. This is well below any of the yield point and explains why these reefs are able to withstand such storms. However, the interaction of waves and these reefs is a complex mechanism which requires much more detailed investigation to give accurate assessment.

Suitability of Method

Oedometer testing of the reefs is a method well suited to showing its behaviour under 1D compression. These results showed the behaviour of the reefs under common pressures such as walking. The 1D compression method of testing does have its shortcomings though. This method with these pressures did not succeed in showing the full extent of behaviour, as the elasticity of the materials before the yield point was not examined. However, the method did succeed at illustrating the compressibility of the material. Unfortunately, the lateral pressures could not be examined using this method, which would help determine how stresses are distributed and dissipated inside the reefs. Further testing repeat loading above and below the yield point would be recommended to further study the behaviour of the material under conditions more reflective of in-situ pressures. These tests would be especially useful combined with further imaging showing how damage occurs in the reefs. This is possible using special apparatus which work inside the mCT-scanner.

4.3 Shear Box testing

Results

To investigate the behaviour of the reef materials under shear conditions, direct shear testing was done on three samples of the reefs collected from location 6.1C as well as on beach sand collected from the beach at Le Croisic. This sand is a pebbly coarse sand, with many angular fragments and shell pieces present. A picture of these sands before and after shearing in the shear box is present in figure 4.3.3. A stepped approach was taken where the samples were sheared to constant shear stress at different normal stresses consecutively. This is to investigate the behaviour also after the yield stress has been exceeded. This is done to investigate the behaviour of the material in a degraded state, which is a relevant factor as reefs degrade and grow over time.

Firstly, the vertical displacements and shear stresses are given as a function of horizontal displacement in figure 4.3.1. This shows the difference in volumetric behaviour during testing, with the beach sands showing varying amounts of dilation followed by compression in later stages. For example, beach sand 2 dilates in load steps 1, 2 and 3 with constant volume shearing in the last step. This contrasts with, for example, reef sample 2, which starts compressing as testing starts showing only some dilation in the first load step. During this first load step, reef samples are sheared up to 3.5 mm horizontal displacement. For beach sand, their volumetric behaviour is related to their initial void ratios (table 4.3.1) with the looser samples (high void ratio) having a tendency towards compression while denser samples (low void ratio) show strong dilation. The reefs all compress during shearing.

In terms of shear force, a similar pattern is visible. The dense sand samples (lower void ratio) show higher peak strengths than the loose sands (higher void ratio). For the reefs, samples 1 and 2 show similar peak strengths with similar void ratios. Sample 3 is very different to the others. It only shows a peak strength during the load step. After this, the shear force drops off, even with increased normal stresses.

Looking at the void ratio development over the test (figure 4.3.1c), the void ratios of several samples reef and beach sand samples become very similar after testing with a value of about 0.85. The reef samples compress until they reach this value, although they would probably keep compressing with increased shear displacement as they do not show any asymptotic behaviour. Conversely, the beach sands show a decreasing shear stress at these points, except for beach sand 1 which show an increasing stress at the end stages of shearing.

From these results, the normal stresses versus the peak shear stress are plotted. This results in a linear increase of shear strength with normal stress for the reefs, while the sands show a curve. For the beach sands, the increase of shear strength is not linear but decreases at high normal loads (figure 4.3.2). A Mohr-Coulomb failure criteria is fitted to these results. Every sample has been fitted individually (figures E.3.3 and E.3.4) as well as all together. Using all data points gives a friction angle of 21.3°and a cohesion of 23.1 kPa for the S. A. reefs. However, the individual samples show a spread with cohesion varying from 22.3-32.7 kPa and friction angles from 12.8-22.3°. Figure

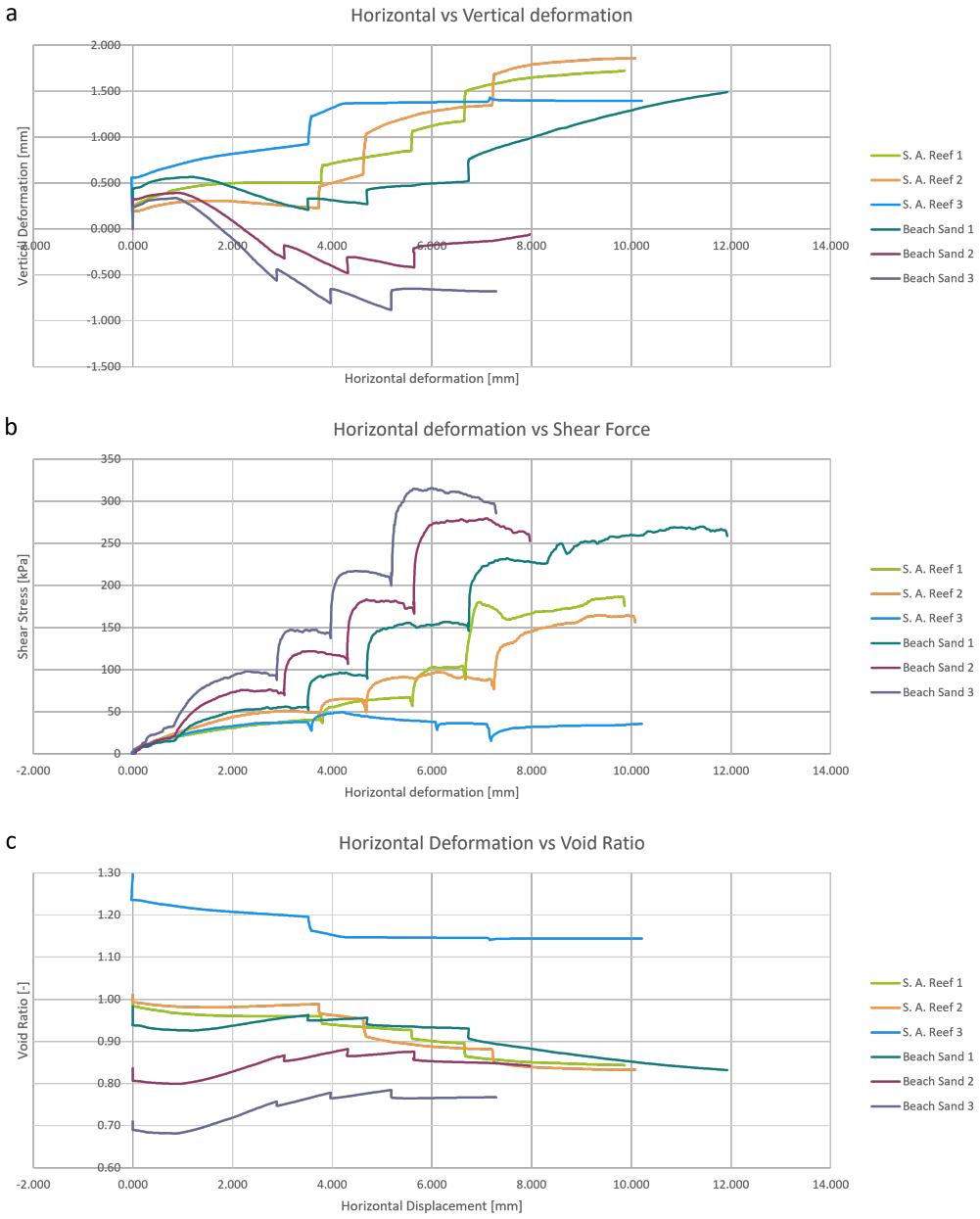

Figure 4.3.1: Vertical displacement (a), shear stress (b) and (c) void ratio against horizontal deformation for the different samples tested. Note that positive vertical deformation means compression here.

	c' [kPa]	phi' [°]	Tested Density [g/cm3]	Dry Density [g/cm3]	Moisture content after test [%]	Void ratio
S. A. Reef 1	22.3	22.3	1.61	1.33	21%	1.01
S. A. Reef 2	32.7	19.0	1.58	1.33	19%	1.01
S. A. Reef 3	26.5	12.8	1.49	1.16	28%	1.30
Combined	23.1	21.3				
	phi' [°] - 1mm	phi' [°] - Stage 3	Tested Density [g/cm3]	Dry Density [g/cm3]	Moisture content after test [%]	Void ratio
Beach sand 1	18.1	30.9	1.35	1.35	0.29%	0.98
Beach sand 2	23.7	34.5	1.45	1.45	0.27%	0.83
Beach sand 3	34.4	37.6	1.57	1.56	0.31%	0.71

Table 4.3.1: Determined parameters as based on shear box tests for the different samples.

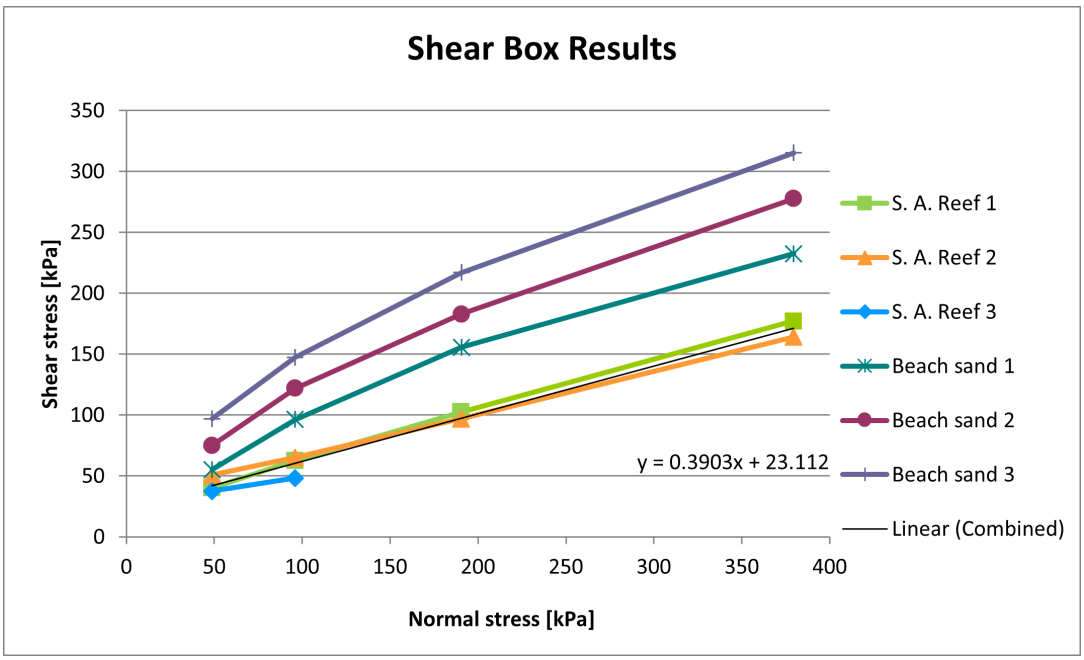

Figure 4.3.2: Normal vs. peak shear stresses during the shear box experiments for all the different samples tested.

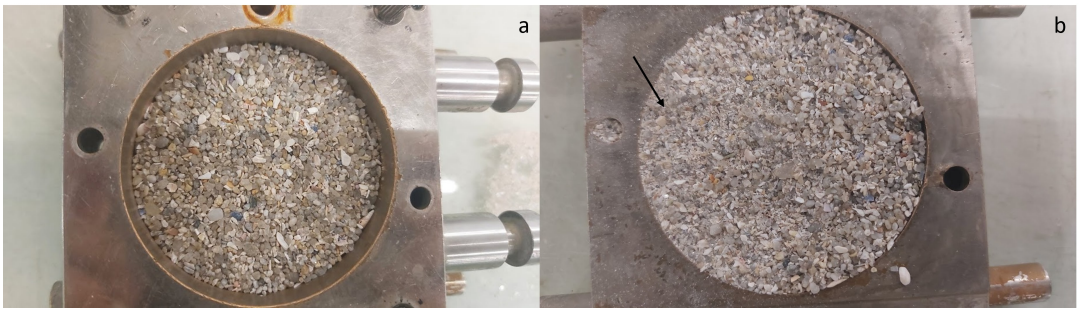

Figure 4.3.3: Photos from beach sand sample 3 before (a) and after (b) testing. A large amount of coarse grains and larger fragments is visible. Note the smaller grain size as indicated by the black arrow in (b). For scale, the diameter of the shear box is 63 mm.

4.3.2 shows though that the lines for the reef samples curve slightly at the start. This means that the cohesion is probably higher than estimated here and could be as high as about 40 kPa. At the lower confining stresses the influence of friction angles is lower while the cohesive bonds are fully intact, leading to underestimation of the cohesion using the stepped approach.

The beach sands are also fitted with a Mohr-Coulomb criteria (figure E.3.4). The friction angle of the sands can be computed based on all values or on the first values from figure 4.3.2, but this gives friction angles in the order of 46-60°, which is unrealistically high for sands. Looking at the displacements (figure 4.3.1), the beach sands show strong dilation beginning at a horizontal displacement of about 1 mm which is accompanied by a strong increase in shear stresses. The mobilization of this dilative behaviour distorts the friction angle. This will be discussed further in the methods subsection. As such, the friction angle has been calculated from the point where the shear stresses initially start to deflect upwards. This gives friction angles of 18-34° (table 4.3.1). With comparative void ratios, these angles are similar or slightly lower than the friction angles of the reef samples. For comparison sake, the friction angles have also been computed for the end of the experiment, where the samples show constant void ratio. For this, the shear stresses just before stopping the experiment have been used. This gives friction angles of 31-38° (table 4.3.1).

The beach sand samples all show some degree of dilation during the experiments (figures 4.3.1). The amount of dilation is related to the initial void ratio, like the friction angle is. Samples with smaller void ratios show more dilation and a higher friction angle, as grains that are more closely packed are harder to move from each other. However, the friction angle of the sand decreases

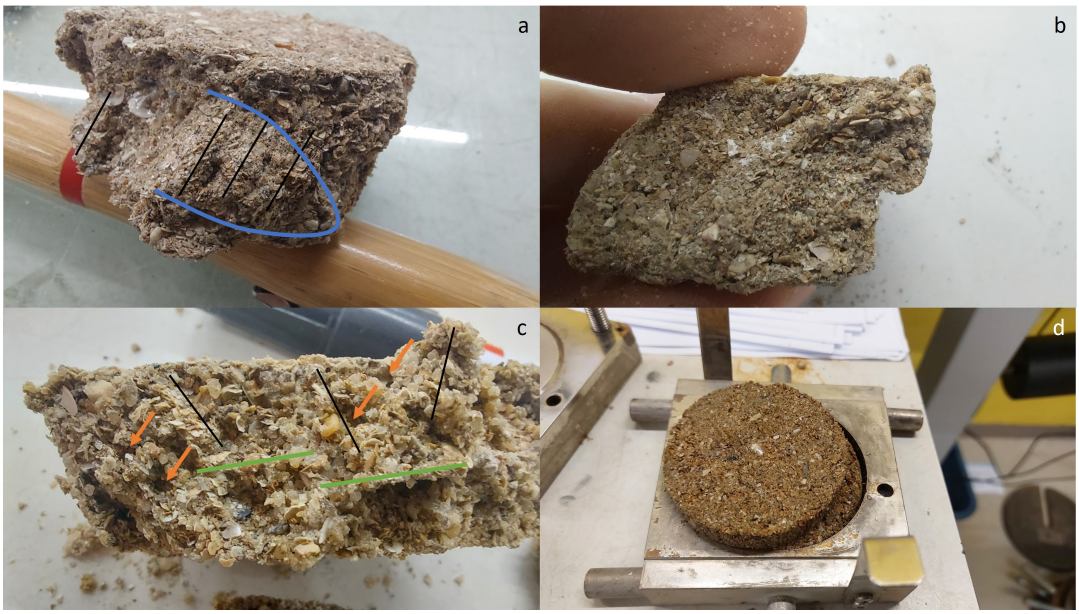

Figure 4.3.4: Photos from the tested reef samples after testing. Photos are from sample 1. Photos a and b were taken perpendicular to the shear direction, photo c was taken parallel to the shear direction. The black lines denote visible tubes remaining in the samples, the structure indicated by the blue lines is a possible the shear band formed during shearing. The green lines indicate a possible shear plane. As visible in sample a, some tubes do remain visible inside the formed band indicated in blue. At the same time sample b indicates that this is not always the case, although it is not possible to ascertain the amount of tubes present in the sample before shearing. Photo c shows a structure in which plenty of tubular structure remains, broken by a possible shear plane in some places. Also note the multiple crevasses between residual tubular structures as indicated by the orange arrows.

over the experiment. This is probably because of particle breakage. This is also visible inside the samples when disassembling as visible when comparing figure 4.3.3a and b. After shearing, a band is visible inside the sample in which many finer grained particles are visible along with dust and other fines from particles breaking. This is not seen inside the reef samples which do not show any particle breakage and keep a constant friction angle even at high stresses and large displacements.

After shearing, samples were dissected to investigate their structure. Between samples, there are some differences. In all reef samples, some of the tubes remain open, while others are fully or partly closed and squished. Tubes are often bent and/or broken, while others remain more or less intact. Generally, a large portion of the internal structure is damaged and sometimes a band or plane is visible, probably formed by shearing. In sample 2, voids have opened up (figure 4.3.4c), while in samples 1 and 3 they have closed and most internal structure is destroyed (figure 4.3.4a/b). This is however strongly dependent on which direction the sample is viewed in and in which direction it is cut. Interestingly, a band can be seen in sample 1 inside of which structure does remain. Inside this band, looking along the direction of shearing, very little structure is visible. This is because tubes have been bent and flattened and as such, no structure is visible any more. However, looking perpendicular to the shear direction the tubes are often bent (figure 4.3.4b) or deformed (figure 4.3.4a) with the direction of shearing but the remnants are still visible. The sample outside of this shear band seems to be broken or displaced relative to the shear band with no continuity visible. However, in samples 2 and 3 this band is not clearly defined and instead a discontinuous plane can be seen inside the samples.

As the sample in figure 4.3.4d shows, although the internal structure may be deformed to such a degree that it becomes completely unrecognizable, the sample does keep its structural integrity. It still stands up straight, retains enough (apparent) cohesion to act as a single block and the top and bottom surfaces are still parallel. This in contrast to the beach sand which has none of these characteristics.

Interpretation & Discussion

Looking in more detail at the results for sample 3 (figure 4.3.2), only the first two data points are plotted. When looking at the full data for the reef samples in figure E.3.3, it becomes clear that for this sample, behaviour is very different from the other samples. Where reef samples 1 and 2 behave strongly linear with both a cohesive and frictional component of strength, sample 3 is different. For that sample, peak shear strength is found during the second loading interval, without much increase from the first. Given the erratic behaviour of this sample it is more likely that the shear box did not work as designed. The normal forces are transferred to the sample by a top cap which is loosely placed on the sample. It is possible for this top cap to get stuck, this is the case for this sample, given the lack of response to increased normal stress on the sample. Also, it was noted that the shear box was much harder to disassemble after testing this sample compared to others. This can be seen at a displacement of about 7.0 mm (figure 4.3.1a). Because of this, this part of the behaviour is not considered during calculation of friction angles and cohesion.

Similarly, beach sand sample 1 also shows some erratic behaviour. Although shear forces decrease after reaching a peak in the last stage of shearing, at a displacement of about 8.5 mm they start increasing again. This is erratic behaviour, often caused by load being taken by larger particles such as shell fragments or stones. Large particles are present in the beach sands, as shown in figure 4.3.3. As such, this load increase is not taken into account for the estimation of friction angles of the sand.

It is also notable that reef samples 1 and 2 and beach sands 1 and 2 reach similar void ratios during the later stages of experimentation. However, their behaviour is different, with the reef samples showing lower shear stresses and compaction while the volume of the beach sands does not change anymore. The strain in the reef samples is also significantly higher than that of the beach sands. This means that the structures differ strongly between the two types of samples. More specifically, the reef samples keep (part of) their cohesion but show a lower friction angle. This is not surprising, the structure of the reefs aligns the flat grains of sand, reducing interlocking. At full displacement, the reefs keep compacting and would probably compact further with more displacement. The reefs start as a very loosely packed material but can become very densely packed. This is possible because grains in the tubes are normally neatly arranged making the tube walls relatively densely packed. When the tube space is closed during shearing, a material is formed which is more dense than normal sands. The way grains are arranged next to each other probably also lowers the friction between grains, allowing for high levels of compaction.

Given this, the friction angle of the beach sand should be discussed. It should firstly be noted that several friction angles are commonly used to describe the shear behaviour of sands. Chief among these are the peak friction angle ϕ_p and the constant volume friction angle ϕ_{cv}. The peak friction angle describes the behaviour of the sand including the component induced by dilation, while the constant volume friction angle is a parameter describing steady state behaviour (Jamiolkowski et al., 2003). Given the curved envelope in figure 4.3.2, the peak friction angle of the beach sand tested here is related to the stress state. At these peak states, their behaviour can be described using a Mohr-Coulomb criteria by using an apparent cohesion and peak friction angle which vary with the stress state. With increasing stress state, the apparent cohesion increases while peak friction angle decreases.

However, the reefs are best described using a constant friction angle, and as such must be compared to the constant volume friction angle of the beach sands tested, as it does not change with stress. As mentioned, these can be computed in two ways, with one computed from the infliction point marking the onset of dilation and one from the constant void ratio shearing condition produced at the end of the experiment. As such, it needs discussing which friction angles are closer to reality. The measurements taken at the infliction point give friction angles ranging from 18-34°. At this point, particles have been compacted by a 49 kPa normal stress and have compacted under shear (as the dilation has not yet been mobilized). Although the volume is constant at that point while the samples go from compaction to dilation, this is temporary and the arrangement of particles will be different than in the constant volume state at the end of testing as the particles are rearranged during shearing.

As such, the constant void ratio friction angles are probably more accurate. Their values are also closer to what would be expected for angular sands such as those tested by Prakash et al. (2023) and closer to those of the calcareous sands tested by Jamiolkowski et al. (2003). However, they are probably still overestimated given that the forces were still decreasing at the time experimentation was stopped. Given this, the shear resistance of the beach sand is higher than that of the reefs. This

is probably due to the structure in the reefs, where grain contacts are not randomly distributed (as they are in the beach sand) and (most of) the grain contacts are connected by the glue. Also, it has been observed that the tubes are interlocking to some extent. As such, the friction angle measured in the reef sands is a function of both intertube and intergrain friction, complicated by the deformation of tubes under compression and shear loading.

Inside the beach sand samples, breakage of grains has been observed. This is normally not the case with sands until their compaction ability is exhausted (Ghafghazi et al., 2014) and as such is unexpected in the dilating sands tested here. It is likely that this is because some of the fragments in the beach sand are porous in nature. Also, the angular shape of carbonate sand particles facilitates bending fracture, and particles with a lower sphericity and a higher porosity are more prone to breaking (Li et al., 2020).

Looking at more detail at the structural changes, during shearing, the tubes are not only bent and closed by the shear forces, the structure can become deformed to where it is barely recognizable. However, the tubes do retain some structural integrity even though they experience not only shear but also tensile forces as the experiment goes on and they are deformed along the shear direction.

Lastly, it is necessary to discuss the structural damage observed in the samples. These include bent tubes and a band formed after testing (figure 4.3.1). Probably, in the first stages of shearing, tubes are bent along the shear direction with increasing displacement. As the stress directions rotate with increased displacement, tubes are also closed. In the last stages of shearing, the shear bands or planes are formed, probably as a result of the samples staying attached to the shear box walls under the confining pressure. At this point, the larger voids seen in some samples probably also open up, breaking between tube remains. As such, most of the load will be concentrated in the centre of the samples, where the tubes are fully bent and folded in response to the stresses. Although this is the most likely mechanism, it is theoretically possible that (parts of) the band/plane were formed in-situ or as a result of sampling. However, in the parts of the reefs studied for their structure, no similar-looking phenomena have been observed making its natural formation unlikely. As such, it is recommended to combine shearing with mCT scanning before and during testing to more fully understand their behaviour.

Given the mechanisms described above, the apparent cohesion shown by the samples after testing is probably a function of several mechanisms. It is clear that initially, grains are bonded together by a real cohesion due to the S. A. glue. After testing, reef samples are deformed with displacements up to 1 cm or 16% of their diameter. With these displacements, fully intact glue bonding in the samples is unlikely and the rebound stiffness in 1D compression indicates this also. As such, several possible causes of this apparent cohesion exist. As discussed in section 4.4.3, it often requires very high stresses and strains to granulate a cemented sand (Coop & Atkinson, 1993; Lade & Trads, 2014). The results show this, with (parts of) tubes found mostly intact after testing. At the same time, parts of the samples were found with extensive damage in the form of bent, broken and flattened tubes. As such, damage varies inside the sample. Given these observation, the observed apparent cohesion is probably the result of interlocking tube parts, with some bonds intact in places without much damage. These tube parts are more or less intact, with both contributions from (damaged) glue spots as well as increased particle interlocking due to decrease in void ratios. It may be that a significant part of the displacement is along shear bands and planes, allowing some of the glue spots to stay intact. However, samples did not split along these structures when dissecting samples, pointing to strong interlocking of these structures.

It is difficult to compare these stresses and effects with the loads put on the reefs in-situ. These include, for example, wave loading and loading of walking and fishing. These effects do generally not directly induce shear stresses on sample in the same way the test does. As such, the comparisons made here are not fully accurate. In terms of bed shear stress (stresses exerted on a surface by water flowing over it), Thappeta et al. (2023) for example estimates peaks of 630 Pa under wave flume conditions when rapidly increasing water depth from 10 to 40 cm. This may be similar to the stress increases induced by waves. Although these bed stresses are not directly simulated by the shear box, they give an idea of the magnitudes of such stresses. These are much lower than even the cohesion of the reefs, showing how they can stand up in such water flows. When using the method mentioned before (Cuomo et al., 2010), wave pressures in the order of 36 kPa can be expected, which exceed the cohesion of the reefs. However, there is also the influence of the friction angles of the reefs and the effect of the direction of stresses. Together with the complex morphologies of the reefs, this makes a complex puzzle which would make a good research topic for further study.

Suitability of Method

Samples for testing in this case were made out of samples taken from sampling tube, removing a small annulus of damaged material in the process. Although these samples were visually intact, they may have sustained damage during sampling, distorting their behaviour. Small cracks and other damages are not visible with the naked eye and may not become apparent during handling of the samples. Even in mCT scanning this would probably not be visible, although this needs testing to ascertain. As such, there is a chance samples may not have been representative.

The stepped approach taken made for the requirement of a stopping criterium to add an extra load. In this case, the criteria was a constant shear load. However, this is problematic when working with beach sand, which exhibits strong volume changing behaviour due to the angular nature of the fragments. This behaviour persists over large displacements. As such, even though shear stresses became approximately constant when shearing was stopped, this would have been temporary and shear load and dilation would probably have decreased with further displacement. The beginning of this is already visible in figure 4.3.1, with forces decreasing after a peak in most cases. This is also what would have given representative friction angles, with the current calculated friction angles being only an approximation. Basically, the test was probably stopped too early leading to initial overestimation of the friction angles to an unrealistic degree. For further testing, shearing should be stopped at a larger displacement. If more material is available in the correct sizes, unstepped shearing for different samples at different confining pressures would be able to show more of the failure mechanisms at different confining stresses.

More importantly, the stepped shearing has the important disadvantage that the strength at the later stress levels is affected by the shear failure occurring during earlier shear steps. In this case it means that after the first step the strength of the material is no longer fully reflective of the intact material, but is more reflective of damaged material. However, since the reefs naturally exist in many different stages of deterioration and progradation, the data is probably still relevant to reefs at different locations and to reefs in different health conditions.

At the same time, although the tests did showcase some of the material properties of the reef, they were difficult to relate to in-situ conditions and threats. This is partly due to the limited applicability of the chosen method to the in-situ loads. Also, the tests did not allow to ascertain the manner of deformations of the material. As such, a better investigation into the shear strength of these materials may be triaxial testing inside an mCT scanner. Also, testing which is more applied to the actual conditions or use case of the material is recommended. As mentioned in previous sections, there are several possibilities for this such as flume testing.

4.4 Data synthesis, discussion and comparison with other cemented sands

This section is dedicated to synthesizing the data from the different experiments and comparing this to the other cemented sands. Some other test-related issues will be discussed and previously presented results will be looked at critically here.

4.4.1 Influence of storage

Firstly, the influence of the time delay between collecting samples and testing must be discussed. In total, about one year was between the sample collection and last tests performed for this thesis. It has been observed earlier that the vacuum drying as inherent to E-SEM damages the inner membrane and glue spots (section 3). However, when Le Cam et al. (2011) tested 5 year old samples which had been stored in dry conditions, it was found that they were still able to dissipate energy. At the same time, it has been observed that samples in storage showed strong black discoloration after a few months of storage in airtight containers, accompanied with a strong odour. These signs point to anoxic degradation of organic matter stored in the sediments, with the black discoloration a product of precipitating iron sulfides and the smell being toxic H_2S (Broman et al., 2017). This process, although well described, is complex with several intermediary steps producing and using several different products which may or may not influence the behaviour of the organic glue studied here (Kirchman, 2012). Generally, the process seems to be completed by several different microbes and produces H_2S and Fe^{2+}, which is reversible when oxygen is reintroduced (Broman et al., 2017; Lovley, 1997). No information is available on the effects of these chemicals on the S. Alveolata glue. Since both the discoloration and smell disappeared with the regular introduction of fresh air

into the storage buckets, this happened to the samples studied here as well. As such, there is no direct reason that suggests significant deterioration by this effect, but it cannot be excluded either. However, given that materials with similar chemical formation mechanisms to the glue (complex coacervates) have long been used to encapsulate volatile or sensitive compounds (Shao et al., 2009), there is reason to believe the results are still at least somewhat representative.

4.4.2 Failure

The failure mechanisms of the tubes must be discussed. As mentioned in the sections before, it is clear that the tubes inside the sample are not completely destroyed during testing. Rather, the tubular structure remains after testing, even though it is bent and broken (figures 4.2.3 & 4.3.4), or in some cases not even visible anymore. This raises the question what failure entails in this case. One of the criteria most at hand is the reduction of the reefs back to the consistency of beach sand. However, this point is not reached during any of the tests done. Another possibility is to define failure as any breakage or loss of cohesion within the sample, but this does not happen fully in any of the tests even though the cohesion is (partly) replaced by an apparent cohesion. As such, defining failure as making the reef uninhabitable for the S. Alveolata is more suitable. However, this means that probably after a single stage of shearing most tubes are uninhabitable as the displacement after a single shearing is already about 3.5 mm. Notable, this is the same for all the different reef samples. Also, this is a good estimate for the diameter of a single tube (figure 3.2.1). So, it can be said that the the shear stresses found for the first loading step are the best approximation in view of the criterion. These stresses are about 38-50 kPa. This is also similar to the stress induced by wave loading, something the reefs are known to survive. As such, this is a good estimate of the stresses possible in the reef before they become uninhabitable.

However, when looking at the behaviour in 1D compression it is more difficult to determine when the reefs become uninhabitable to S. Alveolata individuals. Even after yielding and after the full 304 kPa of vertical pressure, the tubes are not fully closed and as such S. Alveolata individuals may survive such pressures on the reefs.

Whatever the loading the direction may be, it needs to be considered that any stresses and as such any damage will spread under the footing. As such, any damage will be concentrated at the top of the reefs. Considering that worms were seen to move inside their tubes to protect themselves (Vovelle, 1965), they are more likely to survive loading of the reefs. Given that the worms are known to rebuild reefs very quickly after being damaged by fishing gear (Vorberg, 2000), damage is less likely than would be thought purely based on the results from the tests performed in this thesis.

4.4.3 Comparison with other cemented sands

The closest materials in many aspects to these reefs are calcareous (artificially) cemented sands. These sands are often found to have characteristics of both soils and rocks (Sitar, 1983), with many similarities regardless of cementing agent. These materials show similar behaviour regardless of cementing agent in that they can resist shear stress and compression as well as some tensile stress due to cohesion. At the same time for most of these materials, a linear Mohr-Coulomb strength envelope apply. In many of these materials, apparent cohesion is a function of the cementing agent and angularity of the particles. Failure at low confining pressures often occurs at low strain levels, with an increasing ductile response at higher confinement levels (Collins & Sitar, 2009). And in many aspects these criteria apply to reefs as well. For example, as noted before, the Mohr-Coulomb strength envelope of these materials is very much linear. However, failure in the case of these reefs is difficult define. At no point during these experiments did any sample exhibit a brittle failure and breakage such as found by Clough et al. (1981). However, looking at the material in terms of functional failure, it exhibits a progressive collapse of structure after a well-defined yield point.

In terms of behaviour, cemented carbonate sands feature relatively high friction angles and compressibilities. The bonding of these sands results in increased strength and stiffness, which increase with increasing sands contents. At the same time these bonded soils have lower water contents and void ratios than their uncemented counterparts because the void spaces are filled with cement (Coop & Atkinson, 1993). The effect on friction angle differs per soil and cement type with Coop and Atkinson (1993) reporting decreases of about 3°for carbonate sands cemented with gypsum, while Lade and Trads (2014) reports slightly increased friction angles although the increase is dependent on confining pressures. So generally, no significant changes are expected (Allman & Poulos, 1988).

In some aspects, the reef materials as built by S. Alveolata have similar characteristics. Especially in terms of compressibility the reefs are very different to the tested beach sands with their compressibilities much higher than the sands. However, in some aspects, these reefs contradict the norm. As they are built grain-by-grain, glue is only placed at grain contacts and not randomly deposited on grains as is the case for cemented sands. As such, there is no filling of void spaces as is the case with normal cemented sands (Allman & Poulos, 1988; Boey & Carter, 1988). As is shown by the experiments in previous sections, friction angles are very different, probably as a function of this. Even when void ratios are comparable as in the shear box experiments (0.98 to 1.01), the friction angles of the reefs are about 2/3 of those from the tested beach sand. As such, the structure provides for very different ways of movement of the particles among each other. As we have seen in the structural investigation of the reefs, they often consist of flat particles neatly arranged in a scale-like pattern. This would provide very little frictional resistance compared to the normal arrangements in sand grains.

Cemented sands experience strong influence of confining pressures. At low confining pressures a peak strength can be observed from cohesion (Cuccovillo & Coop, 1999). Also, samples show linear behaviour until plastic yielding initiates as the bonds start to degrade, after which strong volumetric dilation takes place. The bonds that cause this cohesion often start to break at very small strains (Cuccovillo & Coop, 1999; Lade & Trads, 2014). At higher confining pressures (1000s of kPa), the soil behaviour becomes ductile and is generally in compression. Under these cirumstances, the effect of cementation is insignificant as behaviour is mostly frictional. Also, the initial void ratio is important with samples at low void ratios experiencing dilation and samples with high void ratios being more compressive (Allman & Poulos, 1988; Coop & Atkinson, 1993; Lade & Trads, 2014). Also, in cemented sands, the soil will not necessarily return to the behaviour of uncemented soil after the bonds are broken. This is due to a small degree of residual cohesion (Clough et al., 1981) and because lumps of cemented materials act as larger particles (Lade & Trads, 2014). The residual strength of these materials is however independent on the degree of cementation (Reddy & Saxena, 1993). However, especially after larger strains soils may return to similar behaviour as the uncemented material. It often requires very high stresses and strains to granulate a cemented sand (Coop & Atkinson, 1993; Lade & Trads, 2014). Given this and the testing regime the reef samples were subjected to, we should have seen breaking of bonds at low strains. This remains difficult to judge, but apart from a very small interval for sample 2, no dilation was seen from the reef samples. This is because of the very large void ratios and specific structure encountered. These provide for very little particle interlocking and as such for little dilation. Also, as discussed before, the internal structure does not fully collapse and close at any point during these experiments, this may be similar to cemented sands but would require a closer examination at the specific testing pressures. Remarkably, the behaviour of the tested reefs could easily be described as ductile, showing strong deformation but no loss of cohesion. This is in contrast to other cemented sands, which only show this effect at very high confining pressures. This is probably due to the different nature of the organic glues compared to the normally used mineral cements.

4.5 Summary

In the previous section, several mechanical tests have been performed and the results have been discussed. Firstly, slake durability testing on reef blocks revealed very strong weight loss from the samples in the form of single sand grains. This also depended on location, with blocks from one location losing up to 90% after one cycle and up to 97% after two cycles. The other location lost 76% and 94% after the different cycles. The remaining weight after one cycle is in the form of single tube parts and rounded parts while after two cycles mostly small blocks and shell fragments survive. This performance is most similar to some mudrocks. Although the test was aimed at representing the weathering of the reefs by wave impact, the results are more indicative of the transport of fragments along the sea bed by currents. The resistance to wave action would be better tested using wave flumes or an Erosion Function Apparatus.

Secondly, slake durability on single tubes was performed. This showed that the tubes decrease in size along their length and radius at similar rated, although their original elongated shapes means that the decrease in length was greater than in radius. This is related to the tube structure. Given this, it is likely that the tubes have more resistance to weathering in their radius than along its length.

1D compression testing showed that the reef blocks are highly compressible, with strain from 10-

23%. The reefs show a large natural variability with void ratios from 1.15-1.72 and accompanying low densities. The reef blocks showed clear yield points at 80-185 kPa, in contrast to the beach sand which behaved very linearly. About 5-16% of the total strain is recovered when unloading the reefs in contrast to 34% for the beach sand, which showed much lower strain at 2.5%. Although samples have varying void ratios, their closure rate with pressure becomes similar at higher pressure, probably due to the void ratio distribution becoming more similar. The reef blocks show some closure of tubes but the structure is still mostly intact after testing, this is due to rearrangement of particles and stretching of glue spots. The comparison of between loading and unloading stiffness points to the bonds not being fully broken after loading to 604 kPa. Compared to other materials, compressibility of the reefs is very high. It has been shown that the yield points of the reefs are such that they may be damaged by people walking on them. This is however dependent on many factors such as the local conditions and any damage may be quickly repaired. The 1D compression testing method did show the behaviour of the material under common pressures but was limited by its inability to assess the lateral stresses. Also, further loading and unloading above and below the yield point would have been useful to determine the elastic properties of the material.

During shear box testing 3 different reef samples and 3 different beach sand samples were sheared to constant shear stress. The 3 different beach sands were constructed at low, medium and high void ratios. The samples show different volumetric behaviour, with the beach sands dilating during shearing and the reef samples compressing. After testing, the void ratios of some beach sands and some reef samples become very similar at 0.85, although the reefs would probably keep compressing at further shearing. The sands show higher (peak) shear resistance than the reef samples, with denser sands showing higher shear resistance. When fitting a Mohr-Coulomb to the reef sands, they show linear behaviour with cohesion about 23.1 kPa and a friction angle of 21.3°. However, the cohesion is probably under estimated here. The beach sands show no cohesion and a friction angle of about 31-38° depending on void ratio. Inside the structure, after shearing the tubes are bent, broken and often closed. A shear band or shear plane is visible, showing displacement from top and bottom. After testing, samples have an apparent cohesion probably due to some intact bonds, interlocking tube parts and interlocking grains. The stepped approach used in testing may have negatively influenced the testing results as the stopping criterium (constant shear force) was not as suitable as intended.

Several things may have influenced the results, it was highlighted that samples may have experienced some damage from anoxic degradation during storage. Also, the influence of void ratio on sample behaviour seems large, but this could also be due to mistakes or failures during testing.

Lastly, the comparison was made with the behaviour of other cemented sands. Especially in terms of compressibility, the reefs are similar to other cemented sands. However, their lower friction angles and open, tubular structure differ from other cemented sands. Also, in terms of volumetric behaviour and bonds breaking the reef samples differ from other cemented sands.

Chapter 5

Conclusion

5.1 Conclusion

In this study, fieldwork was conducted to investigate the presence of S. Alveolata bioconstructions in the field. The samples collected during this fieldwork were analyzed through extensive imaging using digital and E-SEM microscopy as well as mCT-scanning. The grains were also analyzed and characterized using laser diffraction and powder X-ray diffraction techniques. The microscopy experiments brought reliable observations, as did the P-XRD testing. Laser diffraction was unfortunately less reliable at measuring the grain sizes encountered here. Also, two different versions of slake durability testing were done as well as oedometer and shear box testing while comparing the results against a collected beach sand and literature for cemented sands. The slake durability experiments added interesting details on the durability of the materials. The oedometer and shear experiments gave some insight in the mechanical behaviour, although better results may have been gotten from more applied testing such as flume testing. However, this would have presented their own challenges. As such, the following could be answered.

> How do the S. Alveolata bioconstructions behave in response to different (environmental) loads?

Which was itself subdivided into different subquestions which are answered below.

1. How are these bioconstructions structured and built?

S. Alveolata reefs are built from tubes made of particles bound together with a biogenic glue. In accordance with Sanfilippo et al. (2019), the glue used by the polychaetes was found to have particular bubbly structure with larger bubbles radiating from the center and smaller, circular bubbles surrounding this center. These glue spots also exhibit a face-hardening effect. The glue spots showed brown discoloration after being in the SEM vacuum making them recognizable under a digital microscope. Also, glue spots were quantified for the first time. The glue spots had an average size of 152 μm for sample 6.1A and an average size of 86 μm for sample 5.3. This also showed that in general two shapes of glue spot are commonly found. They are either linear, connecting grains together by their edges or circular, binding the edges of grains. Of these, the linear type is more common. On average, 7-8 glue spots connect a single grain to its neighbours.

The tubes of which the reefs are built up were found to exhibit a particular three layered structure with an inner organic sheath on the inside in which the worm lives, as found before (Fournier-Sowinski, 2013; Vovelle, 1965). This inner sheath partly encapsulates the second layer which is solely made up of flat sand grains which are neatly placed besides each other. These two inner layers are surrounded by a third layer of grains which is preferentially made up of flat particles but can also be (partly) made up of rounded grains where the flat grains are not available. This outer layer of grain is placed in a scale-like manner with grains placed obliquely to the tube axis, partially overlapping the layers around them. Adding upon earlier observations of the tube structure, the relief inside the inner tube was measured and found to be exceptionally flat with a maximum relief of 30 μm.

The structure of the tube is also shown in the volumetric grain distribution which shows that there is no grain size progression over the tube. About half of the tubes consist of large grains with a diameter of about 1 mm, with a significant secondary peak of up to 20% of total volume

represented by grains of about 0.5 mm diameter, but this section is not always present. The rest of the material is often made up of smaller grains covering a size range from 0.5 to 100 μm. This is an expansion of earlier research done by others (Gruet, 1984; Lisco et al., 2020; Naylor & Viles, 2000; Vovelle, 1965), larger grain sizes were found than in these previous studies.

From a mineral composition view point, the tubes contain quartz, calcite, aragonite and sometimes muscovite as well as traces of other minerals. The presence of especially calcite, aragonite and muscovite is probably a result of the preferential selection of flat grains. Calcite and aragonite are common minerals in shells and other biogenic fragments, while muscovite is a platy mineral which are favourable for reef construction.

It was shown for the first time that these tubes are connected to each other with the same glue spots as are used inside the tubes, as well as having some amount of particle interlocking. The tubes do not share any particle layers, creating voids in between tubes which are often filled with sand grains and other materials, ranging from silt to larger pebbles. Alternatively, smaller tubes, probably from juvenile worms were observed crossing through these void spaces.

As widely observed by others, a reef built by S. Alveolata starts from a hard substrate (Naylor & Viles, 2000; Vovelle, 1965; Wilson, 1971), normally a buried rock from observations made here. From this, CT-scans show that tubes start along the substrate before curving upwards. From there, tubes can go many directions. The number of tubes is not constant along the height of the reefs with new tubes starting in between old tubes. Towards the top and the outside of the reef, tubes orient themselves in the currents in such a way to optimally have access to the water currents which provide the polychaete with food and particles necessary for survival. Since no little development was observed in tube diameter or grain sizes inside the tubes and given that tube densities vary, tubes are probably reconstructed during the year.

2. What are their basic mechanical properties?

The reefs showed a very low slake durability index, with an I_{d1} in the 10% range and an I_{d2} of only a few percent. This is indicative of their low resistance to mechanical abrasion. However, some difference was found to exist between different locations, with one location having an index about double of the other. Mainly, tube fragments and small clusters survive in abrasive environments. The reefs did also not show any anisotropy, with remains showing no influence from tube direction. In the respect of erosion resistance, the S. Alveolata reefs are similar to a siltstone stabilized with 5% cement.

Tests also showed that single tubes are susceptible to breaking. Although the relative weathering rates are equal in radius and length, in absolute terms this means that they lose more in their length than in their radius. This points to a larger radial strength than their along their axis. Single tubes are shown to have a density of about 0.34 g/cm.

Unfortunately though, slake durability testing was shown to be a poor analogue for the weathering by wave action often encountered by the reefs. In reality, slake durability testing is a much better analogue of the weathering of tubes and blocks during transport along the sea bed. The resistance to wave action would be better tested using wave flumes or an Erosion Function Apparatus.

Under 1D compression in the axial direction, reefs show strong compressibility. They show strain rates in the order of 10-20% after loading up to 604 kPa, starting from high void ratios of between 1.15-1.72. During testing, with enough load, the reef samples start to exhibit similar closure rates independent of their initial void ratios. However, this rate is still much higher than that of comparable beach sand. Void ratios are also still higher than most normal sands even after tested. The reefs also show clear yield points at 80, 100 and 185 kPa depending on the sample. There the initial, relatively stiff and elastic response changes to large plastic strains. However, even initially the reefs respond less stiff than the beach sand. This variability between samples is visible in many aspects of their behaviour. Even after testing, bonds in the reef samples are not fully broken and it behaves cohesively. Tubes inside the samples are partly but not fully closed.

Under stepped shearing in the shear box, the reefs show lower shear resistance than the beach sand tested here. They exhibit contraction in volume under shearing in contrast with tested beach sands which always showed some amount of dilation. As a result of this, two beach sand and two reef samples ended up at a similar void ratio after testing. However, the beach sands did not exhibit a constant void ratio at that point and were still contracting. The reefs conform well to the linear Mohr-Coulomb criteria, showing a cohesion of about 23 kPa and a friction angle of about 21°. These friction angles are lower than other beach sands, probably due to the structure of the

scale-like outer layer and inner lining that align the sand particles inside the reefs. However, since tubes also interlock, the friction angle is a result of both interparticle and intertube friction.

During shearing the internal structure of the reef blocks is deformed. Tubes are bent in the initial stages. With further shearing, the tubes are broken in places and a shear band or shear plane is formed. Even though the reefs show widespread damage during shearing, some residual structure is left after testing and it has an apparent cohesion. This apparent cohesion is probably due to some intact bonds, interlocking tube parts and interlocking grains. Testing did show that at this point the void ratio of the samples is similar to that of other sands but would probably keep decreasing to lower values than found in testing. Given this, the reefs are built from relatively densely packed grains inside the tube walls, making for a relatively compact structure after loading.

Comparing these reefs to other (cemented) sands shows many similarities to these materials. These include among others, the applicability of the linear Mohr-Coulomb criteria and the high compressibilities of the reefs. However, several differences are present such as the absence of high friction angles in the reefs and the higher void ratios compared to other cemented sands. The reefs also do not show any brittle response but behave much more ductile than many other cemented sands.

3. How do these materials respond to environmental pressures (such as wave impacts and human trampling)?

Although the results from the tests performed in this thesis are not extensive and detailed enough to make a detailed analysis, some initial aspects stand out. Firstly, the pressure exerted from a person walking is in the same range of the yield stresses found in this study. This means that depending on the natural variability, walking individuals could definitely pose a threat to the reefs. The impact of waves on the reefs is more difficult to assess but bed shear stresses are far lower than the shear resistance of the material. The pressure exerted by waves, estimated to be about 36 kPa is much lower than any yield stresses and also lower than the shear resistance of the reefs although this is difficult to determine as it depends on many different factors.

Looking at the damages to the reefs during testing, under 1D compression yield stresses are about 80-185 kPa. Although the pressures exerted by walking are higher than this, they only last a very short time, as such the yield stresses are exceeded but the damage to the tube structure is limited. Tubes are still open and visible, even after much higher loads. Under conditions of shear, stress initially becomes constant at a displacement similar to the diameter of a single tube. This corresponds to a peak stress of 38-50 kPa, and means that they will probably survive normal wave loading. Bed shear stresses from waves are also lower than these, so should not pose a problem for the reefs.

5.2 Further recommendations

Given the results of these experiments as outlined above, many questions do remain. As many tests described in this thesis are relatively rudimentary, more detailed and applied tests would be useful to better determine the environmental impacts on the reefs. Also, repeat testing of the material would be useful to more fully capture the natural variability in these reefs which could only be captured in these tests to a limited extend. At the same time, testing of the probable anisotropy in behaviour in the samples is recommended to better understand the material. Also the response of the reefs as a mass to wave energy would be an interesting subject of further study. This because of the suggested wave energy attenuation of the reefs (Le Cam et al., 2011), but this has only been looked at in relation to the material and not in relation with the mass properties and the irregular geometry of the reefs. At the same time, long-term response of the reefs is not classified here and would be an interesting subject.

Also, questions remain to the variability of the reefs and the relation of this to the mechanical properties. The mechanisms by which the reefs are built up and gain their strength are not fully understood, as the roles of the different linings of the tubes is not entirely clear in this aspect. In this respect, the question also still remains if the size and amount of glue spots is governed by the hydrodynamic conditions of if this is also related to the granulometry of the reefs and the available building materials. The possible differences in behaviour of reefs from different locations and different wave regimes could also make for new studies. This would shine a light on the adaptability of S. Alveolata and its bioconstruction.

Looking back, the mechanical tests performed have one major shortfall. They were not combined with a structured program of imaging and structural investigation. For any of the above mentioned

tests, observation of the structure before, during and after testing is at least highly recommended or even an absolute necessity depending on the exact test. Such investigations are necessary to establish the influence of loading on the S. A. individuals occupying the tubes.

In terms of applicability, three main directions emerge as well. As we know from other research, many threats anthropogenic threats of the reefs exist such as trawling, dredging and human trampling (Dubois et al., 2002; Plicanti et al., 2016; Riesen & Reise, 1982). These threats could be investigated in terms of mechanical impacts to the reefs along with their mechanical properties to better assess the environmental threats to the reefs.

A second very interesting direction of further research is the application of the glue as a soil strengthening agent along the lines of enzyme-induced carbonate precipitation (Ahenkorah et al., 2021), given that the synthesis (Becker et al., 2012) and use of the glue in several applications is already a growing area of research. Gruet et al. (1987) already researched the working of the glue early on. Applications include the replacement of tar in asphalt (Buffet et al., 2018) and as a glue in surgical applications (Shao et al., 2009). Also, comparing this to more conventional methods in terms of strength and durability but also in terms of costs and CO_2 production during the life cycle of the product would make for an interesting advancement of coastal protection and ground improvement.

Thirdly, this material may have an interesting application in coastal protection as suggested by Perricone et al. (2023). Growing it on structures such as groynes has certain challenges such as providing the right environmental parameters for their procreation in terms of food and particle supply. However, if this would succeed, regrowing coastal protection with additional environmental benefits in terms of species diversity could be a reality.

However, these reefs are not the only ecosystem that could hold such promise. Several species, among which the species H. Nirae alter their environments and could positively contribute to many different applications from coastal protection (such as sabellaria reefs) to maybe ground improvements by altering soft sediments such as H. Nirae does. A short study of H. Nirae highlighting some of its features is found in appendix F.

Bibliography

Ahenkorah, I., Rahman, M. M., Karim, M. R., & Beecham, S. (2021). Enzyme induced calcium carbonate precipitation and its engineering application: A systematic review and meta-analysis. *Construction and Building Materials*, *308*, 125000. https://doi.org/10.1016/j.conbuildmat.2021.125000

Allman, M. A., & Poulos, H. G. (1988). Stress-strain behaviour of an artificially cemented calcareous soil [Num Pages: 10]. In *Engineering for calcareous sediments volume 1*. CRC Press.

Alves, R. M. S., Vanaverbeke, J., Bouma, T. J., Guarini, J.-M., Vincx, M., & Van Colen, C. (2017). Effects of temporal fluctuation in population processes of intertidal lanice conchilega (pallas, 1766) aggregations on its ecosystem engineering. *Estuarine, Coastal and Shelf Science*, *188*, 88–98. https://doi.org/10.1016/j.ecss.2017.02.012

Ankara, H., Çiçek, F., Deniz, I. T., Uçak, E., & Kandemir, S. Y. (2016). Determination of slake durability index (sdi) values on different shape of laminated marl samples. *IOP Conference Series: Earth and Environmental Science*, *44*, 022006. https://doi.org/10.1088/1755-1315/44/2/022006

Becker, P. T., Lambert, A., Lejeune, A., Lanterbeco, D., & Flammang, P. (2012). Identification, characterization, and expression levels of putative adhesive proteins from the tube-dwelling polychaete sabellaria alveolata. *Biological Bulletin*, *223*(2), 217–225. http://www.jstor.org/stable/41759008

Beuselinck, L., Govers, G., Poesen, J., Degraer, G., & Froyen, L. (1998). Grain-size analysis by laser diffractometry: Comparison with the sieve-pipette method. *CATENA*, *32*(3), 193–208. https://doi.org/10.1016/S0341-8162(98)00051-4

Boey, C., & Carter, J. (1988). Mechanical testing of artificially cemented carbonate soil. *Proceedings of the Australia-New Zealand conference on geomechanics*, *1*, 145–149.

Briaud, J.-L., & Chen, H.-C. (2005). The EFA, erosion function apparatus: An overview. *Proceedings of the 16th International Conference on Soil Mechanics and Geotechnical Engineering*, *2*, 479–483. https://doi.org/doi:10.3233

Broman, E., Sjöstedt, J., Pinhassi, J., & Dopson, M. (2017). Shifts in coastal sediment oxygenation cause pronounced changes in microbial community composition and associated metabolism. *Microbiome*, *5*(1), 96. https://doi.org/10.1186/s40168-017-0311-5

Bruschetti, M. (2019). Role of reef-building, ecosystem engineering polychaetes in shallow water ecosystems [Number: 9 Publisher: Multidisciplinary Digital Publishing Institute]. *Diversity*, *11*(9), 168. https://doi.org/10.3390/d11090168

BS 1377-2. (1990). British standard methods of test for soils for civil engineering purposes [OCLC: 25807498].

Buffet, J.-P., Corre, E., Duvernois-Berthet, E., Fournier, J., & Lopez, P. J. (2018). Adhesive gland transcriptomics uncovers a diversity of genes involved in glue formation in marine tube-building polychaetes. *Acta Biomaterialia*, *72*, 316–328. https://doi.org/10.1016/j.actbio.2018.03.037

Buffet, J.-P., Fournier-Sowinski, J., Denis, J.-B., Puchol, M., & Lopez, P. (2017, June 13). *Marine bio-glue: From molecular characterization to applications in wet environments* (Poster) [Poster]. https://doi.org/10.13140/RG.2.2.34089.24169

Butterfield, R. (1979). A natural compression law for soils (an advance on e–log p) [Publisher: ICE Publishing]. *Géotechnique*, *29*(4), 469–480. https://doi.org/10.1680/geot.1979.29.4.469

Cavanagh, P. R., Rodgers, M. M., & liboshi, A. (1987). Pressure distribution under symptom-free feet during barefoot standing [Publisher: SAGE Publications]. *Foot & Ankle*, *7*(5), 262–278. https://doi.org/10.1177/107110078700700502

Chai, Y., Jiang, D.-P., Wang, F.-J., & Lyu, H.-B. (2021). Investigation of engineering properties of cement-stabilized calcareous sand foundation [Publisher: Hindawi]. *Advances in Materials Science and Engineering*, *2021*, e9188560. https://doi.org/10.1155/2021/9188560

Champilou, J.-B., Baltzer, A., Murat, A., Reynaud, M., Maillet, G. M., Nardelli, M. P., & Metzger, E. (2019). New evidence of perfect overlapping of haploops and pockmarks field: Is it a coincidence? *Marine Geology*, *415*, 105961. https://doi.org/10.1016/j.margeo.2019.105961

Clough, W., Sitar, N., & Bachus, R. (1981). Cemented sands under static loading. *Journal of the Geotechnical Engineering Division*, *107*, 799–817. https://doi.org/10.1061/AJGEB6.0001152

Collin, A., Dubois, S., Ramambason, C., & Etienne, S. (2018). Very high-resolution mapping of emerging biogenic reefs using airborne optical imagery and neural network: The honeycomb worm (*Sabellaria alveolata*) case study. *International Journal of Remote Sensing*, *39*(17), 5660–5675. https://doi.org/10.1080/01431161.2018.1484964

Collins, B., & Sitar, N. (2009). Geotechnical properties of cemented sands in steep slopes. *Journal of Geotechnical and Geoenvironmental Engineering - J GEOTECH GEOENVIRON ENG*, *135*. https://doi.org/10.1061/(ASCE)GT.1943-5606.0000094

Coop, M. R., & Atkinson, J. H. (1993). The mechanics of cemented carbonate sands [Publisher: ICE Publishing]. *Géotechnique*, *43*(1), 53–67. https://doi.org/10.1680/geot.1993.43.1.53

Cuccovillo, T., & Coop, M. R. (1999). On the mechanics of structured sands. *Géotechnique*, *49*(6), 741–760. https://doi.org/10.1680/geot.1999.49.6.741

Cuomo, G., Allsop, W., Bruce, T., & Pearson, J. (2010). Breaking wave loads at vertical seawalls and breakwaters. *Coastal Engineering*, *57*(4), 424–439. https://doi.org/10.1016/j.coastaleng.2009.11.005

Curd, A. (2020, July 7). *On the macroecology and global distribution of the ecosystem engineer; sabellaria alveolata in a changing world.* (Doctoral dissertation). L'UNIVERSITE DE BRETAGNE OCCIDENTALE. Plouzané. Retrieved April 20, 2023, from https://theses.hal.science/tel-03738043/document

Curd, A., Cordier, C., Firth, L. B., Bush, L., Gruet, Y., Le Mao, P., Blaze, J. A., Board, C., Bordeyne, F., Burrows, M. T., Cunningham, P. N., Davies, A. J., Desroy, N., Edwards, H., Harris, D. R., Hawkins, S. J., Kerckhof, F., Lima, F. P., McGrath, D., ... Dubois, S. (2020). A broad-scale long-term dataset of sabellaria alveolata distribution and abundance curated through the REEHAB (REEf HABitat) project. https://doi.org/10.17882/72164

Curd, A., Pernet, F., Corporeau, C., Delisle, L., Firth, L. B., Nunes, F. L., & Dubois, S. F. (2019). Connecting organic to mineral: How the physiological state of an ecosystem-engineer is linked to its habitat structure. *Ecological Indicators*, *98*, 49–60. https://doi.org/10.1016/j.ecolind.2018.10.044

D' Angremond, K., & Pluim-van der Velden, E. T. J. M. (2001). Introduction to coastal engineering [Publisher: TU Delft, Section Hydraulic Engineering]. *Collegedictaat CT4300*. Retrieved February 20, 2023, from https://repository.tudelft.nl/islandora/object/uuid%3Afa54d9a3-e52b-42af-a76e-28b5a64da764

Delbono, I., Bianchi, C., & Morri, C. (2003, September 1). Le biocostruzioni di sabellaria alveolata come indicatori ambientali: Area costiera fra chiavari e sestri levante. In *Studi per la creazione di strumenti di gestione costiera* (pp. 130–140). Golfo del Tigullio.

Direct shear — geotechnical testing lab. (n.d.). Retrieved July 12, 2024, from https://research.iitgn.ac.in/stl/direct-shear/

Dubois, S., Retière, C., & Olivier, F. (2002). Biodiversity associated with sabellaria alveolata (polychaeta: Sabellariidae) reefs: Effects of human disturbances [Publisher: Cambridge University Press]. *Journal of the Marine Biological Association of the United Kingdom*, *82*(5), 817–826. https://doi.org/10.1017/S0025315402006185

Fernlund, J. M. R., Zimmerman, R. W., & Kragic, D. (2007). Influence of volume/mass on grain-size curves and conversion of image-analysis size to sieve size. *Engineering Geology*, *90*(3), 124–137. https://doi.org/10.1016/j.enggeo.2006.12.007

Firth, L. B., Mieszkowska, N., Grant, L. M., Bush, L. E., Davies, A. J., Frost, M. T., Moschella, P. S., Burrows, M. T., Cunningham, P. N., Dye, S. R., & Hawkins, S. J. (2015). Historical comparisons reveal multiple drivers of decadal change of an ecosystem engineer at the range edge [_eprint: https://onlinelibrary.wiley.com/doi/pdf/10.1002/ece3.1556]. *Ecology and Evolution*, *5*(15), 3210–3222. https://doi.org/10.1002/ece3.1556

Fournier-Sowinski, J. (2013, January 1). *Bioconstructions d'annélides polychètes. complexité des niveaux d'organisation, de l'organisme à l'écosystème.* Université de Bretagne Occidentale.

Ghafghazi, M., Shuttle, D. A., & DeJong, J. T. (2014). Particle breakage and the critical state of sand. *Soils and Foundations*, *54*(3), 451–461. https://doi.org/10.1016/j.sandf.2014.04.016

Gravina, M. F., Cardone, F., Bonifazi, A., Bertrandino, M. S., Chimienti, G., Longo, C., Marzano, C. N., Moretti, M., Lisco, S., Moretti, V., Corriero, G., & Giangrande, A. (2018). Sabellaria spinulosa (polychaeta, annelida) reefs in the mediterranean sea: Habitat mapping,

dynamics and associated fauna for conservation management. *Estuarine, Coastal and Shelf Science*, *200*, 248–257. https://doi.org/10.1016/j.ecss.2017.11.017

Grieve, D. W., & Rashdi, T. (1984). Pressures under normal feet in standing and walking as measured by foil pedobarography. *Annals of the Rheumatic Diseases*, *43*(6), 816–818. https://doi.org/10.1136/ard.43.6.816

Gruet, Y., & Bodeur, Y. (1994). Sélection des grains de sable selon leur nature et leur forme par sabellaria alveolata linné (polychète, sabellariidé) lors de la reconstruction expérimentale de son tube. *Mémoires du Muséum national d'Histoire naturelle. Série A, Zoologie*. Retrieved February 10, 2023, from https://www.waterbouwkundiglaboratorium.be/en/publications/open-fhr-archive

Gruet, Y. (1972). Aspects morphologiques et dynamiques de constructions de l'Annelide polychete Sabellaria alveolata (Linne). [Issue: 2 Pages: 131-161 Publication Title: Revue des Travaux de l'Institut des Pêches Maritimes Type: Article Volume: 36]. *Revue des Travaux de l'Institut des Pêches Maritimes*, *36*(2), 131–161. https://archimer.ifremer.fr/doc/00000/2061/

Gruet, Y. (1984). Granulometric evolution of the sand tube in relation to growth of the polychaete annelid *Sabellaria alveolata* (linné) (sabellariidae). *Ophelia*, *23*(2), 181–193. https://doi.org/10.1080/00785326.1984.10426613

Gruet, Y. (1986). Spatio-temporal changes of sabellarian reefs built by the sedentary polychaete sabellaria alveolata (linné) [_eprint: https://onlinelibrary.wiley.com/doi/pdf/10.1111/j.1439-0485.1986.tb00166.x]. *Marine Ecology*, *7*(4), 303–319. https://doi.org/10.1111/j.1439-0485.1986.tb00166.x

Gruet, Y., Vovelle, J., & Grasset, M. (1987). Composante biominérale du ciment du tube chez *Sabellaria alveolata* (L.), Annélide Polychète. *Canadian Journal of Zoology*, *65*(4), 837–842. https://doi.org/10.1139/z87-133

Haldar, S. K., & Tišljar, J. (2014, January 1). Chapter 5 - sedimentary rocks. In S. K. Haldar & J. Tišljar (Eds.), *Introduction to mineralogy and petrology* (pp. 121–212). Elsevier. https://doi.org/10.1016/B978-0-12-408133-8.00005-5

Hartono, E., Wardani, S. P. R., & Muntohar, A. S. (2019). SLAKE DURABILITY OF THE COMPACTED-SILTSTONE FRAGMENT WITH CEMENT STABILIZATION. *International Journal of GEOMATE*, *17*(64). https://doi.org/10.21660/2019.64.84678

Head, K. H., & Epps, R. (2011). *Permeability, shear strength and compressibility tests* (3. ed). Whittles.

HELCOM Red List Biotope Expert Group. (2013). Biotope information sheet: Baltic aphotic muddy sediment dominated by haploops spp. Retrieved February 13, 2023, from https://helcom.fi/wp-content/uploads/2019/08/HELCOM-Red-List-AB.H1I2.pdf

Hessert, M. J., Vyas, M., Leach, J., Hu, K., Lipsitz, L. A., & Novak, V. (2005). Foot pressure distribution during walking in young and old adults. *BMC Geriatrics*, *5*(1), 8. https://doi.org/10.1186/1471-2318-5-8

Hong, S., Lee, H., & Lee, H. (2014). Controlling mechanical properties of bio-inspired hydrogels by modulating nano-scale, inter-polymeric junctions [Publisher: Beilstein-Institut]. *Beilstein Journal of Nanotechnology*, *5*(1), 887–894. https://doi.org/10.3762/bjnano.5.101

Ile de noirmoutier - barbatre surf forecast and surf report. (n.d.). Retrieved September 3, 2024, from https://www.surf-forecast.com/breaks/Ile-de-Noirmoutier-Barbatre/forecasts/latest/six_day

Jamiolkowski, M., Lo Presti, D. C. F., & Manassero, M. (2003). Evaluation of relative density and shear strength of sands from CPT and DMT. *Soil Behavior and Soft Ground Construction*, 201–238. https://doi.org/10.1061/40659(2003)7

Kaneko, D., Wang, S., Matsumoto, K., Kinugawa, S., Yasaki, K., Chi, D. H., & Kaneko, T. (2011). Mussel-mimetic strong adhesive resin from bio-base polycoumarates [Publisher: Nature Publishing Group]. *Polymer Journal*, *43*(10), 855–858. https://doi.org/10.1038/pj.2011.77

Katiyar, N. K., Goel, G., Hawi, S., & Goel, S. (2021). Nature-inspired materials: Emerging trends and prospects [Number: 1 Publisher: Nature Publishing Group]. *NPG Asia Materials*, *13*(1), 1–16. https://doi.org/10.1038/s41427-021-00322-y

Keyence International. (2023). *Digitale microscoop - VHX-7000-reeks. keyence international belgium (nederlands).* Retrieved December 11, 2023, from https://www.keyence.eu/nlnl/products/microscope/digital-microscope/vhx-7000/?aw=KIB01kw1_11488492&gad_source=1&gclid=CjwKCAiAg9urBhB_EiwAgw88mSYp67Goy8STP77Szqx7DtsfLuuJgylbOGN7hOjcKINuzC
BwE

Kirchman, D. L. (2012). *Processes in microbial ecology* [OCLC: ocn757930826]. Oxford University Press.

Lade, P. V., & Trads, N. (2014). The role of cementation in the behaviour of cemented soils [Publisher: ICE Publishing]. *Geotechnical Research*, *1*(4), 111–132. https://doi.org/10.1680/gr.14.00011

Le Cam, J.-B., Fournier, J., Etienne, S., & Couden, J. (2011). The strength of biogenic sand reefs: Visco-elastic behaviour of cement secreted by the tube building polychaete sabellaria alveolata, linnaeus, 1767. *Estuarine, Coastal and Shelf Science*, *91*(2), 333–339. https://doi.org/10.1016/j.ecss.2010.10.036

Li, H. Y., Chai, H. W., Xiao, X. H., Huang, J. Y., & Luo, S. N. (2020). Fractal breakage of porous carbonate sand particles: Microstructures and mechanisms. *Powder Technology*, *363*, 112–121. https://doi.org/10.1016/j.powtec.2020.01.007

Linnaeus, C. (1767). *Systema naturae per regna tria naturae : Secundum classes, ordines, genera, species, cum characteribus, differentiis, synonymis, locis* (Editio decima tertia, ad editionem duodecimam reformatam Holmiensem., Vol. 1) [Pages: 1-842]. Typis Ioannis Thomae. https://www.biodiversitylibrary.org/item/83650

Lisco, S. N., Acquafredda, P., Gallicchio, S., Sabato, L., Bonifazi, A., Cardone, F., Corriero, G., Gravina, M. F., Pierri, C., & Moretti, M. (2020). The sedimentary dynamics of sabellaria alveolata bioconstructions (ostia, tyrrhenian sea, central italy). *Journal of Palaeogeography*, *9*(1), 2. https://doi.org/10.1186/s42501-019-0050-6

Lisco, S. N., Moretti, M., Moretti, V., Cardone, F., Corriero, G., & Longo, C. (2017). Sedimentological features of sabellaria spinulosa biocontructions. *Marine and Petroleum Geology*, *87*, 203–212. https://doi.org/10.1016/j.marpetgeo.2017.06.013

Lisco, S. N., Pierri, C., Lazic, T., Bonifazi, A., Gravina, M. F., Giangrande, A., Acquafredda, P., & Moretti, M. (2021). Sabellaria alveolata versus sabellaria spinulosa reefs along the italian coasts: A new methodological proposal to compare different growth models [Number: 10 Publisher: Multidisciplinary Digital Publishing Institute]. *Geosciences*, *11*(10), 426. https://doi.org/10.3390/geosciences11100426

Lourenço, C. R., Nicastro, K. R., McQuaid, C. D., Krug, L. A., & Zardi, G. I. (2020). Strong upwelling conditions drive differences in species abundance and community composition along the atlantic coasts of morocco and western sahara. *Marine Biodiversity*, *50*(2), 15. https://doi.org/10.1007/s12526-019-01032-z

Lovley, D. R. (1997). Microbial fe(III) reduction in subsurface environments. *FEMS Microbiology Reviews*.

Maréchal, J.-C., & Rouillard, J. (2020, March 17). Groundwater in france: Resources, use and management issues. https://doi.org/10.1007/978-3-030-32766-8_2

Muller, A., Poitrimol, C., Nunes, F. L. D., Boyé, A., Curd, A., Desroy, N., Firth, L. B., Bush, L., Davies, A. J., Lima, F. P., Marzloff, M. P., Meneghesso, C., Seabra, R., & Dubois, S. F. (2021). Musical chairs on temperate reefs: Species turnover and replacement within functional groups explain regional diversity variation in assemblages associated with honeycomb worms. *Frontiers in Marine Science*, *8*, 654141. https://doi.org/10.3389/fmars.2021.654141

Multer, H. G., & Milliman, J. D. (1967). Geologic aspects of sabellarian reefs, southeastern florida. *Bulletin of Marine Science*, *17*, 257–267.

Naito, M., Hayakawa, O., Nakahira, K., Mori, H., & Tsubaki, J. (1998). Effect of particle shape on the particle size distribution measured with commercial equipment. *Powder Technology*, *100*(1), 52–60. https://doi.org/10.1016/S0032-5910(98)00052-7

Nakata, Y., Hyodo, M., Hyde, A. F. L., Kato, Y., & Murata, H. (2001). Microscopic particle crushing of sand subjected to high pressure one-dimensional compression. *Soils and Foundations*, *41*(1), 69–82. https://doi.org/10.3208/sandf.41.69

Naylor, L. A., & Viles, H. A. (2000). A temperate reef builder: An evaluation of the growth, morphology and composition of sabellaria alveolata (l.) colonies on carbonate platforms in south wales [Publisher: The Geological Society of London]. *Geological Society, London, Special Publications*, *178*(1), 9–19. https://doi.org/10.1144/GSL.SP.2000.178.01.02

Nichols, G. (2009). *Sedimentology and stratigraphy* (2nd ed) [OCLC: ocn259754358]. Wiley-Blackwell.

Nicoletti, L., Lattanzi, L., La Porta, B., La Valle, P., Gambi, M., Tomasseti, P., Tucci, P., & Chimenz Gusso, C. (2001). Sabellaria reefs from the latium coast (central tyrrhenian sea). *Biologia Marina Mediterranea*, *8*(1), 252–258.

Noernberg, M. A., Fournier, J., Dubois, S., & Populus, J. (2010). Using airborne laser altimetry to estimate sabellaria alveolata (polychaeta: Sabellariidae) reefs volume in tidal flat environments. *Estuarine, Coastal and Shelf Science*, *90*(2), 93–102. https://doi.org/10.1016/j.ecss.2010.07.014

OSPAR commission. (2021). Case report for haploops habitat. Retrieved February 13, 2023, from https://www.ospar.org/documents?v=46861

Parker, J. (1983). A comparison of methods used for the measurement of organic matter in marine sediment. *Chemistry in Ecology*, *1*, 201–209. https://doi.org/10.1080/02757548308070802

Perricone, V., Mutalipassi, M., Mele, A., Buono, M., Vicinanza, D., & Contestabile, P. (2023). Nature-based and bioinspired solutions for coastal protection: An overview among key ecosystems and a promising pathway for new functional and sustainable designs (S. Degraer, Ed.). *ICES Journal of Marine Science*, *80*(5), 1218–1239. https://doi.org/10.1093/icesjms/fsad080

Plicanti, A., Domínguez, R., Dubois, S. F., & Bertocci, I. (2016). Human impacts on biogenic habitats: Effects of experimental trampling on *Sabellaria alveolata* (linnaeus, 1767) reefs. *Journal of Experimental Marine Biology and Ecology*, *478*, 34–44. https://doi.org/10.1016/j.jembe.2016.02.001

Polakowski, C., Sochan, A., Bieganowski, A., Ryżak, M., Földényi, R., & Toth, J. (2014). Influence of the sand particle shape on particle size distribution measured by laser diffraction method. *International Agrophysics*, *28*, 195–200. https://doi.org/10.2478/intag-20014-0008

Prakash, K., Sridharan, A., Manoj, N., & Manoj. (2023). Friction angles of sands: An appraisal. *Geotechnical and Geological Engineering*, *41*(8), 4865–4872. https://doi.org/10.1007/s10706-023-02548-9

Reddy, K. R., & Saxena, S. K. (1993). Effects of cementation on stress-strain and strength characteristics of sands. *Soils and Foundations*, *33*(4), 121–134. https://doi.org/10.3208/sandf1972.33.4_121

Reeuwijk, L. P. v. (2002). *Procedures for soil analysis* (6. ed). International Soil Reference; Information Centre.

Reynaud, M. (2014). Rôle des pockmarks dans l'activité de bioconstruction de Haploops nirae. https://dumas.ccsd.cnrs.fr/dumas-01019920

Riesen, W., & Reise, K. (1982). Macrobenthos of the subtidal wadden sea: Revisited after 55 years [Number: 4 Publisher: BioMed Central]. *Helgoländer Meeresuntersuchungen*, *35*(4), 409–423. https://doi.org/10.1007/BF01999132

Rigolet, C. (2013). *Diversité structurelle et fonctionnelle des peuplements sablo-vaseux de Bretagne sud: Impact de l'expansion d'Haploops nirae* (Doctoral dissertation). L'UNIVERSITE PIERRE ET MARIE CURIE. Paris. Retrieved February 9, 2023, from http://rgdoi.net/10.13140/RG.2.1.3698.1280

Rigolet, C., Le Souchu, P., Caisey, X., & Dubois, S. F. (2011). Group sweeping: Feeding activity and filtration rate in the tubiculous amphipod haploops nirae (kaim-malka, 1976). *Journal of Experimental Marine Biology and Ecology*, *406*(1), 29–37. https://doi.org/10.1016/j.jembe.2011.06.006

Rodgers, M. M. (1995). Dynamic foot biomechanics. *Journal of Orthopaedic & Sports Physical Therapy*, *21*(6), 306–316. https://doi.org/10.2519/jospt.1995.21.6.306

Roux, A. L. (2008, April 7). *Sabellaria alveolata, partie antérieure de l'animal sorti de son tube.* Retrieved April 5, 2023, from https://commons.wikimedia.org/wiki/File:Sabellaria_alveolata_b.JPG

Sanfilippo, R., Rosso, A., Mastandrea, A., Viola, A., Deias, C., & Guido, A. (2019). *Sabellaria alveolata* sandcastle worm from the mediterranean sea: New insights on tube architecture and biocement. *Journal of Morphology*, *280*(12), 1839–1849. https://doi.org/10.1002/jmor.21069

Shao, H., Bachus, K. N., & Stewart, R. J. (2009). A water-borne adhesive modeled after the sandcastle glue of *P. californica*: A water-borne adhesive modeled after the sandcastle glue of... *Macromolecular Bioscience*, *9*(5), 464–471. https://doi.org/10.1002/mabi.200800252

Sitar, N. (1983). Slope stability in coarse sediments. *Geological Environment and Soil Properties (paper prepared in conjunction with the ASCE Geotechnical Engineering Division and the ASCE Convention, Houston, Texas, 17–21 Oct 1983)*, *22*(5), 161. https://doi.org/10.1016/0148-9062(85)92274-0

Skafel, M. G., & Bishop, C. T. (1994). Flume experiments on the erosion of till shores by waves. *Coastal Engineering*, *23*(3), 329–348. https://doi.org/10.1016/0378-3839(94)90009-4

Temmerman, S., Meire, P., Bouma, T. J., Herman, P. M. J., Ysebaert, T., & De Vriend, H. J. (2013). Ecosystem-based coastal defence in the face of global change [Number: 7478 Publisher: Nature Publishing Group]. *Nature*, *504*(7478), 79–83. https://doi.org/10.1038/nature12859

Tervoort, J. (2022, June 10). *Comparing wave transformation of a hard, impermeable structure with various biogenic, permeable structures* (MSc Thesis). Utrecht University. Utrecht.

Retrieved April 13, 2023, from https://studenttheses.uu.nl/bitstream/handle/20.500.12932/43390/Thesis_JanTervoort.pdf?sequence=1

TESCAN. (n.d.). *TESCAN CoreTOM micro CT*. Retrieved December 11, 2023, from https://info.tescan.com/coretom-micro-ct

Thappeta, S. K., Johnson, J. P. L., Halfi, E., Peretz, Y. S., & Laronne, J. B. (2023). Bed shear stress in experimental flash flood bores over dry beds and over flowing water: A comparison of methods [Publisher: American Society of Civil Engineers]. *Journal of Hydraulic Engineering*, *149*(4), 04023001. https://doi.org/10.1061/JHEND8.HYENG-13029

Tide times and charts for pornichet, pays-de-la-loire and weather forecast for fishing in pornichet in 2023. (n.d.). Retrieved August 15, 2024, from https://tides4fishing.com/fr/pays-de-la-loire/pornichet

Tunnicliffe, V. (1982). The effects of wave-induced flow on a reef coral. *Journal of Experimental Marine Biology and Ecology*, *64*(1), 1–10. https://doi.org/10.1016/0022-0981(82)90064-8

Ulusay, R., & Hudson, J. A. (2007). *The complete ISRM suggested methods for rock characterization, testing and monitoring: 1974-2006* (April 2007 ed) [OCLC: 161605085]. Commission on Testing Methods, International Society of Rock Mechanics.

van der Reijden, K. J., Koop, L., O'Flynn, S., Garcia, S., Bos, O., van Sluis, C., Maaholm, D. J., Herman, P. M. J., Simons, D. G., Olff, H., Ysebaert, T., Snellen, M., Govers, L. L., Rijnsdorp, A. D., & Aguilar, R. (2019). Discovery of sabellaria spinulosa reefs in an intensively fished area of the dutch continental shelf, north sea. *Journal of Sea Research*, *144*, 85–94. https://doi.org/10.1016/j.seares.2018.11.008

Van Duren, L., Gittenberger, A., Smaal, A., van Koningsveld, M., Osinga, R., Cado van der Lelij, J., & de Vries, M. (2017). *Rich reefs in the north sea; exploring the possibilities of promoting the establishment of natural reefs and colonisation of artificial hard substrate* (No. 1221293-000). Deltares. Retrieved April 19, 2023, from https://publications.deltares.nl/1221293_000_Eng.pdf

Vorberg, R. (2000). Effects of shrimp fisheries on reefs of sabellaria spinulosa (polychaeta). *ICES Journal of Marine Science*, *57*(5), 1416–1420. https://doi.org/10.1006/jmsc.2000.0920

Vovelle, J. (1965, October 12). *Le tube de Sabellaria alveolata (L.) Annélide Polychète Hermellidae et son ciment. Étude écologique, expérimentale, histologique et histochimique.* (Doctoral dissertation). Université de Paris. Paris.

Wantha, S. (2021, November 18). *Xtra library for thermo scientific amira, avizo and PerGeos software — porosity volume fraction analysis* [Porosity volume fraction analysis]. Retrieved July 15, 2024, from https://www.thermofisher.com/software-em-3d-vis/xtra-library/xtras/porosity-volume-fraction-analysis

Wilson, D. P. (1971). Sabellaria colonies at duckpool, north cornwall, 1961–1970 [Publisher: Cambridge University Press]. *Journal of the Marine Biological Association of the United Kingdom*, *51*(3), 509–580. https://doi.org/10.1017/S002531540001496X

Yang, Y., Zhang, C., Wang, R., Jiang, M., & Tian, Y. (2021). Engineering properties of the compressibility and crushing characteristics of transitional soils mixed with silicate and carbonate sands. *Engineering Geology*, *292*, 106246. https://doi.org/10.1016/j.enggeo.2021.106246

Zhang, J., Hüpers, A., Kreiter, S., & Kopf, A. (2021). Pore pressure regime and fluid flow processes in the shallow nankai trough subduction zone based on experimental and modeling results from IODP site c0023. *Journal of Geophysical Research: Solid Earth*, *126*. https://doi.org/10.1029/2020JB020248

Appendices

Table of Appendices

Appendix A

Fieldwork description, procedures and locations

For the tests described in this thesis, several samples needed to be collected. To do this, a fieldwork was organized from the 3rd of may to the 9th of may in the sampling area. These dates were chosen to coincide with the spring tides in order to take advantage of the low water levels. During this fieldwork, samples of Sabellaria Alveolata and Haploops Nirae constructions were taken. These samples were subsequently transported to the Netherlands and stored in the cool sample storage room at the Delft University of Technology until they were used for tests.

A.1 Sampling locations

Over the duration of the fieldwork several locations were visited, mostly around the isle of Noîrmoutier and the town of Pornichet as displayed in figure 2.1.1. The H. Nirae constructions were sampled at sea, just outside the harbour of La Turballe. Also, during the fieldwork some L. Conchilega constructions were encountered and sampled as well, together with some beach sand collected at the same location.

Location Number	**Species Sampled**	**Latitude**	**Longitude**	**GPS Elevation**	**Time & Date Logged**
5.1	S. Alveolata	47.01134223	-2.219386	-1.365609674	2023/05/05 09:46:25+00
5.2	S. Alveolata	47.02686095	-2.24510382	0.889763224	2023/05/05 11:22:00+00
5.3	S. Alveolata	46.97441262	-2.27738127	-0.994736838	2023/05/05 13:06:35+00
6.1A	S. Alveolata	47.25535062	-2.34070828	-4.427535349	2023/05/06 10:37:16+00
6.1B	S. Alveolata	47.25499288	-2.34109123	-1.560984705	2023/05/06 11:00:11+00
6.1C	S. Alveolata	47.2549197	-2.3418324	Unknown	2023/05/06 11:34:00+00
8.1	S. Alveolata	47.25496092	-2.34128994	0.619808374	2023/05/08 13:02:26+00
L. Conchilega	L. Conchilega	47.25513087	-2.34092751	1.170152522	2023/05/08 13:21:18+00
Haploops Nirae	Haploops Nirae	47.34141766	-2.55221927	6.906228151	2023/05/08 08:50:44+00

Table A.1.1: Table with the sampling location visited during the fieldwork.

A.2 Tidal information for the fieldwork location and period

Date	Tidal Coefficient	High tide (m)	Low tide (m)
04/05/2023	79	5.5	1.0
05/05/2023	86	5.6	1.0
06/05/2023	91	5.8	0.8
07/05/2023	94	5.7	0.9
08/05/2023	91	5.6	1.0

Table A.2.1: Tidal coefficients and high and low tides at Pornichet for the field work days. Tide levels are in reference to Mean Lower Low Water (MLLW). Data retrieved from "Tide times and charts for Pornichet, Pays-de-la-Loire and weather forecast for fishing in Pornichet in 2023" (n.d.).

A.3 Sampling procedures

For the different species collected during the fieldwork, different procedures and equipment were necessary. As such, two different procedures will be outlined in the next sections.

Sampling S. Alveolata

Firstly, it should be noted that not all species were collected in equal amounts. Specifically, S. Alveolata was much easier to both find and sample as it was not living on the sea bottom. It should also be noted again that all samples were collected during spring tide, giving much more opportunities to sample with the lower tide. The tools used in sampling these bioconstructions are:

1. Geologic hammer
2. Jointing knife
3. Tape measure
4. Camera or camera equipped phone
5. GPS or GPS equipped phone
6. Buckets with lid
7. Sampling tubes with lids and a hammer that fits the tubes.

Generally speaking, before making any sampling attempt, locations are to be recorded and necessary photographs taken, using a tape measure for scale. Then, pieces of interest must be selected for sampling, and a plan made on how to reach these. This is because storage buckets, especially with lids, are limited in size. Pieces can then be dislodged using the jointing knife. Where constructions are too strong, the hammer can be used to deliver a few blows to the jointing knife to help dislodge pieces. Samples are then carefully handled and packed in plastic bags. After this, they are stored in buckets with several pieces in one bucket. Buckets were then stored in the vehicle for the duration of the fieldwork, before being delivered to the cold sample storage room at the TU Delft. Similarly, a few sample tubes were filled as well by hammering them into the reefs, closing them using lids and then transporting them to the TU Delft. Some variants on this procedure are possible, such as storage in sea water instead of dry in bags.

Sampling H. Nirae

In order to sample H. Nirae from the seabed, some equipment is needed. However, apart from the listed equipment, it is necessary to have a boat with gps equipment to find the correct location. In this fieldwork, a local fisherman was found that knew the location where H. Nirae lived and that was willing to ferry the team to and from that location. The necessary equipment for sampling this species is as follows:

1. Van Veen grab sampler
2. Plastic tray
3. Tape measure
4. Camera or camera equipped phone
5. Buckets with lid

The procedure for sampling H. Nirae from the sea bottom is quite straightforward. Using the Van Veen sampler, chunks of sediment are sampled from the sea bottom and pulled onboard the vessel. Once on board, the sampler is opened into the plastic tray so the material can be inspected. The tray can then be photographed with the sample, using a tape measure as scale. After this, the samples are deposited in buckets, topped of with sea water and driven to the cold sample storage at the TU Delft. Samples were put together in the buckets and are thus disturbed.

Appendix B

Procedure for disintegration of S. Alveolata bioreefs.

B.1 Chemicals and equipment list

The following chemicals were used for the disintegration of S. Alveolata bioconstructions:

- 30% hydrogen peroxide (H_2O_2) (Sigma-Aldrich) diluted to 6% using demineralized water.
- Demineralized water
- Ethanol as a safety measure.

As well as the following lab equipment:

- Scalpel
- Scales
- Dessicator
- Sample storage containers with lid
- Whatman N°50 filter paper
- Hot plate
- Buchner funnel,
- Glass stirring rod
- 25 mL volumetric flask
- 150 mL conical flasks
- Cover glass to fit the conical flasks
- Evaporating dish, 150 mm
- Oven

B.2 Disintegration Procedure

This procedure is designed to disintegrate small pieces of S. Alveolata bioreefs. Generally, this procedure is suitable for single pieces and small clusters, with weights of about 5 grams or less. This procedure is based on organic material oxidation procedures as outlined in BS 1377-2 (1990), Parker (1983) and Reeuwijk (2002).

1. Select samples which have little attached plants or other organic matter. Cut the samples to size using a scalpel.
2. Remove any and all visible plant growth and animal remains. Air out the sample if necessary. Wash with fresh water to remove excess and loose grains.

3. Select, label and weigh all materials before starting.
4. Measure and note the inner diameter of the tube.
5. Dry out the samples overnight in a 65 degree oven and let cool in a desiccator.
6. Place the sample in a conical beaker and weigh the combination.
7. Add about 20 mL of distilled water and gently boil to reduce the volume slightly, by about 10%, stir regularly. Let cool.
8. After cooling, add 25 mL of the 6% hydrogen peroxide and stir the mixture gently with the glass rod. Make sure that the sample is completely covered, otherwise add more peroxide until covered. Cover with a cover glass and allow to stand overnight.
9. Gently heat the mixture in the conical flask, taking care to avoid frothing over. Stir or agitate the contents frequently.
10. As soon as vigorous frothing has subsided, reduce the volume to about 20 mL by boiling. With very large amounts of organic material additional peroxide may be required to complete the oxidation.
11. Transfer the mixture including the mineral grains to an evaporating dish.
12. Put the evaporating dish into a 105 °C oven for about 4 hours until completely dry. From here the samples can be used in the XRD procedure.
13. If necessary, transfer the now dried particles to storage container, using a jet of water and put the lid on. They are now ready for use in laser diffraction.

Appendix C

Structural Investigation Methods

This appendix will outline the methods used in the different steps towards the structural analysis of the reefs. In total, five different research methods were used to piece together information on the structure of the reefs.

C.1 Digital Microscopy

In order to investigate the structure of S. Alveolata bioreefs and the H. Nirae biotubes use was made of a Keyence VHX-7000 digital microscope system (Keyence International, 2023) equipped with their VHX-7100 fully integrated head. Three different lenses were used mainly, the VHX-E100, VHX-E20 and VHX-E500 high-resolution lenses. Samples were cut from larger blocks and then inserted into the microscope for examination. Images were then processed using the accompanying Keyence software.

Microscopy type		Optical	
Sample location	Number of single tubes	Number of clusters	Number of photos
H. Nirae	8	0	33
4.1	7	0	7
5.3	16	3	51
6.1A	4	5	45

Table C.1.1: Table with the amount of samples produced and the number of images taken per fieldwork location as used in optical microscopy investigation. This includes images taken of samples previously used for E-SEM work.

C.2 E-SEM

In order to investigate the microstructure of S. Alveolata bioreefs, Environmental Scanning Electron Microscope (E-SEM) was used. In this case an FEI Quanta 650 FEG was used, coupled with an EDS system made by Thermo Fisher Scientific for point and image spectral analysis.

Microscopy type		SEM	
Sample location	Number of tubes	Number of SEM pictures	Number of optical photos
4.1	1	18	12
5.1	7	27	19
6.1A	4	30	36

Table C.2.1: Amount of samples produced and the number of images taken per fieldwork location as used in E-SEM.

Subject description	Location	Acquisition time	Voltage (kV)	Power (W)	Voxel size (µm)	Exposure (ms)	Projections
Small, complete reef block	6.1C	00:02:18	150	125	125	35	1440
More detailed scan of the attachment area to the substrate	6.1C	01:11:49	150	30	30	2750	1440
Small sample for initial porosity analysis	5.3	01:12:23	150	30	30	2750	1440
Small sample for detailed porosity analysis	6.1C	01:26:54	120	15	10	1700	2879

Table C.3.1: Parameters used in producing the different CT-datasets.

C.3 CT-scanning

For CT-scanning use was made of a CoreTOM micro-CT scanner, built by TESCAN (TESCAN, n.d.). In total, 5 different image sets were produced for use during these experiments. These scans the parameters used are listed in table C.3.1.

C.4 Laser diffractometry for grain sizes

To analyze the grain size distribution of the different samples, use was made of a Malvern Mastersizer 2000 as provided by Deltares. For this machine the maximum grain size is 3 mm (3000 μm).

In this case, three different single tubes were dissected into three roughly equal size pieces, keeping track of the original tube orientation. As such, 9 samples were produced, 3 top, 3 middle and 3 bottom sections of a tube. These 9 tube section were then treated as outlined section B, producing 9 samples consisting of loose grains.

The loose grains are then transferred to a large beaker with water which is placed in the Mastersizer for measurements. A photograph of the setup is present in section C.4.1. The results are automatically outputted to a CSV file which is then analyzed using Python and Excel.

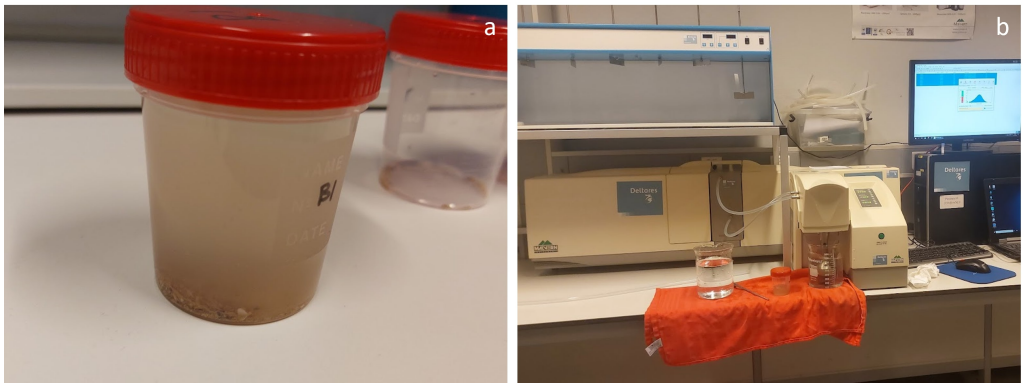

Figure C.4.1: Figure with a) one of the samples (B1) analyzed in laser diffraction and b) the MasterSizer 2000 setup used during the analysis.

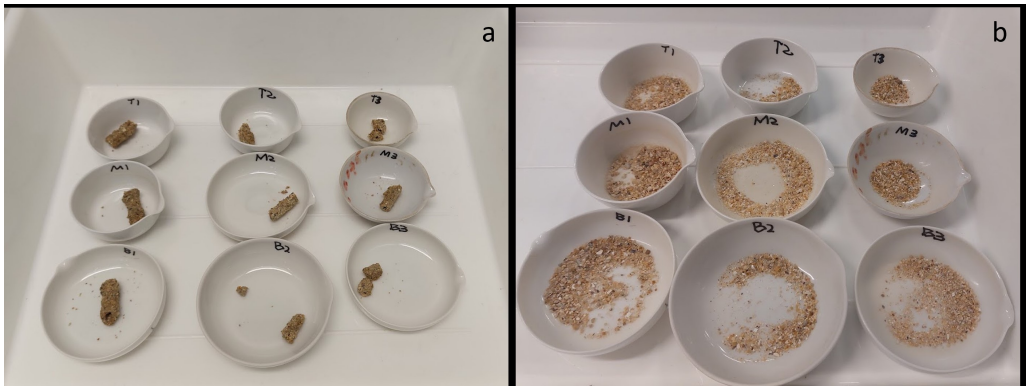

Figure C.4.2: The tube parts analyzed for particle size distribution a) before and b) after the breakdown of organic material. For size reference, the largest ceramic dish is approximately 10 cm in diameter, and most samples are about 2 cm in length.

The resulting particle size distributions can be found in figures C.4.3 (tube 1), C.4.4 (tube 2) and C.4.5 (tube 3). They include all data from the different runs per sample.

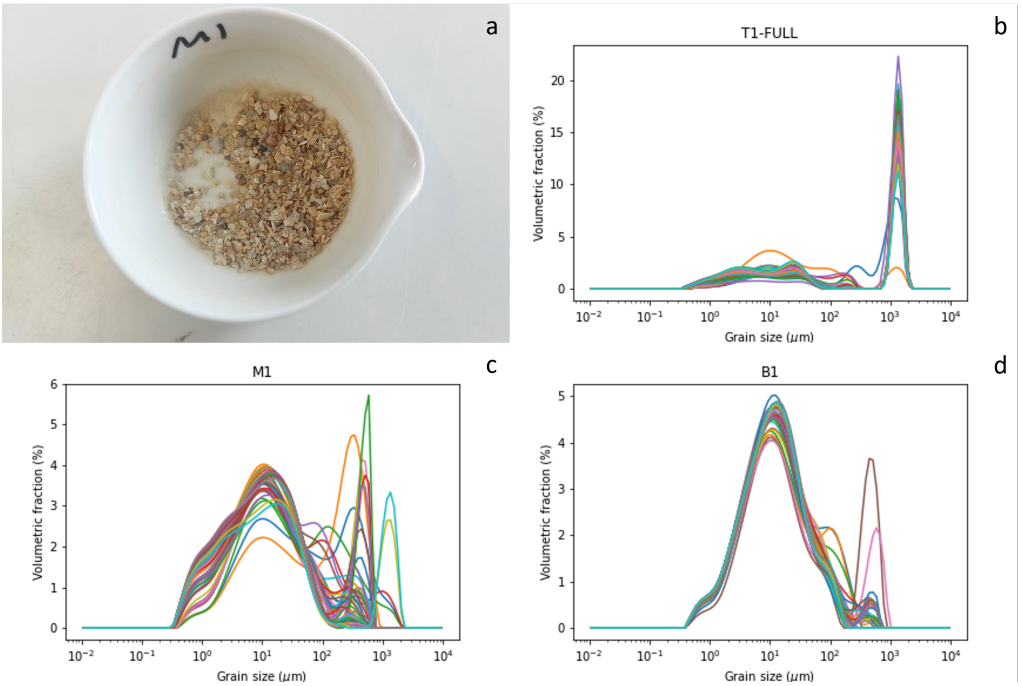

Figure C.4.3: Photo (a) and particle size distributions for sample 1, from b) the top (T), c) the middle (M) and d) the bottom (B). The dish in a) is approximately 5 cm in diameter.

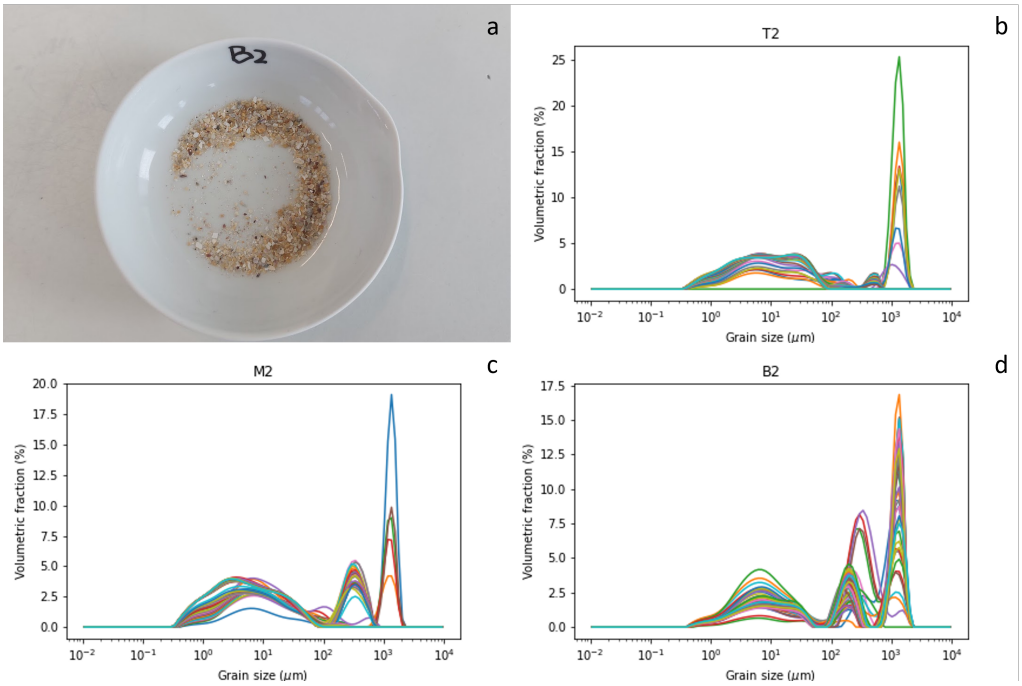

Figure C.4.4: Photo (a) and particle size distributions for sample 2, from b) the top (T), c) the middle (M) and d) the bottom (B). The dish in a) is approximately 10 cm in diameter.

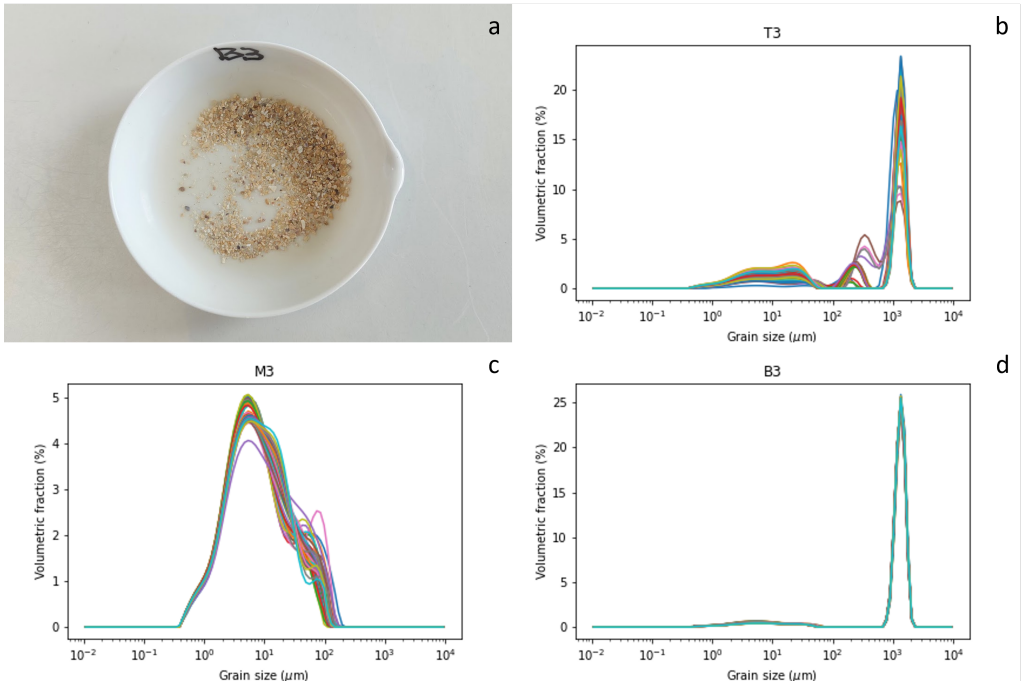

Figure C.4.5: Photo (a) and particle size distributions for sample 3, from b) the top (T), c) the middle (M) and d) the bottom (B). The dish in a) is approximately 10 cm in diameter.

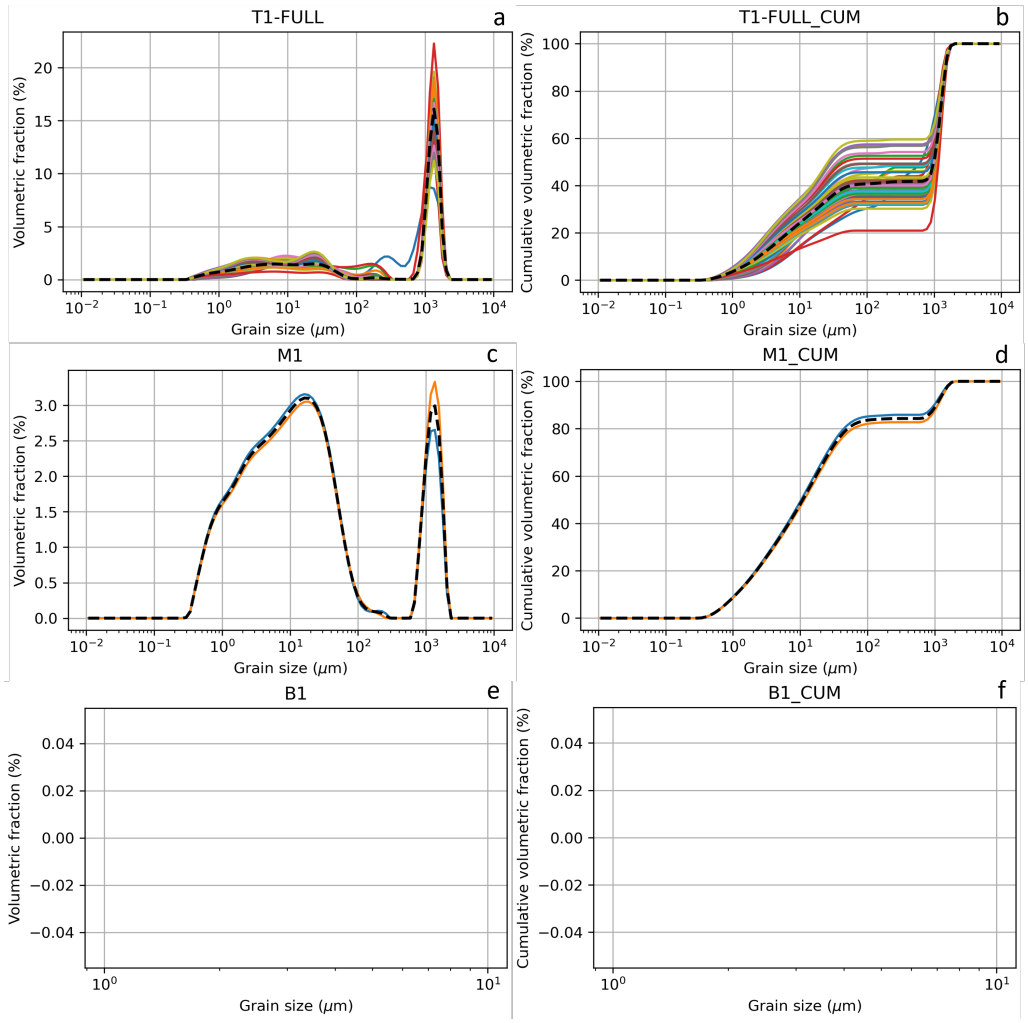

Figure C.4.6: Particle size distributions and cumulative distributions of all the different parts of single tube 1. Each line in represents a single measurement runwhere the d90 ¿ 900µm. Empty figures signify no run had correct data. The black dotted line is the average of all included measurement runs.

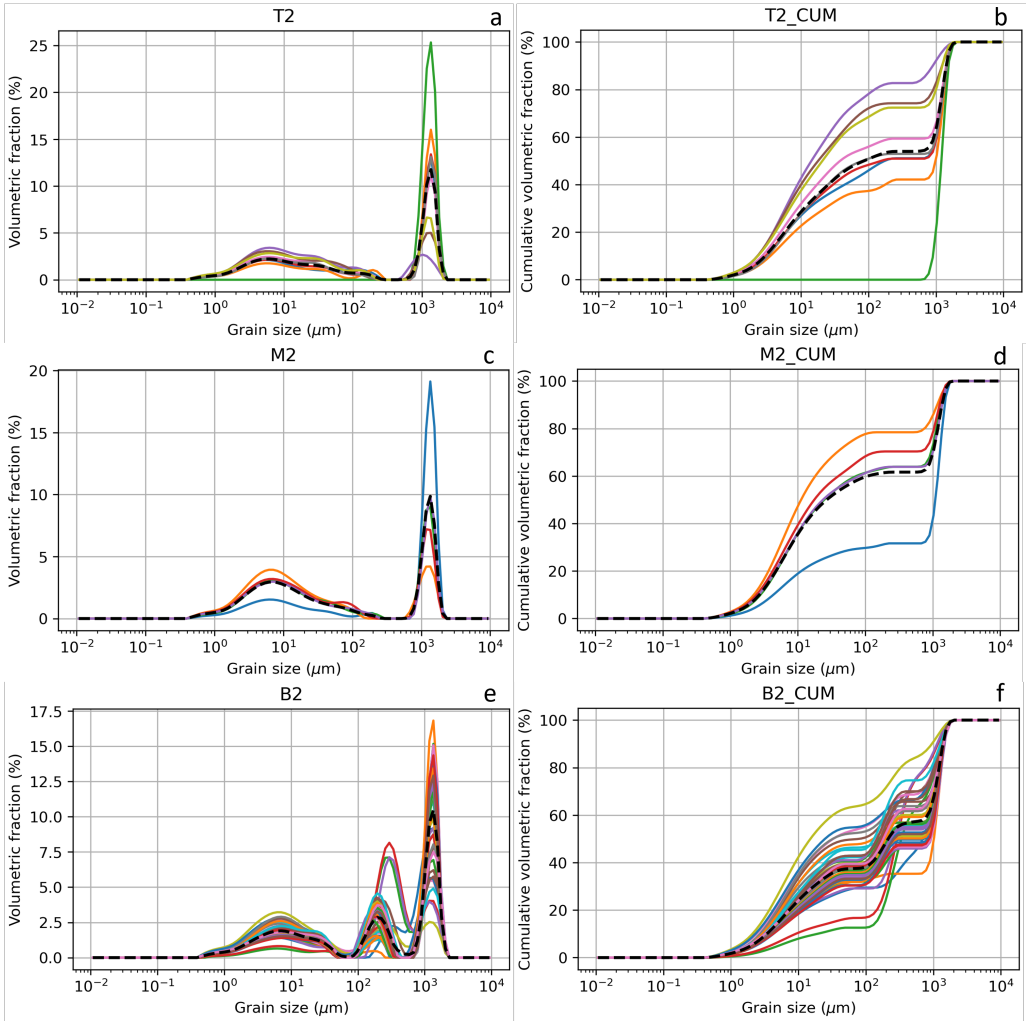

Figure C.4.7: Particle size distributions and cumulative distributions of all the different parts of single tube 2. Each line in represents a single measurement runwhere the d90 ¿ 900µm. Empty figures signify no run had correct data. The black dotted line is the average of all included measurement runs.

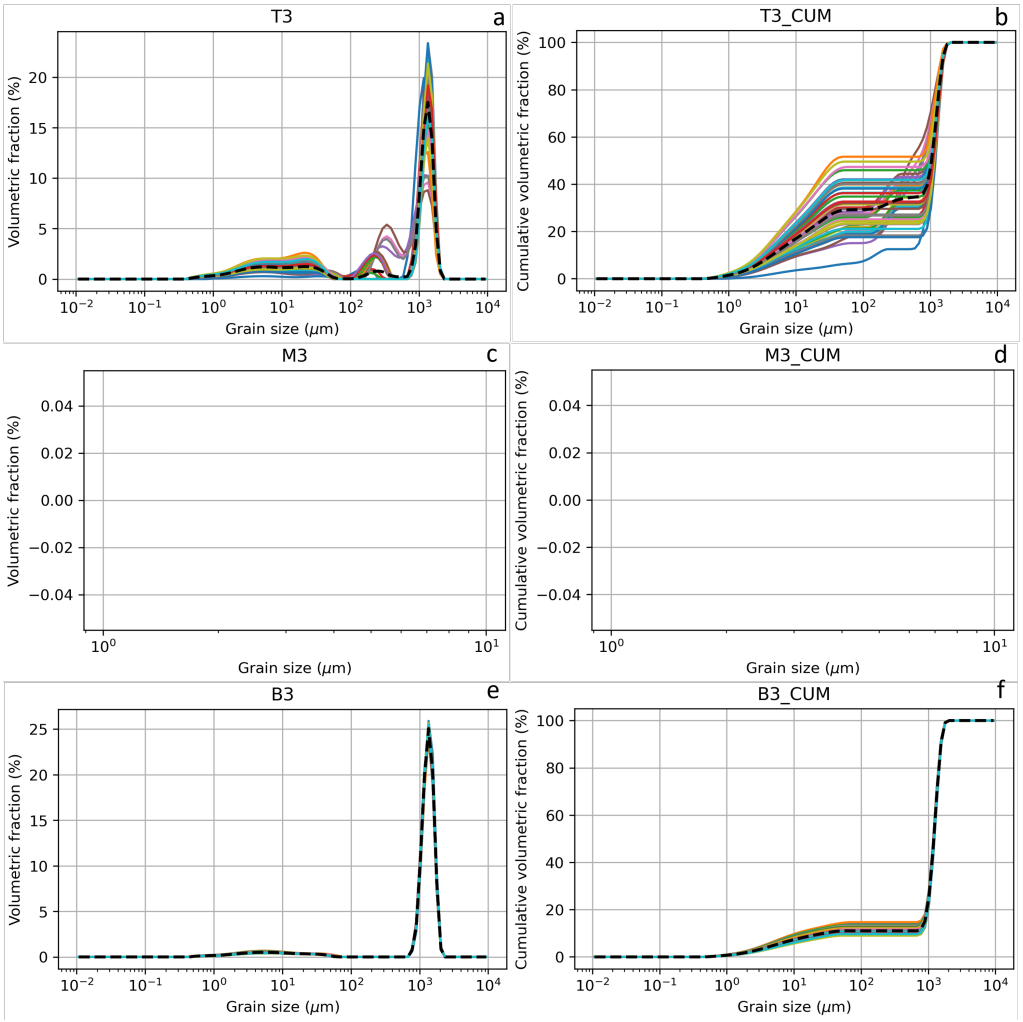

Figure C.4.8: Particle size distributions and cumulative distributions of all the different parts of single tube 3. Each line in represents a single measurement runwhere the d90 ¿ 900µm. Empty figures signify no run had correct data. The black dotted line is the average of all included measurement runs.

C.5 Powder X-Ray Diffraction

For Powder X-Ray Diffraction, use was made of a Bruker D8 series P-XRD machine. In order to prepare samples for P-XRD analysis, tube fragments from locations 5.1 and 6.1B were disaggregated into loose grains. This was done as outlined in section B. The samples used are shown in figure 3.5.1. These loose grains were then hand-crushed using a mortar and pestle. At the same time, sand collected from close by the reefs at these location was also crushed and analyzed using the P-XRD equipment.

C.6 Glue Spot analysis

Samples from These were disaggregated into loose grains by hand using tweezers to mostly pick loose single grains and or using abrasion from the tip of the tools. In this case care was taken to not destroy the grains and to catch all the grains in a 10 cm plastic petri dish. The grains were then left to dry for several days until glue spots had discoloured and could as such be easily distuingished under a microscope. For the glue spot analysis use was made of the Keyence microscope already described in section C.1. This was used to take pictures of the loose grains section by section. This resulted in 51 images of sample 5.3 and 41 images of sample 6.1A. From the 51 pictures from sample 5.3, in total 133 grains were studied and on those grains 663 glue spots were found. From the 41 pictures from sample 6.1A, in total 109 grains were studied and on those grains 538 glue spots were found. Size measurements were taken of 492 glue spots for sample 5.3 and of 459 glue

spots for sample 6.1C. It should be noted that two different analyses were done, one on the sizes of the glue spots and one on the amount of spots per grain. For the sizes of the glue spots all spots visible were taken into account.

The length of the glue spots is measured along their longest axis using the Keyence VHX-7000 software. For circular spots, the diameter is measured using a different tool, so that the shapes can be separated during processing. Figure C.6.1 shows the difference between measurement modes.

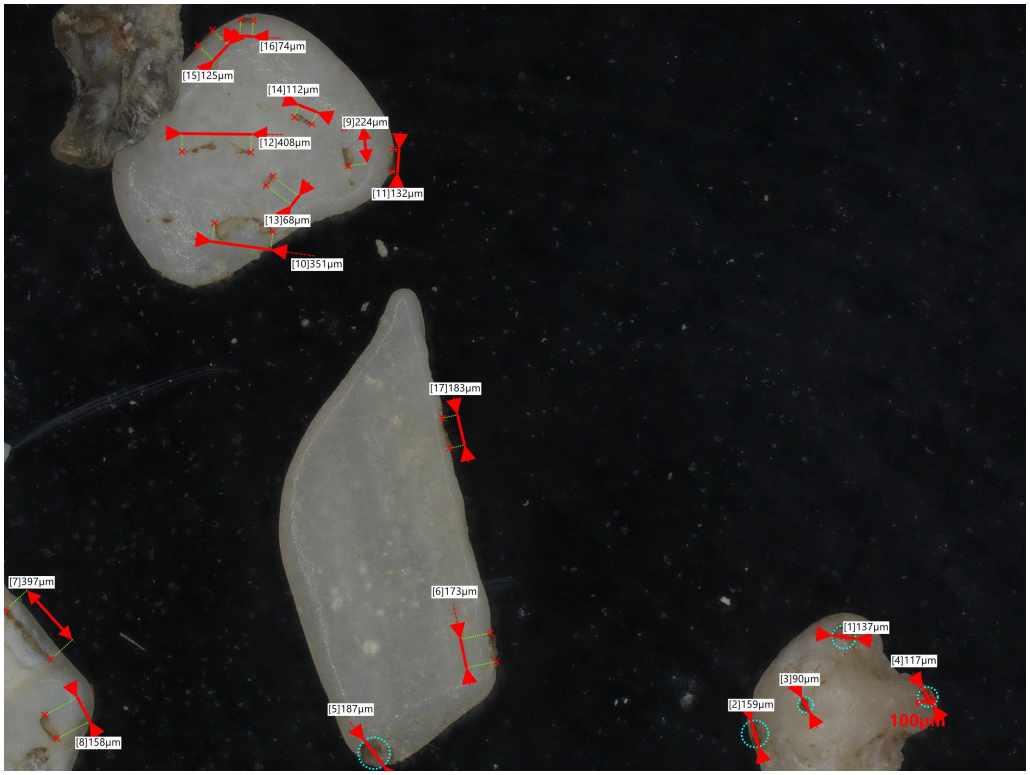

Figure C.6.1: Photo used for the analysis of the glue spots. Note the difference in measurement mode when comparing measurements number 5 and 16/17. The difference in measurement mode allows to distuingish these differences in the analysis. The left bottom corner shows a glue spot of which the size could not be determined, and which is not included in the size analysis.

Appendix D

Image Processing and Analysis

This appendix will shortly highlight the different steps taken to process the images acquired by CT-scanning. There are two different workflows. One to just visualize the tubes, another for visualizing and analyzing the porosity volume fraction.

D.1 Visualizing the tubes

The goal for this analysis is to visualize the tubes inside the sample. A schematic of this workflow is given in figure D.1.1.

The workflow is as follows:

- The datafile is loaded into avizo.
- A filter sandbox and interactive thresholding module are used to filter the structure of the sample. This leaves behind the porosity and gives a binary of the grains and solid matter in the sample.
- Since the goals is to visualize the tube the following modules are used to close all holes the porosity leaves in the structure binary image: majority filter, remove small spots, closing by reconstruction, fill holes.
- This is then masked onto the original data giving the outline of the samples.
- This is then thresholded to give the solid portion inside the sample as a binary.
- The compute ambient occlusion module is used to compute the ambient occlusion.
- The result from this is again masked with the outline to leave only the porosity inside the sample.
- This is then eroded and despeckled to close the smallest holes.
- This image is then thresholded to create a binary image of the internal porosity.
- The remove small spots is used to remove small artefacts.
- A label analysis is used to filter the porosity on size so that the smallest porosity is filtered out before visualizing using the Volume rendering module. A secondary label analysis is attached on elongation of the porosity to try to get a better view.

D.2 Porosity volume fraction analysis

This routine is based on the routine as outlined by Wantha (2021). As such, only the difference with this routine will be discussed here. The routine used in this study is outlined in figure D.2.1.

The routine used for this thesis is as follows:

- Interactive thresholding is used to isolate the structure and sand grains and binarize the image.

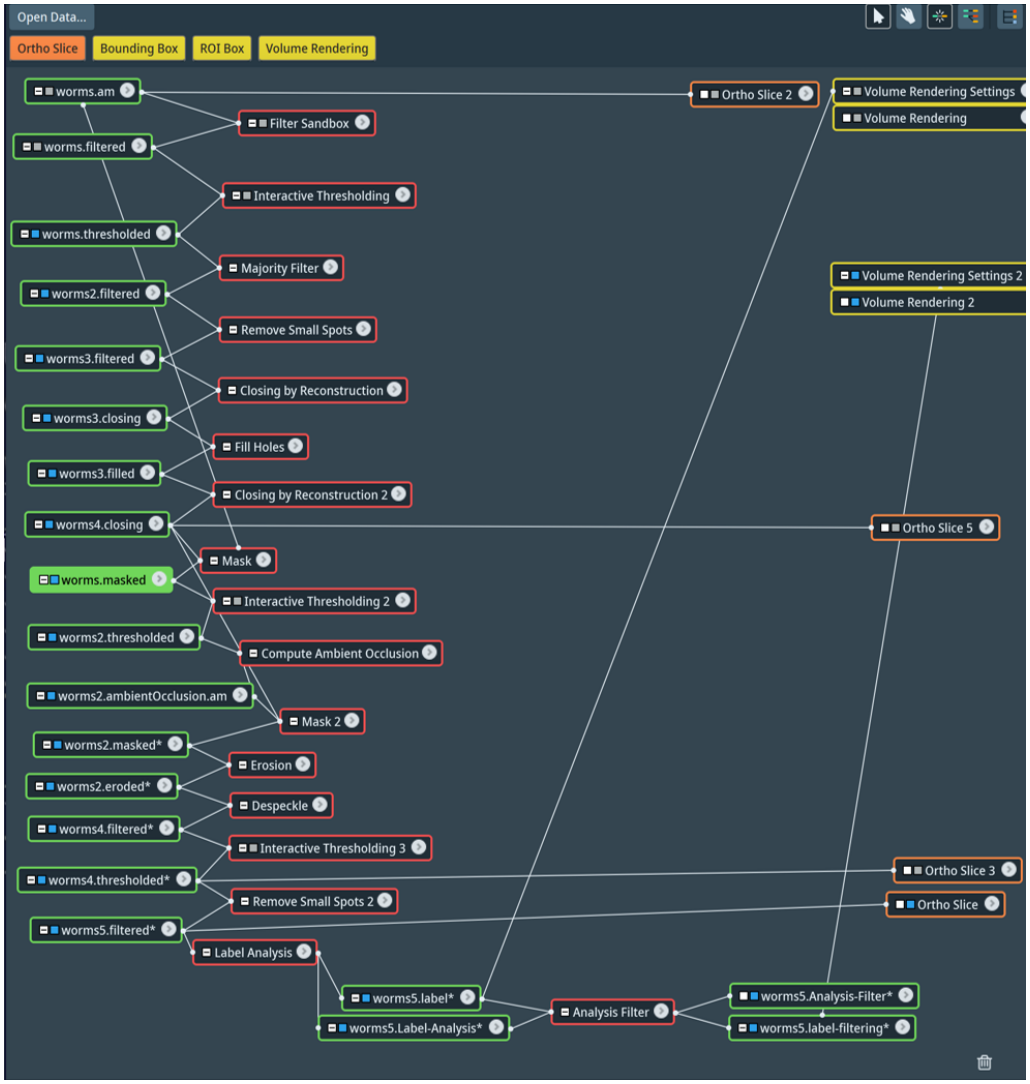

Figure D.1.1: The workflow for analyzing the porosity volume fraction.

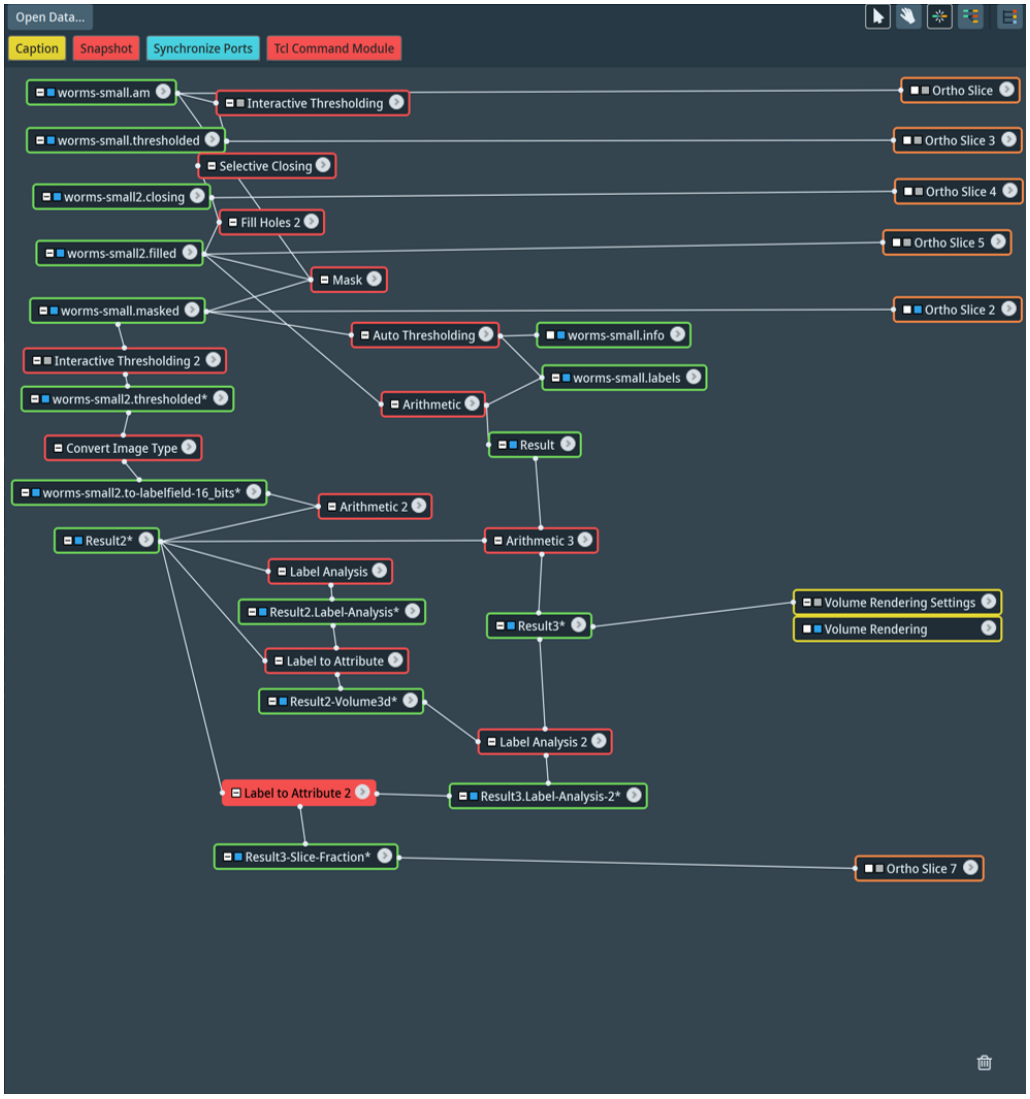

Figure D.2.1: The workflow for analyzing the tubes as they are running through the reefs.

- Selctive closing and fill holes modules are used to transform the binary image into the outline of the sample.
- This binary images is masked with the original data to remove any artefacts outside of the sample which can distort the results.
- From this masked image, the solid parts inside the sample are binarized using the auto thresholding module. This is then subtracted from the sample outline binarization to get a binary image of the porosity fraction.
- The total volume is selected from the masked image using the second interactive thresholding module and converted to a binary image.
- This is converted to a 16-bit label image using the convert image type module.
- This 16-bit image is then multiplied with an index k to calculate the volume per z-slice. (result2 in figure D.2.1)
- A label analysis is used to het the total volume per Z-slice. The label to attribute module is used to display this volume per z-slice.
- The result2 from before is then multiplied with the label analysis to link the porosity to its position in the z-axis.
- A label analysis (label analysis 2) is then used to calculate the porosity fraction per z-slice by using the formula: (100/Maximum)*Volume3d.

Appendix E

Mechanical and durability testing methods

This appendix will give extra information on mechanical and durability testing. Here, the exact procedures used during mechanical testing are outlined and at the same time more detailed results, sample photos and more are presented.

E.1 Slake durability testing

Two different slake durability experiments were performed during the testing phase of this study. Their procedures are outlined below and extra photos taken during sample preparation and testing can be found here.

E.1.1 Slake durability testing on blocks

The slake durability testing procedure on blocks is based on the ISRM procedure as outlined in Ulusay and Hudson (2007). The exact procedures are as follows:

1. A sample of ten reef lumps is cut from the bigger blocks, each with a mass of 40-60 g, to give a total sample mass of 450-550 g.
2. The sample is placed in a clean drum and is dried to constant mass at a temperature of 105 °C in 2 hours in the oven. The mass A of the drum plus sample is recorded. The sample is then tested after cooling.
3. The lid is placed, the drum mounted in the trough and coupled to the motor.
4. The trough is filled with slaking fluid, here tap water at room temperature, to a level 20 mm below the drum axis, and the drum rotated for 200 revolutions during a period of 10 min to an accuracy of 0.5min.
5. The drum is removed from the trough, the lid removed from the drum, and the drum plus retained portion of the sample dried to constant mass at 105 °C for 2 hours. The mass B of the drum plus retained portion of the sample is recorded after cooling.
6. Steps 3-5 are repeated and the mass C of the drum plus retained portion of the sample is recorded.
7. The drum is brushed clean and its mass D is recorded.

After these steps the slaking indices (after cycle 1: I_{d1} and I_{d2} after cycle) can be calculated as follows:

$$I_{d1} = \frac{B - D}{A - D} \times 100\%$$

$$I_{d2} = \frac{C - D}{A - D} \times 100\%$$

Sample preparation for these experiments is simple, blocks are cut from larger blocks collected during field work. These are then weighed and cut back to get the right weights if necessary. After cutting, the blocks are quickly rinsed with water to remove any grains that were not attached. A photo of this is displayed in figure E.1.1. They are then dried and the procedure previously outlined is followed. Also, figures E.1.2-E.1.4 show the progression of each sample during testing, with photos taken before testing and after each cycle.

Figure E.1.1: Photo detailing the sample preparation for slake durability testing. Shown is a larger reef block from which smaller blocks are cut and the water bottle with which the blocks are rinsed.

E.1.2 Slake durability testing on single tube batches

A second variant of the slake durability testing has also been performed. In this case reef blocks were abraded and separated in to single tube fragments. These were then collected and separated into different length classes. The procedure is also outlined by figure E.1.5. The exact procedure is as follows step-by-step:

1. A reef block from location 8.1 was selected and cut into smaller pieces. The pieces were then rinsed quickly with water to get rid of any loose grains and pieces.
2. The tube pieces were then dried overnight at 65 °C to get rid of any moisture.
3. The tube pieces are then sorted according to length and divided into three equal sample runs. The length classes used are as follows: less than 1.5 cm length, 1.5 to 2 cm length, 2-2.5 cm length and larger than 2.5 cm. As such every run consists of an equal number of tubes in every class. The classes are then put in a container and weighed.
4. The tubes are loaded into a drum and the container is weighed.
5. The drum is mounted into the apparatus and the trough is filled to the specified level (20 mm below the drum axis) with water. The machine is turned on and left on for 5 minutes/100 rotations.
6. The appropriate amount of containers is then weighed and prepared for the samples. One container will contain the tubes from one class.
7. The drum is then emptied, the tubes are sorted into the classes specified in step 3 and counted. The tubes are then dried in a 65 °C oven overnight.
8. The tubes are then weighed per class, and the weight of tubes is computed by subtracting the weight of the containers.

The results from this procedure are then processed further. For each class an average length can be estimated as about halfway between the maximum and minimum values. From there the total tube length can be estimated before and after the experiment. Also, the weight per cm of tube length before and after the experiment can be estimated. These are given in table E.1.1. From

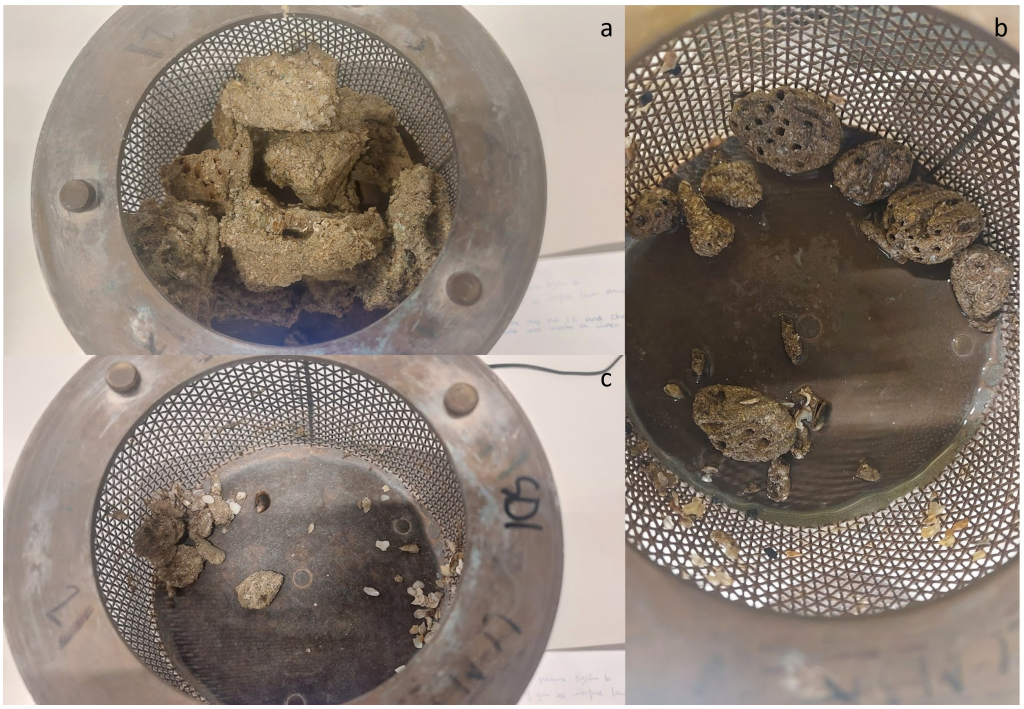

Figure E.1.2: Photos from the slake durability testing of sample 1 from location 4.1. a) shows the samples before testing, b) shows what is left of the sample after one cycle in the slake durability machine. c) shows the sample after two cycle of testing.

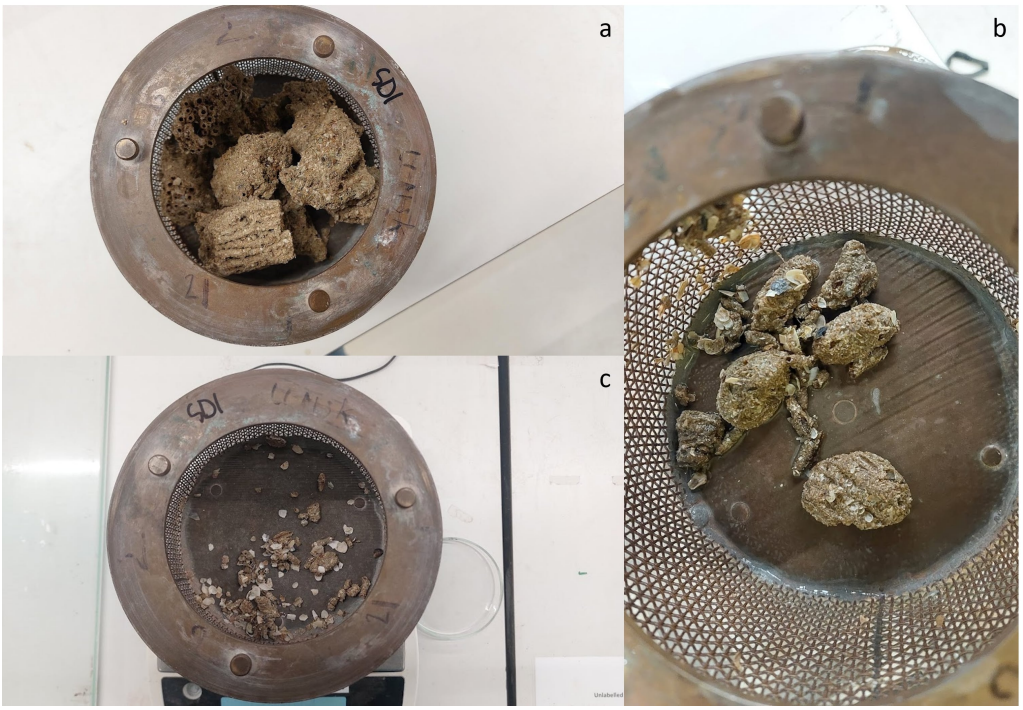

Figure E.1.3: Photos from the slake durability testing of sample 2 from location 4.1. a) shows the samples before testing, b) shows what is left of the sample after one cycle in the slake durability machine. c) shows the sample after two cycle of testing.

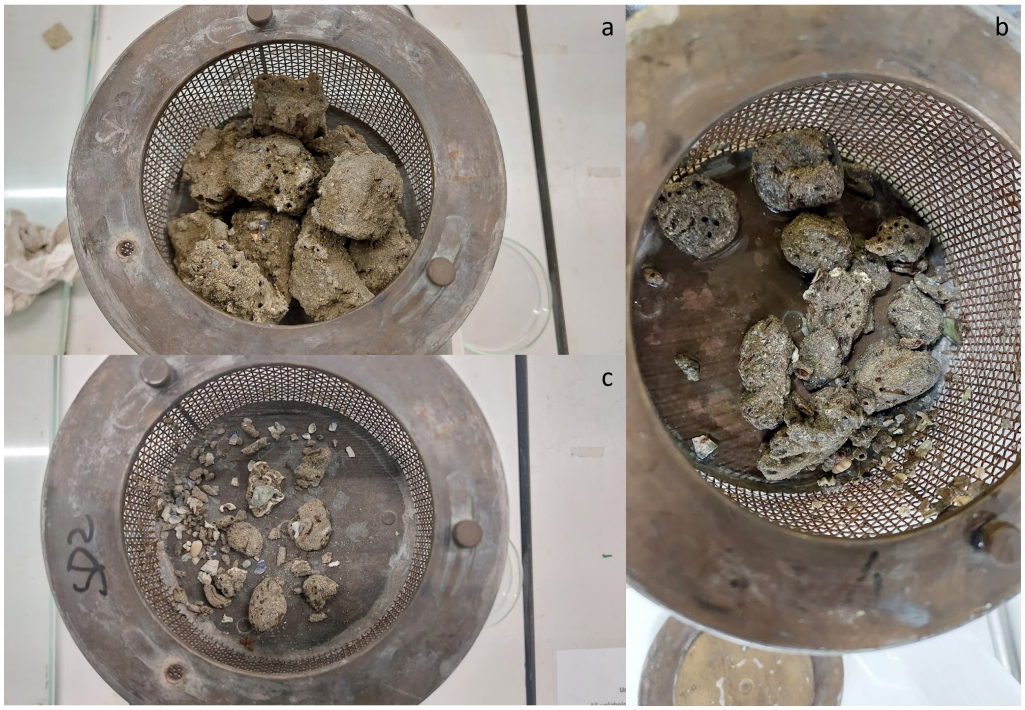

Figure E.1.4: Photos from the slake durability testing of sample 3 from location 5.2. a) shows the samples before testing, b) shows what is left of the sample after one cycle in the slake durability machine. c) shows the sample after two cycle of testing.

Figure E.1.5: Photos from the sample preparation and testing of single tubes using slake durability equipment. a) shows the procedure of dissecting the blocks into single tube parts. b) shows the sizing of the parts into their different classes. c) shows the three sample sets with each row a different sample set while the columns are the classes. d) shows the results after drying and testing.

	Average length per class (cm)	Total length before (cm)	Total length after (cm)	Percentage change	Weight per cm before (g/cm)	Weight per cm after (g/cm)	Percentage change
Run 1	1.25	17.50	31.25	79%	0.33	0.14	-56%
	1.75	26.25	26.25	0%	0.34	0.21	-39%
	2.25	29.25	20.25	-31%	0.36	0.23	-36%
	2.75	33.00	5.50	-83%	0.39	0.29	-27%
Run 2	1.25	17.50	27.50	57%	0.32	0.17	-47%
	1.75	26.25	29.75	13%	0.34	0.18	-46%
	2.25	29.25	15.75	-46%	0.34	0.26	-25%
	2.75	33.00	2.75	-92%	0.36	0.17	-54%
Run 3	1.25	17.50	30.00	71%	0.30	0.15	-51%
	1.75	26.25	28.00	7%	0.30	0.19	-35%
	2.25	29.25	20.25	-31%	0.33	0.20	-40%
	2.75	33.00	8.25	-75%	0.32	0.18	-45%

Table E.1.1: Table with the total length per class and the weight per length unit as well as the changes after the experiment.

Total Length	Before (cm)	After (cm)	% Change	Weight/cm	Before (g/cm)	After (g/cm)	% Change
Run 1	106.00	83.25	-21%	Run 1	0.36	0.19	-46%
Run 2	106.00	75.75	-29%	Run 2	0.34	0.19	-44%
Run 3	106.00	86.50	-18%	Run 3	0.32	0.18	-44%
Average	106.00	81.83	-23%		0.34	0.19	-45%

Table E.1.2: Table with the total length of reef tube per run and the weights per length for tubes as well as the averages over the three runs.

that table for every run and an overall reduction in tube length and weight is computed, these are displayed in table E.1.2.

E.2 Oedometer testing

This section will provide a more complete overview of the oedometer testing and sample preparation overview procedure. Also, tables are present with per-step results for each loading step. The testing scheme here is based on what is outlined by Head and Epps (2011).

E.2.1 Oedometer testing equipment

The oedometer apparatus applies a static load to a sample which is constrained by a ring. A schematic for the apparatus is present in figure E.2.1. The sample holder consists of a confining ring with a sharp edge which is placed on a porous stone to allow for water flow through the stone.

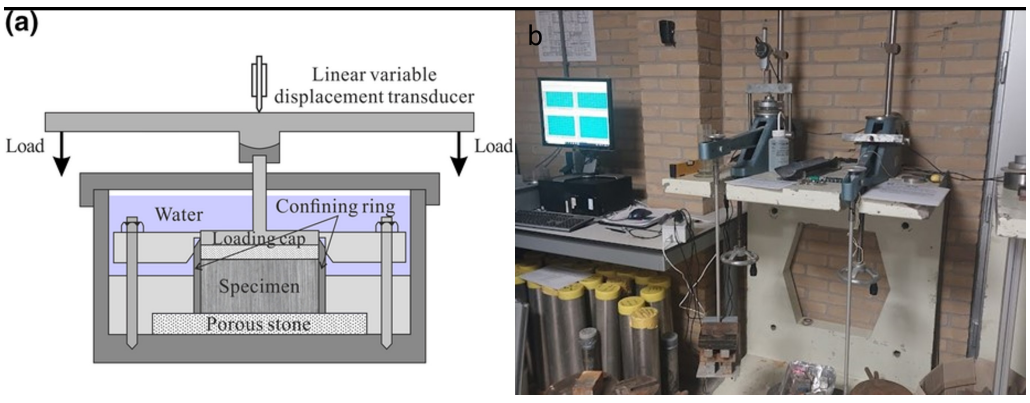

Figure E.2.1: Schematic of the oedometer workings (a) as made by Zhang et al. (2021) and the oedometer setup at the TU Delft laboratory (b).

The stone and confining ring with sample are set in a small basin. The confining ring is held in place by a cap which is secured to the basin by screws or gravity. A loading cap with a porous stone is placed on top, sealing the sample in the confining ring while allowing for water flow. Through a large bracket, an arm on which weights are placed is connected to the loading cap in such a way that the load from the arm is transferred through the loading cap to the sample. The vertical displacement of the sample as a result of the load is measured using a linear displacement sensor.

E.2.2 Oedometer testing procedure

	T1	T2	T3	Beach Sand	
Sample height, H1	19.0	19.0	19.0	20.00	(mm)
Sample diameter, D	50.0	50.0	50.0	50.00	(mm)
Sample wet weight, m_b	47.5	60.1	58.0	74.97	(g)
Sample dry weight, m_d	36.5	46.3	45.8	59.53	(g)
Assumed particle density, rho_p	2.67	2.67	2.67	2.67	(g/cm3)
Height after test, H2	15.0	17.2	16.4	19.67	(mm)
Wet density, rho_w	1.27	1.61	1.56	1.91	(g/cm3)
Dry density before, rho_d1	0.980	1.24	1.23	1.52	(g/cm3)
Dry density after, rho_d2	1.24	1.37	1.43	1.54	(g/cm3)

Table E.2.1: Table with the oedometer test data.

The procedure for sample preparation for oedometer testing of the reef blocks is as follows:

1. A large enough reef block must be selected, from which smaller samples can easily be cut.
2. The confining ring is pushed into the sample in such a way that the tubes inside the sample are as much perpendicular to the ring as possible so that the load will be applied along the tube direction.
3. Using a jointing knife, the bottom and top of the sample will be cut flush with the ring.
4. Any small or large holes left after cutting are filled as much as possible with sand leftover from cutting the sample.
5. The confining ring with the sample is then placed on the porous stone and put in the oedometer setup.
6. The top cap and displacement sensor are placed and measurement is started.
7. The sample is the flooded with demineralised water.
8. After 15 minutes the first load of 1 kg is then placed. Every 15 after this, weight is added or removed until the experiment is complete. The exact load steps are outlined in the tables E.2.2-E.2.5 for the respective samples.
9. When all weight is removed, the measurements are continued for 15 minutes after which measurements are stopped and the setup is disassembled and cleaned.
10. The sample is put insight a container of known mass and weighed.
11. The sample is dried overnight at 105 °C.
12. The sample and container are weighed, the weights are recorded and the data is processed.

For the beach sand tested, step 1-4 are different. For the beach sand, they are as follows:

1. The confining ring is placed on the porous stone.
2. Sand is fed into the ring using a spoon and small funnel in such a way that the sand is carefully placed layer by layer inside the ring. Sand is compacted by tapping and shaking the mold between layers placed.
3. The top of the sample is leveled using a jointing knife and the sample placed in the oedometer apparatus.
4. Testing is then as above from step 6 onwards.

E.2.3 Additional results

In this section, the test data after each load step is presented in tables E.2.2-E.2.5. In tables E.2.6-E.2.9 the consolidation parameters for each load step can be found for all the different samples. Also, in figure E.2.2 sample photographs are presented from before and after oedometer testing.

Figure E.2.2: Upper surfaces of the samples for oedometer testing before and after testing.

Loads and deformations, Test T1												
Load	Load	Total weight	Stress	dinc	dtotal	Final Thickness	Incremental Strain	Total strain	V	e	v	w
Step	(kg)	N	(kPa)	(mm)	(mm)	(mm)	(-)	(-)	(cm3)	(-)	(-)	(%)
0	0	0	0.0	0.00	0.00	19.00	0.000	0	37.3	1.72	2.72	64.61
1	0.37	3.6297	1.9	-0.0020	0.00	19.00	0.000	0.000	37.3	1.72	2.72	64.62
2	1	98.1	51.9	0.4080	0.41	18.59	0.021	0.021	36.5	1.67	2.67	62.43
3	2	196.2	101.9	0.4970	0.90	18.10	0.027	0.048	35.5	1.60	2.60	59.76
4	3	294.3	151.9	1.4120	2.32	16.69	0.078	0.122	32.7	1.39	2.39	52.17
5	4	392.4	201.9	0.5150	2.83	16.17	0.031	0.149	31.7	1.32	2.32	49.41
6	5	490.5	251.9	0.3260	3.16	15.84	0.020	0.166	31.1	1.27	2.27	47.66
7	6	588.6	301.9	0.2680	3.42	15.58	0.017	0.180	30.6	1.23	2.23	46.22
8	8	784.8	401.9	0.3700	3.79	15.21	0.024	0.200	29.8	1.18	2.18	44.23
9	10	981	501.9	0.2260	4.02	14.98	0.015	0.212	29.4	1.15	2.15	43.01
10	12	1177.2	601.9	0.1970	4.22	14.78	0.013	0.222	29.0	1.12	2.12	41.96
11	8	784.8	401.9	-0.0210	4.20	14.80	-0.001	0.221	29.0	1.12	2.12	42.07
12	4	392.4	201.9	-0.0420	4.15	14.85	-0.003	0.219	29.1	1.13	2.13	42.29
13	0	0	1.9	-0.1460	4.01	14.99	-0.010	0.211	29.4	1.15	2.15	43.08

Table E.2.2: Table with the test results for test T1.

Loads and deformations T2												
Load	Load	Total weight	Stress	dinc	dtotal	Final Thickness	Incremental Strain	Total strain	V	e	v	w
Step	(kg)	N	(kPa)	(mm)	(mm)	(mm)	(-)	(-)	(cm3)	(-)	(-)	(%)
0	0	0	0.0	0.00	0.00	19.00	0.000	0	37.3	1.15	2.15	42.98
1	0.37	3.6297	1.9	0.0030	0.00	19.00	0.000	0.000	37.3	1.15	2.15	42.97
2	1	98.1	51.9	0.3090	0.31	18.69	0.016	0.016	36.7	1.11	2.11	41.66
3	2	196.2	101.9	0.1670	0.48	18.52	0.009	0.025	36.3	1.09	2.09	40.95
4	3	294.3	151.9	0.1470	0.63	18.37	0.008	0.033	36.0	1.08	2.08	40.33
5	4	392.4	201.9	0.1250	0.75	18.25	0.007	0.040	35.8	1.06	2.06	39.80
6	5	490.5	251.9	0.1330	0.88	18.12	0.007	0.047	35.5	1.05	2.05	39.24
7	6	588.6	301.9	0.1380	1.02	17.98	0.008	0.054	35.3	1.03	2.03	38.65
8	8	784.8	401.9	0.3350	1.36	17.64	0.019	0.071	34.6	0.99	1.99	37.23
9	10	981	501.9	0.3880	1.75	17.26	0.022	0.092	33.9	0.95	1.95	35.59
10	12	1177.2	601.9	0.3430	2.09	16.91	0.020	0.110	33.2	0.91	1.91	34.14
11	8	784.8	401.9	-0.0240	2.06	16.94	-0.001	0.109	33.2	0.91	1.91	34.24
12	4	392.4	201.9	-0.0510	2.01	16.99	-0.003	0.106	33.3	0.92	1.92	34.46
13	0	0	1.9	-0.2570	1.76	17.24	-0.015	0.092	33.8	0.95	1.95	35.55

Table E.2.3: Table with the full test results for test T2

Loads and deformations T3												
Load	Load	Total weight	Stress	dinc	dtotal	Final Thickness	Incremental Strain	Total strain	V	e	v	w
Step	(kg)	N	(kPa)	(mm)	(mm)	(mm)	(-)	(-)	(cm3)	(-)	(-)	(%)
0	0	0	0.0	0.00	0.00	19.00	0.000	0	37.3	1.17	2.17	43.95
1	0.37	3.6297	1.9	0.0530	0.05	18.95	0.003	0.003	37.2	1.17	2.17	43.72
2	1	98.1	51.9	0.3530	0.41	18.59	0.019	0.021	36.5	1.13	2.13	42.21
3	2	196.2	101.9	0.2970	0.70	18.30	0.016	0.037	35.9	1.09	2.09	40.93
4	3	294.3	151.9	0.3760	1.08	17.92	0.021	0.057	35.2	1.05	2.05	39.32
5	2	196.2	101.9	-0.0140	1.07	17.94	-0.001	0.056	35.2	1.05	2.05	39.38
6	3	294.3	151.9	0.0840	1.15	17.85	0.005	0.060	35.0	1.04	2.04	39.02
7	4	392.4	201.9	0.3960	1.55	17.46	0.022	0.081	34.2	1.00	2.00	37.33
8	5	490.5	251.9	0.2630	1.81	17.19	0.015	0.095	33.7	0.97	1.97	36.20
9	6	588.6	301.9	0.2460	2.05	16.95	0.014	0.108	33.2	0.94	1.94	35.15
10	5	490.5	251.9	-0.0040	2.05	16.95	0.000	0.108	33.3	0.94	1.94	35.16
11	6	588.6	301.9	0.0520	2.10	16.90	0.003	0.111	33.2	0.93	1.93	34.94
12	8	784.8	401.9	0.3400	2.44	16.56	0.020	0.129	32.5	0.89	1.89	33.48
13	10	981	501.9	0.2970	2.74	16.26	0.018	0.144	31.9	0.86	1.86	32.21
14	12	1177.2	601.9	0.208	2.947	16.05	0.013	0.155	31.5	0.84	1.84	31.32
15	8	784.8	401.9	-0.025	2.922	16.08	-0.002	0.154	31.5	0.84	1.84	31.43
16	4	392.4	201.9	-0.055	2.867	16.13	-0.003	0.151	31.7	0.85	1.85	31.66
17	0	0	1.9	-0.223	2.644	16.36	-0.014	0.139	32.1	0.87	1.87	32.62

Table E.2.4: Table with the results for test T3.

Loads and deformations Beach Sand												
Load	Load	Total weight	Stress	dinc	dtotal	Final Thickness	Incremental Strain	Total strain	V	e	v	w
Step	(kg)	N	(kPa)	(mm)	(mm)	(mm)	(-)	(-)	(cm3)	(-)	(-)	(%)
0	0		0.0	0.00	0.00	20.00	0.000	0	39.3	0.76	1.76	28.50
1	0.9084	8.911404	4.5	-0.04	-0.040	20.04	-0.002	-0.002	39.3	0.76	1.76	28.64
2	1	98.1	54.5	0.13	0.090	19.91	0.006	0.005	39.1	0.75	1.75	28.21
3	2	196.2	104.5	0.064	0.154	19.85	0.003	0.008	39.0	0.75	1.75	28.00
4	3	294.3	154.4	0.056	0.210	19.79	0.003	0.011	38.9	0.74	1.74	27.81
5	4	392.4	204.4	0.043	0.253	19.75	0.002	0.013	38.8	0.74	1.74	27.67
6	5	490.5	254.3	0.037	0.290	19.71	0.002	0.015	38.7	0.74	1.74	27.55
7	6	588.6	304.3	0.034	0.324	19.68	0.002	0.016	38.6	0.73	1.73	27.44
8	8	784.8	404.2	0.062	0.386	19.61	0.003	0.019	38.5	0.73	1.73	27.23
9	10	981	504.2	0.057	0.443	19.56	0.003	0.022	38.4	0.72	1.72	27.04
10	12	1177.2	604.1	0.057	0.500	19.50	0.003	0.025	38.3	0.72	1.72	26.86
11	8	784.8	404.2	-0.013	0.487	19.51	-0.001	0.024	38.3	0.72	1.72	26.90
12	4	392.4	204.4	-0.028	0.459	19.54	-0.001	0.023	38.4	0.72	1.72	26.99
13	0	0	4.5	-0.128	0.331	19.67	-0.007	0.017	38.6	0.73	1.73	27.41

Table E.2.5: Table with the results for the test on beach sand.

Consolidation parameters T1					
Step	Average	mv	Es	Cc	Cs
interval	Stress (kPa)	(1/Pa)	(kPa)	(-)	(-)
1-2	10	4.29E-07	2.33E+03	0.040	
2-3	73	5.35E-07	1.87E+03	0.243	
3-4	124	1.56E-06	6.41E+02	1.167	
4-5	175	6.17E-07	1.62E+03	0.597	
5-6	225	4.03E-07	2.48E+03	0.486	
6-7	276	3.38E-07	2.96E+03	0.489	
7-8	348	2.38E-07	4.21E+03	0.427	
8-9	449	1.49E-07	6.73E+03	0.336	
9-10	550	1.32E-07	7.60E+03	0.358	
10-11	492	7.10E-09			0.017
11-12	285	1.42E-08			0.020
12-13	19	4.92E-08			0.010

Table E.2.6: Consolidation parameters for the different loading steps for oedometer test T1.

Consolidation parameters T2					
Step	Average	mv	Es	Cc	Cs
interval	Stress (kPa)	(1/Pa)	(kPa)	(-)	(-)
1-2	10	3.25E-07	3.07E+03	0.024	
2-3	73	1.79E-07	5.60E+03	0.064	
3-4	124	1.59E-07	6.30E+03	0.096	
4-5	175	1.36E-07	7.35E+03	0.114	
5-6	225	1.46E-07	6.86E+03	0.156	
6-7	276	1.52E-07	6.56E+03	0.198	
7-8	348	1.86E-07	5.37E+03	0.305	
8-9	449	2.20E-07	4.55E+03	0.454	
9-10	550	1.99E-07	5.03E+03	0.491	
10-11	492	7.10E-09			0.015
11-12	285	1.51E-08			0.019
12-13	19	7.56E-08			0.014

Table E.2.7: Consolidation parameters for the different loading steps for oedometer test T2.

Consolidation parameters T3					
Step	Average	mv	Es	Cc	Cs
interval	Stress (kPa)	(1/Pa)	(kPa)	(-)	(-)
1-2	10	3.73E-07	2.68E+03	0.0279	
2-3	73	3.19E-07	3.13E+03	0.1159	
3-4	124	4.11E-07	2.43E+03	0.2479	
4-5	124	1.56E-08			0.0092
5-6	124	9.37E-08		0.0554	
6-7	175	4.44E-07	2.25E+03	0.3664	
7-8	225	3.01E-07	3.32E+03	0.3130	
8-9	276	2.86E-07	3.49E+03	0.3577	
9-10	276	4.72E-09			0.0058
10-11	276	6.14E-08		0.0756	
11-12	348	2.01E-07	4.97E+03	0.3129	
12-13	449	1.79E-07	5.58E+03	0.3520	
13-14	550	1.28E-07	7.82E+03	0.3015	
14-15	492	7.79E-09			0.0163
15-16	285	1.71E-08			0.0210
16-17	19	6.91E-08			0.0125

Table E.2.8: Consolidation parameters for the different loading steps for oedometer test T3.

Consolidation parameters Beach Sand					
Step	Average	mv	Es	Cc	Cs
interval	Stress (kPa)	(1/Pa)	(kPa)	(-)	(-)
1-2	16	1.30E-07	7.70E+03	0.011	
2-3	75	6.43E-08	1.55E+04	0.020	
3-4	127	5.65E-08	1.77E+04	0.029	
4-5	178	4.35E-08	2.30E+04	0.031	
5-6	228	3.75E-08	2.67E+04	0.034	
6-7	278	3.45E-08	2.90E+04	0.038	
7-8	351	3.15E-08	3.17E+04	0.044	
8-9	451	2.91E-08	3.44E+04	0.052	
9-10	552	2.92E-08	3.43E+04	0.064	
10-11	494	3.34E-09			0.0066
11-12	287	7.18E-09			0.0083
12-13	30	3.28E-08			0.0068

Table E.2.9: Consolidation parameters for the different loading steps for oedometer test on beach sand.

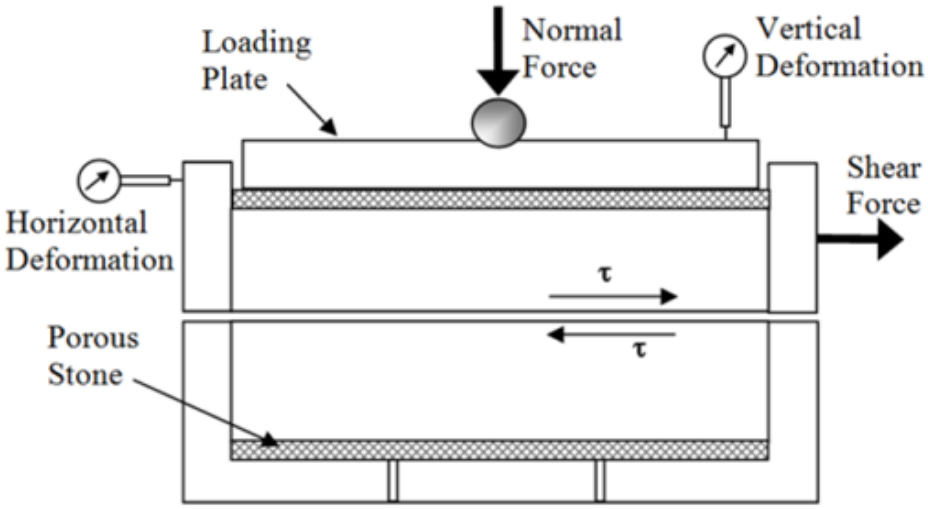

Figure E.3.1: Schematic of the basic shear box setup. Figure from "Direct Shear — Geotechnical Testing Lab" (n.d.).

E.3 Shear box testing

This appendix will outline sample preparation, testing procedure and some additional results for the shear box testing performed for this study.

E.3.1 Shear box setup

The basic setup for the shear box setup consists of a sample holder which is split in half, so that the two halves can slide over each other. The halves have a porous top and bottom stone. A top cap is placed on top of the sample. The top cap is connected to an arm on which weights can be placed which provides a normal force on the sample. Linear displacement sensors are placed in such a way that both the vertical displacement of the top cap and the horizontal displacement of the shear box can be measured. The two halves are connected to a drive which can horizontally displace one of the halves of the shear box at constant speed, exerting a shear force which is measured by a sensor connected to the box.

E.3.2 Sample preparation

There are two kinds of samples tested in the shear box during this study. Firstly the reef blocks are prepared using a cutting ring. The material for this experiment was sampled using a sample

Figure E.3.2: Photos of the material from the sample tubes from which section were cut for shear box testing.

Sample Dimensions	Reef blocks	Sand
Location	6.1C	Le Croisic
Ring inner diameter [mm]	63.0	63.0
Ring height [mm]	21.0	19.5
Sample volume [cm3]	65.5	60.8

Table E.3.1: Sample dimensions for the shear box samples.

tube which was vertically inserted in the top of a reef block making sure the tubes were aligned roughly with the long axis of the sample tube. The sample cutting ring was then pushed into the material in such a way that the tubes were aligned from the top to the bottom in the sample ring. As such, after placement the shear force will be applied perpendicular to the tube direction. The sample was then cut along the top and bottom of the cutting ring, and any large holes were backfilled. The samples were then pushed from the cutting ring into the shear box and tested.

The beach sand samples were prepared in three different ways to get different void ratios. The samples were prepared directly inside the shear box. In beach sand samle 1, the sands were placed carefully layer-by-layer using a funnel. This sample was as carefully handled as possible to not have any disturbances. This resulted in a high void ratio of 0.98. In beach sand sample 2, the sand was placed carefully, layer-by-layer, using a funnel. It was then compacted as a complete sample using a hammer to vibrate the mold and a tamper to compact the sand. This resulted in an intermediate void ratio of 0.83. For beach sand sample 3, sand was placed layer-by-layer in shear box. After every layer was placed, the mold was vibrated with a hammer and compacted with a tamper until the surface did not move down any more. Than, a new layer was placed and these steps repeated until the sample was complete. This resulted in a relatively low void ratio of 0.71. The exact final dimensions of the different samples are given in table E.3.1.

E.3.3 Testing regimen

After the samples were placed in the shear box setup, the apparatus was assembled. The following steps were then followed during testing.

1. The load for the first step (1.5 kg) is added to the loading frame.
2. The load is transferred to the sample by releasing the arm carrying the load frame.
3. The sample is left to settle until no change is seen in the vertical measurements until no change is seen for 30 seconds. This generally takes about 5 minutes.
4. The shear apparatus is then set to run at 1.000 mm/min until the shear force becomes constant or starts to decrease.

Sample parameters	Void ratio (-)	Tested density (g/cm3)	Dry density (g/cm3)
Test 1	1.01	1.61	1.33
Test 2	1.01	1.58	1.33
Test 3	1.30	1.49	1.16
Beach sand 1	0.98	1.35	1.35
Beach sand 2	0.83	1.46	1.45
Beach sand 3	0.71	1.57	1.56

Table E.3.2: Sample parameters for the shear box samples.

5. The load is doubled, and steps 1-4 are repeated.
6. Steps 1-5 are repeated until the load on the load frame is 12 kg and the shear forces do not increase anymore or until the apparatus reaches its maximum displacement of just over 10 mm.
7. The sample is then taken out of the shear box, weighed and placed in a 105 °C oven overnight.
8. The sample is taken out of the oven, weighed again and examined. From this, the basic sample parameters as given in table E.3.2 are determined.

E.3.4 Additional results

For every single sample, the maximum shear stress for every load step was plotted against the normal stress for the load step. A Mohr-Coulomb envelope was then linearly fitted to the data and from there, the apparent cohesion and friction angle were determined. These can be found in table 4.3.1. The figures from where these data were determined can be found in figures E.3.3 and E.3.4.

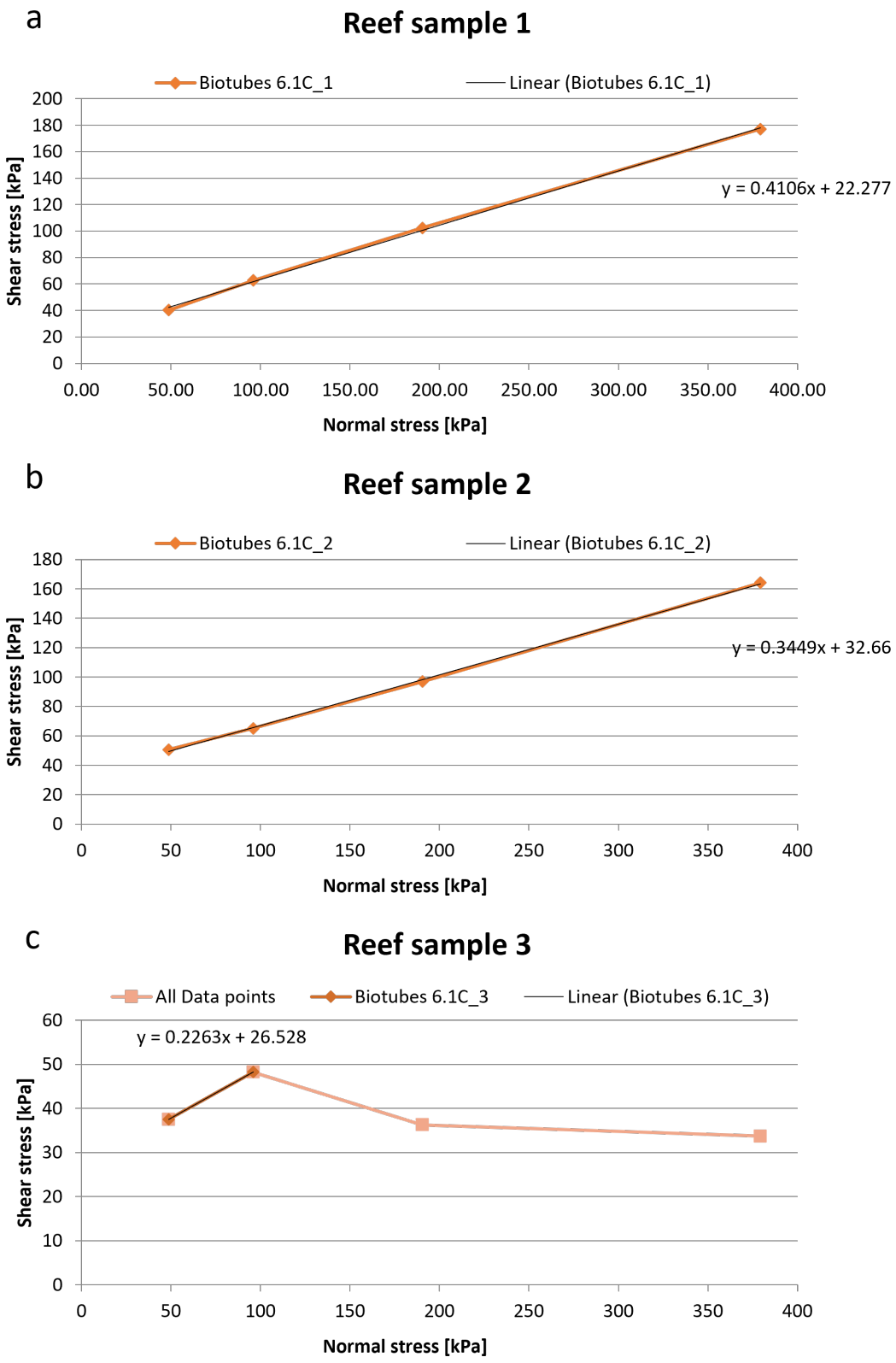

Figure E.3.3: Normal vs shear stress plots for the different reef samples from shear box testing with the linear fit from which the cohesion and friction angle are determined.

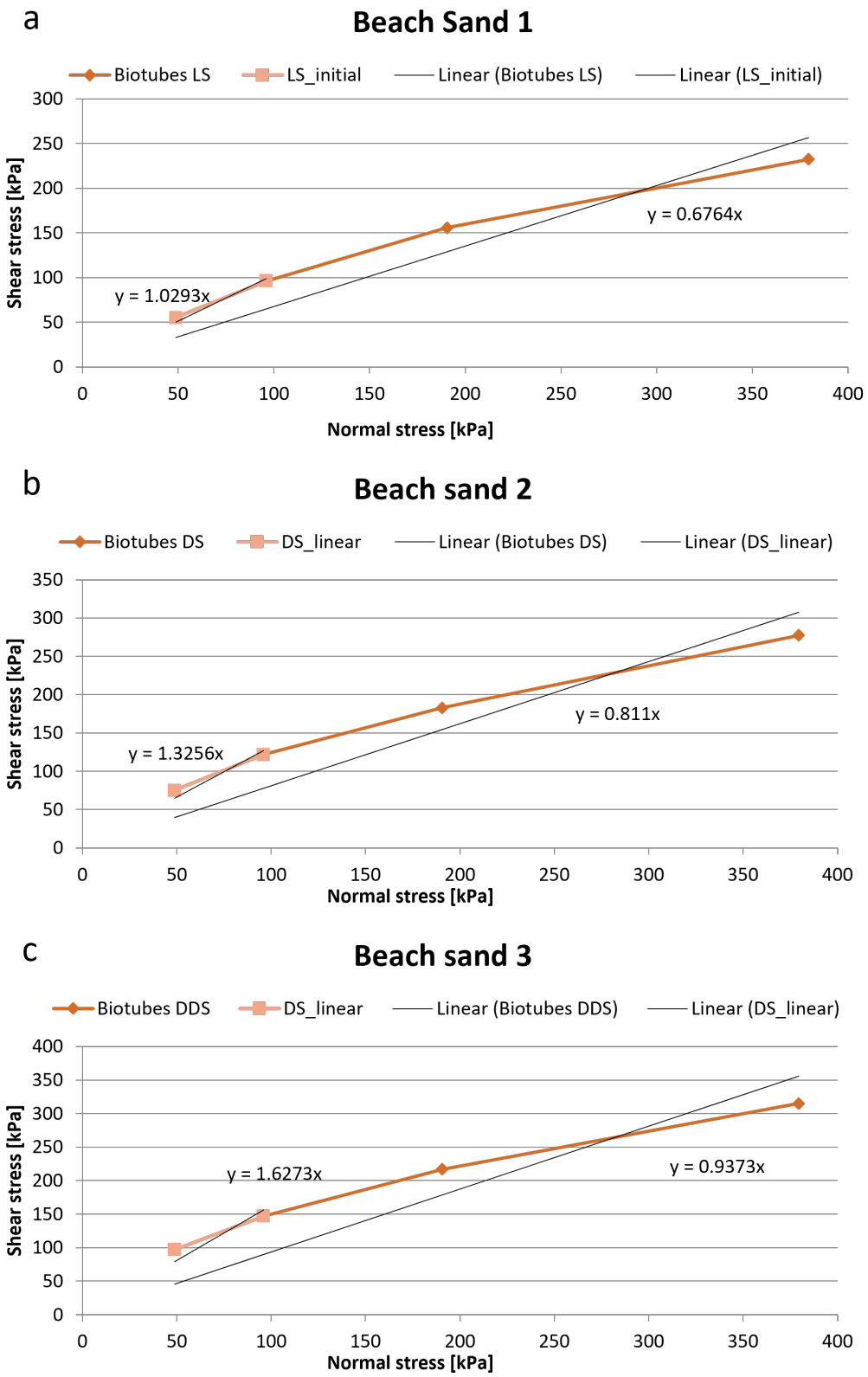

Figure E.3.4: Normal vs shear stress plots for the different beach sand samples from shear box testing with the linear fit from which the cohesion and friction angle are determined.

Appendix F

Haploops Nirae

Apart from the Sabellaria worm, there are several more interesting ecosystem engineering species. A good example of this is Haploops Nirae, a tube dwelling amphipod which in some places forms thick tube mats, instead of the reefs which are common for the Sabellaria. However, this species is much less studied, and is not at all studied from an engineering geology perspective. They are small crustaceans living in the deep bottom sediments where they build tubes out of small particles of mucus and pseudofaeces (Rigolet, 2013). From their tubes H. Nirae catch food particles by sticking their antenna and legs out of their tubes. In turn, they themselves are an important food source for many species of fish such as cod (HELCOM Red List Biotope Expert Group, 2013). The several haploops species are present in many oceans all over the world. This is illustrated by figure F.0.1, which shows the presence of the different species of Haploops over the world. However, H. Nirae specifically is mostly found in the North Atlantic, Northern Pacific and Arctic oceans. Notable concentrations are found in the Øresund and the Kattegat in Sweden, the Gulf of Clyde, Scotland as well as the Gulf of Cascogne and the Bay of Concarneau in France (Rigolet, 2013). Because these habitats are in danger of going extinct in many places, they are currently part of the European OSPAR list (OSPAR commission, 2021).

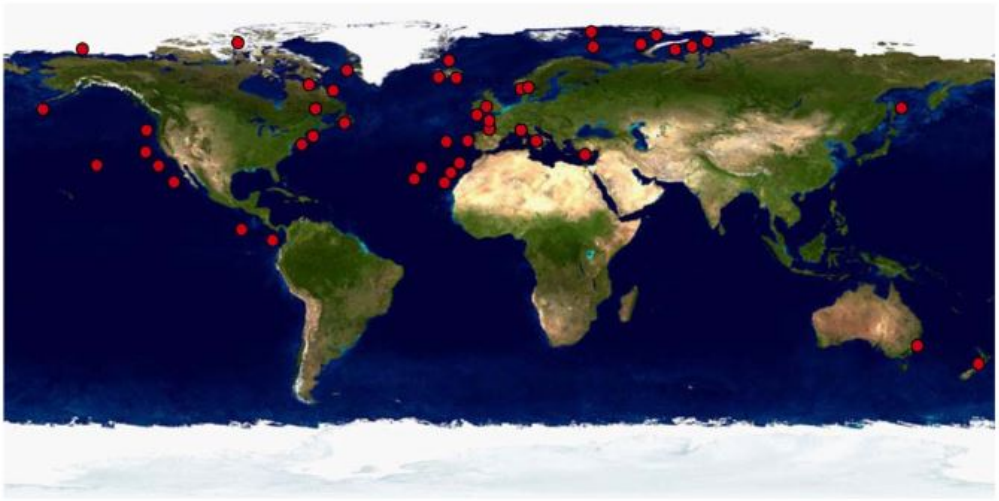

Figure F.0.1: Map illustrating occurrence of different Haploops species over the world. Map from Rigolet (2013).

It must be noted that H. Nirae are known to live at depths of 15 to 320 meters on muddy bottoms, which allow them to build their tubes. Each individual lives in its own tube, which can only be opened from the inside. These are positioned vertically in the sediment and protrude from it (Reynaud, 2014). They are made from a mixture of slime, pseudofaeces (particles which were not digested by the animal) and mucus (Rigolet, 2013). Interestingly, the filtration rate of this species is much higher than other species such as bivalves, gastropods or polychaete annelids. The population in the bay of Concarneau would be capable to filter the complete volume of the bay in a period of 29-30 days (Rigolet et al., 2011).

It is notable that in the bay of Concarneau in France, the population of H. Nirae perfectly overlaps a field of pockmarks. Pockmarks are the product of gasses and fluids welling from the sea bed because of e.g. seismic events, iceberg scouring, trawling or tidal pressures. As such, a mechanistic link between the two has been suggested but not elaborated and their link is unclear (Champilou et al., 2019; Reynaud, 2014).

However, it is known from personal communications with local fishermen, that the colony of H. Nirae along the coast of Le Croisic is a no-go area for local fishermen due to their nets getting stuck at the bottom in these areas. This is because the H.Nirae tubes sticking out of the sea bottom get caught in the mesh netting. This happens with such force that nets sometimes need to be cut or left. As such, there is good reason to assume that the H. Nirae tubes have significant strength and that their colonies impact the sediment behaviour significantly.